Title: Experiments and Modeling to Support Field Test Design

Author(s): Johnson, Peter Jacob
Bourret, Suzanne Michelle
Zyvoloski, George Anthony
Boukhalfa, Hakim
Stauffer, Philip H.
Weaver, Douglas James

Intended for: Report

Issued: 2017-09-25 (rev.1)

Experiments and Modeling to Support Field Test Design

Spent Fuel and Waste Disposition

P.J. Johnson
S.M. Bourret
H. Boukhalfa
F.A. Caprouscio
G.A. Zyvoloski
D.J. Weaver
S. Otto
P.H. Stauffer

Los Alamos National Laboratory
August 31, 2017

FCT Quality Assurance Program Document

Appendix E
FCT Document Cover Sheet

Name/Title of Deliverable/Milestone		**Test Proposal Document for Phased Field Thermal Testing in Salt**		
Work Package Title and Number		SF-17LA01030302	Salt R&D - LANL	
Work Package WBS Number		1.08.01.03.03 - Salt Disposal R&D		
Responsible Work Package Manager		Philip H. Stauffer		
		(Name/Signature)		8/31/17
Date Submitted				
Quality Rigor Level for Deliverable/Milestone	☒ QRL-3	☐ QRL-2	☐ QRL-1 ☐ Nuclear Data	☐ N/A*

This deliverable was prepared in accordance with   Los Alamos National Laboratory
(Participant/National Laboratory Name)

QA program which meets the requirements of
    ☒ DOE Order 414.1   ☐ NQA-1-2000

This Deliverable was subjected to:

Technical Review (TR)	Peer Review (PR)
☐ Technical Review	☐ Peer Review
Technical Review (TR)	**Peer Review (PR)**
Review Documentation Provided	**Review Documentation Provided**
☐ Signed TR Report or,	☐ Signed PR Report or,
☐ Signed TR Concurrence Sheet or,	☐ Signed PR Concurrence Sheet or,
☒ Signature of TR Reviewer(s) below	☐ Signature of PR Reviewer(s) below

Name and Signature of Reviewers

Hari Viswanathan

*Note: In some cases there may be a milestone where an item is being fabricated, maintenance is being performed on a facility, or a document is being issued through a formal document control process where it specifically calls out a formal review of the document. In these cases, documentation (e.g., inspection report, maintenance request, work planning package documentation or the documented review of the issued document through the document control process) of the completion of the activity along with the Document Cover Sheet is sufficient to demonstrate achieving the milestone. QRL for such milestones may be also be marked N/A in the work package provided the work package clearly specifies the requirement to use the Document Cover Sheet and provide supporting documentation.

Table of Contents

List of Figures

Experiments and Modeling to Support Field Test Design

Experiments and Modeling to Support Field Test Design

List of Tables

1 Introduction

Disposition of heat-generating nuclear waste (HGNW) remains a continuing technical and sociopolitical challenge. We define HGNW as the combination of both heat generating defense high level waste (DHLW) and civilian spent nuclear fuel (SNF). Numerous concepts for HGNW management have been proposed and examined internationally, including an extensive focus on geologic disposal (c.f. Brunnengräber et al., 2013). One type of proposed geologic material is salt, so chosen because of its viscoplastic deformation that causes self-repair of damage or deformation induced in the salt by waste emplacement activities (Hansen and Leigh, 2011). Salt as a repository material has been tested at several sites around the world, notably the Morsleben facility in Germany (c.f. Fahland and Heusermann, 2013; Wollrath et al., 2014; Fahland et al., 2015) and at the Waste Isolation Pilot Plant (WIPP) near Carlsbad, NM. Evaluating the technical feasibility of a HGNW repository in salt is an ongoing process involving experiments and numerical modeling of many processes at many facilities.

Much of this report focuses on numerical modeling and experiments pertaining to physical processes that occur during and shortly after the period of hypothetical HGNW emplacement in a salt repository. Several processes occur within the host material prior to and immediately following the final viscoplastic closure of the salt gallery. Modeling described herein uses the numerical model Finite Element Heat and Mass (FEHM, https://fehm.lanl.gov; see Zyvoloski et al., 2012). The code has been applied to a wide variety of problems involving coupled heat, stress, and mass flow, including geothermal and hydrothermal processes (c.f. Spinelli and Fisher, 2004; Winslow et al., 2016), near-surface gas transport (Stauffer et al., 2005), and others. Over the past few years, new functionality has been built into the code to allow for modeling of physiochemical processes in salt (Jordan et al., 2015a,b,c; Bourret et al., 2016; Bourret et al., 2017). Efforts to both refine the code and use it to gain an improved understanding of the modeled systems are ongoing. Code refinements further serve to broaden the applicability of FEHM into new study areas and applications.

Salt within a repository may occur in two basic forms: dense bedrock and crushed run-of-mine (ROM) salt. One generic concept is for "in-drift" disposal of HGNW in which a canister is placed in an open gallery and covered with crushed run-of-mine (ROM) salt (Bechthold et al., 2004; Hansen and Leigh, 2011). Much of the work presented in this report supports ongoing investigation into the processes that occur within the ROM salt when a heat source is applied inside it, particularly brine migration (c.f. Doughty and Pruess, 1990; Cinar et al., 2006; Caporuscio et al., 2013). The second major aspect of the salt disposal problem is to understand how the heat generated by HGNW affects intact salt following closure of the gallery. Experimental designs described herein aim to gain fundamental understanding of coupled heat and fluid flow and how they affect the salt surrounding the gallery. Numerical modeling prior to physical experiments can aid in experiment design and prediction of results. Furthermore, numerical models are necessary in any predictive analysis of the long-term behavior of a repository. Validation of numerical models against short-term experiments and ensuring proper

representation of the physics of heat/salt interactions is necessary prior to undertaking long-term modeling efforts.

Previous work at LANL on experiments and numerical modeling of brine flow in salt has been presented in numerous milestones and published papers over the past several years (c.f. Stauffer et al. 2013, Jordan et al. 2015a,b,c; Stauffer et al., 2015). Further refinement was conducted during the 2016 fiscal year (Bourret et al., 2016) and early 2017 (Bourret et al., 2017; see Appendix B). Current work focuses on the existing facility at WIPP as a surrogate for a generic site. WIPP features fluid flow and deformation in galleries carved into complex but salt-rich layers (Krieg, 1984; Lappin, 1988; Kuhlman and Malama, 2013). Parallel efforts on modeling brine transport have been conducted at multiple DOE and academic research facilities recently (Robinson et al., 2012; Stauffer et al., 2013; Rutqvist et al., 2016). Although materials other than NaCl salt are present in rock layers at WIPP, salt remains a dominant mineral phase. Understanding fluid flow in salt is fundamental to research concerning the generic salt repository concept.

For the past several years, international collaborative efforts have identified a continuing need to enhance understanding of generic salt repository science through experiments, model development, and benchmarking calculations (Hansen et al., 2015; Hansen et al., 2016; Hansen et al, 2017). The 6th US/German Workshop on Salt Repository Research and Development proceedings identified a need for "Further development of geomechanical constitutive laws and calculation methods… [including] hydro-mechanical interactions (pore pressure build-up in case of delayed drainage) as well as microstructural processes influenced by moisture" (Hansen et al., 2016). The mention of moisture influence on microstructural processes raises a related issue concerning moisture migration and its consequent effects on drift salt shortly following emplacement, prior to compaction of the repository. Heat from waste may create a dry halo that prevents brine from reaching the canister (Hansen and Leigh, 2011), but multiphase flow in repository salt is still under study (Kuhlman and Malama, 2013). Several papers have examined brine migration from a heat source through various approaches (c.f. Birkholzer, 2004; Caporuscio et al., 2013; Kuhlman and Malama, 2013; Rutqvist et al., 2016; Bourret et al., 2016; As suggested in Hansen et al. (2016), an in-drift experiment with a heater in salt would assist in validating work concerning emplacement of heat-generating canisters in salt.

In addition to the work on ROM salt, this report also presents modeling of heaters in boreholes drilled into the dense, relatively impermeable wall rock as proposed in Stauffer et al., (2015) and Kuhlman et al. (2017). Proposed experiments aim to quantify potential brine and chemical interactions in the wall rock, particularly migration of brine into a borehole with a heater applied. A variety of experiment concepts have been proposed in recent milestones (Jordan et al., 2016; Bourret et al., 2016; Kuhlman et al., 2017) ranging from small diameter boreholes to full drift scale multiple canister heater tests. One driving motivation is to better constrain brine availability in the wall rock, which informs both the availability of brine after gallery closure but also is suggestive of brine availability when the rock salt and associated evaporite minerals are crushed for ROM salt. Brine content of bedded salt can range from <1% by weight for dense salt to several weight percent when clay minerals are present (Powers,

1978), but the presence, availability, and migration potential are unclear for WIPP bedrock. These factors may strongly influence the safety basis and efficacy of a generic salt repository, but are as yet poorly understood. Field experiments can add knowledge about these factors, increasing confidence in generic repository science (Kuhlman and Malama, 2013).

This milestone is organized into eight content sections. Section 2 summarizes changes that to FEHM subroutines that pertain to salt since the end of September, 2016. Section 3 describes a new functionality built into FEHM during FY 2017 for capillary suction calculations in a porous medium with changing porosity. This new functionality is still under development but is, to the best of the authors' knowledge, unique in publicly used modeling software. Verification and small-scale validation follow in Sections 4, 5, and 6, with testing of simple meshes and a reexamination of one of the main experiments of fluid flow in crushed salt (Olivella et al., 2011). Numerical experiments in support of future borehole experiments are described in Section 7. Section 8 presents experimental work performed in support of field testing during FY17. Preliminary modeling of a scaled up two-dimensional mesh of an ongoing, DOE-EM funded, in-drift heated canister experiment is presented in Section 9.

2 FEHM Updates

2.1 Code modifications

Several code changes and additions have been applied to FEHM subroutines (Table 1). Many of these changes are minor amendments to improve efficiency in terms of timesteps or iterations. The modular nature of FEHM typically requires amendments to several subroutines. In addition to minor cosmetic or performance enhancements, two substantial code additions are in development and implementation. One is an in-development code for temperature-dependent heat capacity of the solid matrix. Application to salt of this model has not yet been implemented but is intended in continuing work, so changes to subroutines for this function are included here but a more enhanced description is not. The second major addition is for porosity-dependent capillary suction, which is described conceptually in Section 3 with test problems in Sections 4, 5, and 6. A brief summary of the subroutine changes for these functions is included in Table 1. Usage of the new capillary function is described in Appendix A.

Table 1: Changes to FEHM routines.

Subroutine	Description of change
allocmem.f	Allocated arrays needed for SoilVision combining of contour files
anonp.f	Added coding to correct negative volumes due to element node ordering
cappr.f	Added (n, Sl) calculations
comai.f	Added some variables in the use module
combi.f	Added arrays needed for saving zones
comdi.f	Added declaration for flag for (n,sL) function

comdi_1.f	Added arrays necessary for nonlinear rock density and heat capacity
comsi.f	Added arrays necessary for additional nonlinear stress parameters
coneq1.f	Modified transport equations for new GDKM models
enthp_1.f	Modified the routine so it works when using a nonlinear rock heat capacity in a conduction-only problem
flow_boundary_conditions.f	Small correction to constant-saturation boundary condition
gdkm_volume_fraction_interface.f	Modifications to implement new GDKM conceptual models
geneq1.f	Small fix to incorporate directional GDKM fracture models
geneq2.f	Small fix to incorporate directional GDKM fracture models
geneqc.f	Small fix to incorporate directional GDKM fracture models
ingdpm1.f	Added simplified input to GDKM; old input still allowed
initdata2.f	Modified zone input to accept saved zones
pstal.f	Called sparrow vapor pressure lowering
rlp_cap.f	Made correction to VG models for rlpm
rlperm.f	Added flag, definitions, and reads for (n, Sl) function and link to linear relative permeability model; correction to input of relative perm models when GDKM models are present
scanin.f	Added recognition of new rlp inputs
scanin1.f	Added check of GDKM for new input
startup.f	Turn off vapor flux output for Richard's eqn; apply volume fraction to some flow and transport parameters; changed some calls to GDKM module
stress_3D_post.f	Changed subroutine header for calling principle stress routine
stressctr.f	Changed subroutine header for calling principal stress routine
thermw_1.f	Implemented nonlinear rock density and heat capacity terms
thrmwc_1.f	Implemented nonlinear rock density and heat capacity terms
write_avs_node_con_6.f	Enabled output from saved zones and output gdkm blanking
write_avs_node_mat.f	Added ifblock for GDKM
write_avs_node_s.f	Enabled output from saved zones and output gdkm blanking
write_avs_node_v_temp1.f	Enabled output from saved zones and output gdkm blanking
zone_4.f	Implemented zone "saved"

3   New capillary effect model

3.1   Background

Model simulations in support of salt typically encounter significant changes in the porosity of portions of the model domain (Bourret et al., 2016; Bourret et al., 2017). This presents a challenge for functions in the model that are specified for initial conditions but are highly sensitive to these changes. One aspect of the model that has been problematic is the choice of the water retention curve, which in FEHM is specified through the *rlp* macro and calculates capillary suction pressure (P_c) as a function of saturation in each timestep. Several formulations are implemented, including linear models (Forsythe, 1988), the Brooks and Corey

Experiments and Modeling to Support Field Test Design

(1964) approach, and the van Genuchten (1980) functions. The choice of P_c model influences node saturation and water flow calculations, which in turn also affect the flow of heat. Consequently, defining a proper function is vital to ensure accurate results. Furthermore, in the salt domain, porosity changes which affects capillary suction. This can cause capillary effects to be higher than expected in portions of the model domain that have experienced considerable increases in porosity (Figure 1).
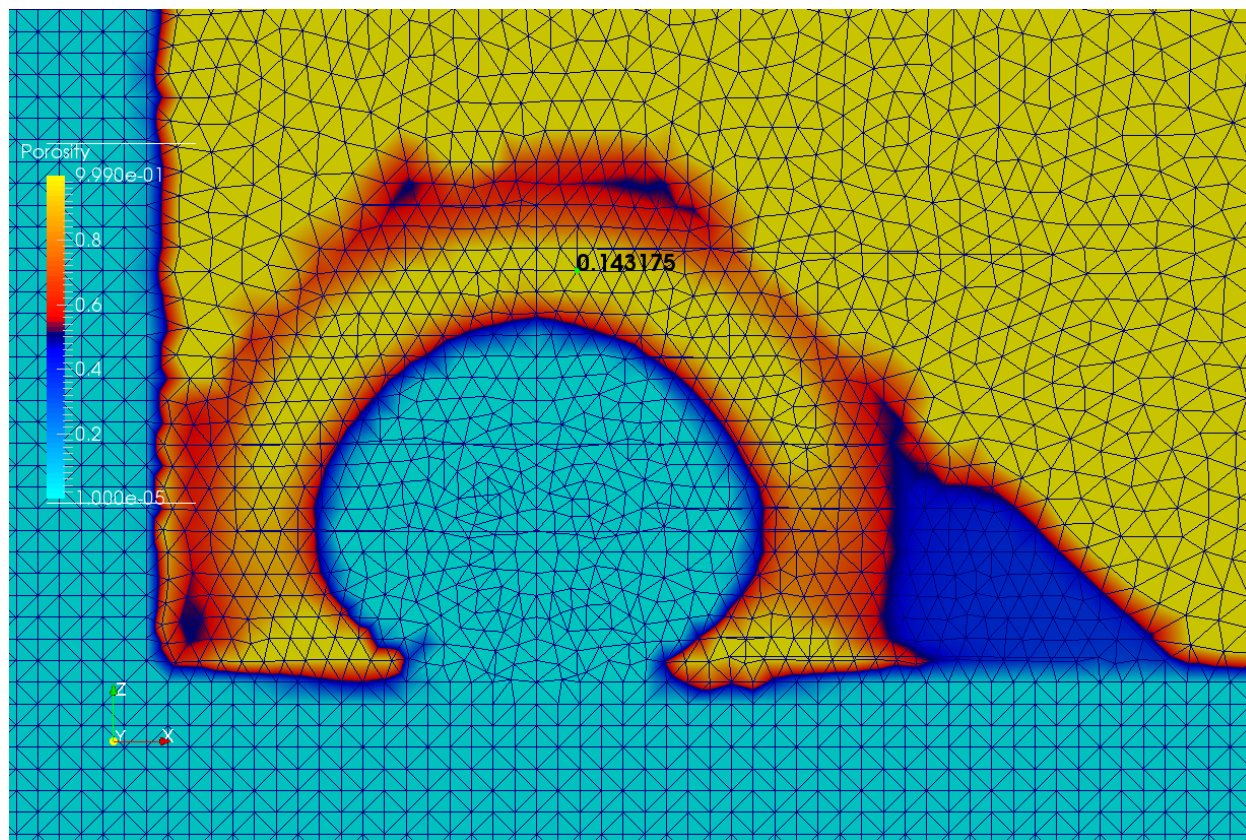
Figure 1: Modeled mesh showing highly porous (n = 0.999935, yellow color), partially saturated (S_l = 0.143) node (green dot). The region surrounding this node is similarly porous and partially saturated. This results from high capillary suction which is appropriate for the early period of the model run Red color indicates high porosity and blue color indicates low porosity.

In an effort to improve model representation of the physical system through the duration of the model run, we have developed a porosity-dependent capillary suction function. This new function is built into the *rlp* macro in FEHM that allows the user to specify initial parameters (Table 2) and then calculates a new retention curve at each timestep if porosity changes. The function then reads new parameters from the model global variable arrays (Table 3) and calculates a new pressure accordingly. A description of the function and verification that it is operating correctly follows. For clarity, we refer to the porosity dependent function $P_c(n, S_l)$ as the "new model," and the previously developed linear models as the "old model." No direct changes have been applied to the old model and it remains a usable function in FEHM.

Experiments and Modeling to Support Field Test Design

Table 2: User-entered parameters for porosity-dependent capillary function.

Parameter	Description	Sample model input
n_i	Initial porosity (-)	0.35
S_{ri}	Initial residual saturation (-)	0.1
P_{cmaxi}	Initial maximum capillary pressure (MPa)	0.013

Table 3: Parameters from each timestep used in porosity-dependent capillary function

Parameter	Description
S_l	Saturation (-)
n	New porosity calculated in previous timestep (-)
S_r	Residual saturation for new porosity (-)
$P_c(n, S_l)$	Capillary pressure calculated for new porosity and saturation (Pa)
P_{cmax}	Maximum capillary pressure for new porosity (Pa)
S_{lmax}	Calculated saturation at which capillary pressure goes to zero for new porosity (Pa)

3.2   Function description

The core functionality is similar to the existing linear model already implemented in FEHM based on Forsythe (1988). In the previous function, the user specifies a maximum capillary pressure P_{cmax} at 0 saturation, a residual saturation S_r, and a maximum saturation S_{lmax} above which capillary pressure is zero. Capillary pressure P_c is then calculated as a linear fit given by:

$$P_c = P_{cmax}, \qquad S_l \leq S_r$$

$$P_c = P_{cmax} \frac{S_{lmax}-S_l}{S_{lmax}-S_r}, \qquad S_{lr} < S_l < S_{lmax} \qquad \text{Eq. 1}$$

$$P_c = 0.0, \qquad S_l \geq S_{lmax}$$

To account for changing porosity, the same general function is used but with dynamic calculation of the end points S_r, P_{cmax} and S_{lmax}. In effect, the new function calculates a new liquid retention curve at each timestep. Capillary pressure generally increases as porosity decreases, and approaches zero for all saturations as porosity increases. This approach is predicated on the assumption that changing porosity corresponds to changing average pore diameter and, consequently, increasing radius of interface curvature (Fitts, 2013) with otherwise equivalent capillary drivers such as contact fluid contact angle (Kumar and Prabhu, 2007; Masoodi and Pillai, 2012). For application to the salt problem, this assumption is often justified because changes in porosity are primarily driven by the migration, evaporation, or condensation of brine and water vapor within existing pore space. Note that this may require future reexamination in the context of thermal effects causing release of volatiles from evaporite minerals in repository salt. Borehole experiments described in Section 7 may provide some insight into this process.

3.1.1 Calculation of residual saturation end-member

Two formulations of the residual saturation end member are implemented. In both cases, the user selects a starting value that define an initial retention curve; in all variables described hereafter, the subscript i denotes initial parameters. The first formulation is a linear extrapolation which assumes that at a porosity of 1, S_r is zero and applies a line between the (n, S_r) points of $(0,0)$, (n_i, S_{ri}), and extends to $(1, S_{rmax})$. The line is given by:

$$S_r(n) = -\frac{S_{ri}}{1-n_i}n + \frac{S_{ri}}{1-n_i} \qquad \text{Eq. 2}$$

where S_{ri} is the user specified residual saturation in control statement *rlp*, n is current node porosity calculated during the model run, and n_i is the initial porosity specified by the user in control statement *rock*.

The second formulation for S_r is based on Buckles (1965) and is given by

$$S_r \times n = \alpha \qquad \text{Eq. 3}$$

Where α is a constant.

Further revision to this was proposed by Holmes et al. (2009), wherein an exponent q was applied to S_r,

$$S_r^q \times n = \alpha \qquad \text{Eq. 4}$$

However, the exponent q typically falls between about 0.8 and 1.2, so for the present work it is taken as 1. Future code development might add this feature if necessary.

Solving for S_r with updating porosity causes a curve fit to the $S_r(n)$ function which causes greater increases in S_r than the linear extrapolation when porosity is decreasing greatly (Figure 2).

As a consequence of the increased residual saturation, capillary pressures in the model with non-linear S_r reach their maximum value at higher saturation than the linear S_r case. Consequently, nodes with decreasing porosity will tend to retain a higher saturation value under the new model than in the constant linear model. Capillary pressure in this setup decreases very rapidly at high porosity because the slope of the interpolated line is greater than in the initial linear function. An additional challenge with this function is that when a dynamic S_{lmax} is applied, the slope of the line can become positive, where higher saturation has a higher capillary pressure. If this occurs for high porosity, P_c is defined as zero. A similar problem can arise at very low porosity in which case P_c is assigned to its maximum value. Testing of the $P_c(n,S_l)$ function with the nonlinear form of S_r is ongoing. Subsequent simulations use the linear formulation unless indicated otherwise. Excluding the large 2D single canister mesh, most of the models featured porosity and saturation values in a range where the two models are roughly equivalent.

Residual saturation functions
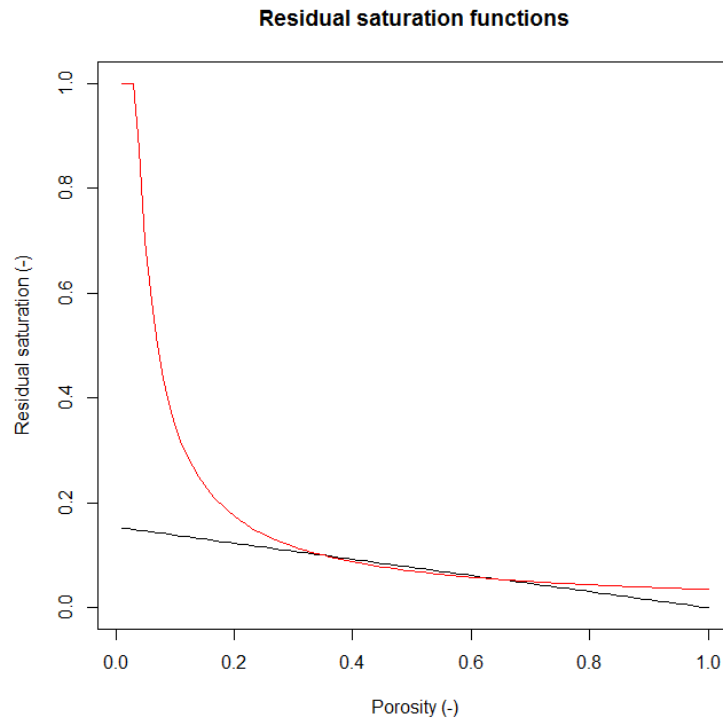
Figure 2: Comparison of residual saturation values as a function of porosity. Black line indicates linear model (Eq. 2), red line indicates non-linear model (Eq. 4).

3.1.2   Calculation of maximum capillary pressure

In the old P_c function, the user inputs a maximum capillary pressure at 0 saturation. For the new function, this input is changed slightly, where the user inputs an initial maximum capillary pressure P_{cmaxi} at the initial residual saturation S_{ri}. For each timestep the maximum pressure P_{cmax} is updated as

$$P_{cmax} = \frac{P_{cmaxi}}{S_{ri}}(S_r)$$

Eq. 5

The S_r calculation from section 3.1.1 is applied to this equation. This formulation is helpful in light of the changing S_r value, so that the maximum pressure can be easily and directly calculated as S_r changes. Separating these calculations will allow for relatively easy code modification in the future if additional information becomes available that allows for improved definition of these functions.

3.1.3   Calculation of maximum saturation

Less theoretical work has been done for changes with respect to porosity in the maximum saturation above which capillary pressure goes to zero because capillary suctions are at their lowest when the wetting phase is close to full saturation. However, in the modeling work pertaining to salt, porosity of a single node can change from values typical for slightly

compacted spheres ($n = 0.35$) to close to $n = 1$. Thought must therefore be given to how to handle capillary effects across the full range of porosity and saturation values, including high-porosity/high-saturation cases. Two approaches are currently applied in the function to account for this. The user can elect to keep S_{lmax} value at 1 (capillary pressures applied for all saturation) or to have the code use a simple linear function as

$$S_{lmax} = 1 - n \hspace{8cm} \text{Eq. 6}$$

In most cases of high porosity where this value changes greatly from 1, capillary suction effects are limited by the other calculations used in the function fit. Changing S_{lmax} primarily affects the slope of the $P_c(S_l)$ line, and at high porosity suction effects are near zero even when S_{lmax} is held at 1. Holding S_{lmax} constant at 1 also eliminates issues arising with the non-linear S_r function where S_r is greater than S_{lmax}; with S_{lmax} constant at 1 the function is instead a nearly vertical line where minor desaturation of nodes causes large capillary suction pressure changes. Determination of the S_{lmax} value is difficult because it depends on a variety of factors, including the type of fluid phases, the solid matrix, and whether fluid is being injected or withdrawn (Fitts, 2013). Unless otherwise specified, our evaluations of model performance use the simplest formulation of $S_{lmax} = 1$. The refinement of this end member is an area for future exploration.

3.1.4   Fit of linear function

The function $P_c(n, S_l)$ is assigned as an explicit series of porosity-dependent linear interpolations between the coordinate points $(S_r(n), P_{cmax}(n))$ and $(S_{lmax}(n), 0)$. The slope of this line, m, is

$$m = \frac{-P_{cmax}(n)}{S_{lmax}(n) - S_r(n)} \hspace{6cm} \text{Eq. 7}$$

For purposes of fitting the function, the slope of the $P_c(S_l)$ line can be extrapolated to sat $= 0$ which gives an intercept b,

$$b = P_{cmax} + \left(\frac{P_{cmax}}{S_{lmax} - S_r} * S_r\right) \hspace{5cm} \text{Eq. 8}$$

Thus, for this simple linear model,

$$P_c = P_{cmax}, \hspace{0.3cm} sat < S_r$$

$$P_c = m * sat + b = \frac{-P_{cmax}(n)}{S_{lmax}(n) - S_r(n)} * sat + P_{cmax} + \left(\frac{P_{cmax}}{S_{lmax} - S_r} * S_r\right) \hspace{1cm} \text{Eq. 9}$$

$$P_c = 0, \hspace{0.3cm} sat > S_{lmax}$$

By keeping P_{cmax}, S_r, and S_{lmax} as separate calculations within the code, the function can be easily altered at a later time to allow changes in how these variables are calculated.

Experiments and Modeling to Support Field Test Design

Choosing arbitrary numbers as an example, the user enters initial porosity n_i, residual saturation S_{ri}, and capillary pressure at residual saturation P_{cmaxi} values of 0.35, 0.1, and 0.03 MPa, respectively. As porosity decreases, capillary pressures for any saturation value increase, and vice versa. In a case where S_{lmax} is allowed to change and the linear S_r function is used, the slope of the $P_c(S_l)$ line is constant (Figure 3a). If S_{lmax} is held at 1, then the slope of the line becomes steeper as porosity decreases (Figure 3b). When the nonlinear S_r function is applied with unchanging S_{lmax}, the slope of the $P_c(S_l)$ line becomes steep as porosity approaches zero, and capillary suction is negligible at high porosity (Figure 3c). If S_{lmax} is allowed to change, the slope for most porosities is similar to the linear S_r/changing S_{lmax} function in Figure 3a, but with divergence at low porosity (Figure 3d). In this last case, capillary suction is zero for most saturation values. One effect of the nonlinear S_r function is that it generates maximum pressure at higher saturations when porosity approaches 0 if the medium is not saturated. This tends to hold water in place at very low porosity.
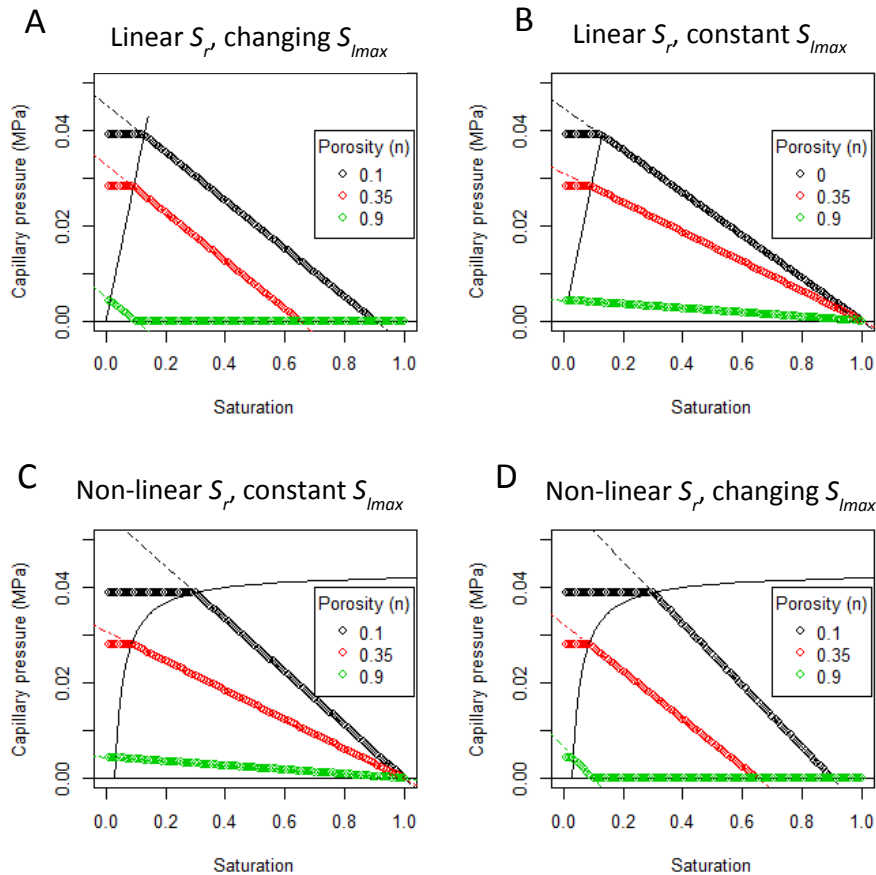
Figure 3: Calculated points for various capillary pressure (P_c) models. For all cases, n_i = 0.35, S_{ri} = 0.1, and P_{cmaxi} = 0.013 MPa. (a) Calculated with linear S_r and changing S_{lmax}; (b) Linear S_r, S_{lmax} = 1; (c) Non-linear S_r, S_{lmax} = 1; (d) Non-linear S_r, varying S_{lmax}.

3.1.5 Derivative function for updated timeste

Early implementation of the model experienced considerable inefficiency in achieving a solution (see Section 5) due to difficulties induced by the new function in choosing the initial guess for each timestep. Upon completion of the previous timestep, the model starts with a guess

at the condition for the subsequent timestep and then revises this guess in the solver iterations until equation residuals are minimized. The initial guess for an updated parameter A_1 is accomplished in most FEHM functions by taking the output parameter value A_0 of the previous timestep and the derivative of that parameter with respect to parameters B affecting that value,

$$A_1 = A_0 + \frac{dA}{dB} dB \qquad\qquad\qquad \text{Eq. 10}$$

For the P_c function described so far, no such derivative term is included. This causes the initial guess for the subsequent timestep to be just the output of the previous step which can be far from the final solver solution in the updated solution. As a result, the number of iterations per timestep can increase greatly, causing a consequent increase in the run time of the model.

To address this, the capillary pressure derivative parameter *dpcef* within the cappr.f module must be populated. A simple approach is to assume that each subsequent timestep has a capillary function $P_c(S_l)$ very similar to the preceding one, so that the *dpcef(i)* variable, where i is the current node, is defined as *m* from Eq. 7. Doing so revises the initial guess to closer to the likely final value and shortens run times considerably, although issues can still arise when porosity changes greatly within a timestep. Further refinement of this aspect is intended for future development but the present implementation is functional for small problems.

4 P_c function verification

In order to verify that the implemented $P_c(n,S_l)$ function is working properly, a series of tests were conducted. The first set of model runs was conducted on a small, 8-node problem to demonstrate that the P_c calculations were correct mathematically and produced proper results. This requires three steps: first, the calculation in FEHM must match the direct analytical calculation. Second, the results of the new linear function must match the existing linear functions if porosity is unchanged. Finally, the new function must yield different results from existing functions if porosity is changing.

4.1   8-node test of capillary suction
4.1.1   Grid parameters and model setup
A simple mesh consisting of 8 nodes was created (Figure 4). Each node is assigned a unique temperature in 10°C increments from 10°C to 80°C. This temperature gradient in conjunction with the *salt* macro functions induces a change in porosity. For mass flow, the edges of the domain are no-flow boundaries with only internal migration due to pressure differences allowed and no external sources of water. Vapor also migrates on vapor concentration gradients, with hotter areas of the domain producing higher vapor content. Each test model is run for ten days of model time. This generates unique porosity for each node with easy model convergence and varying results throughout the domain.
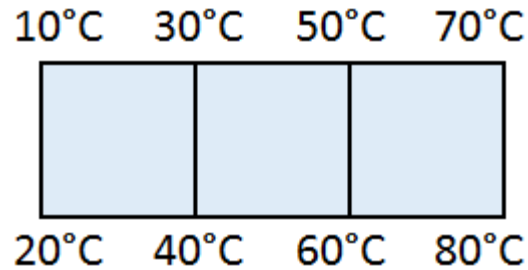
Figure 4: 8-node model domain for P_c verification. Edges are no-flow boundaries with respect to mass with constant temperature.

4.1.2 *Verification of P_c calculation*

FEHM can output the final P_c value at each timestep, but in order to test the in-progress calculations a customized file of P_c for each iteration was created by temporarily adding a print statement to the cappr.f function to output current node porosity, saturation, and the resulting capillary pressure. This file is not a normal part of FEHM and was deactivated for subsequent runs because an output for every calculation and every iteration produces files that can be many gigabytes large for a full run. Using the initial input values and these output values allows direct comparison of all P_c calculations within the model to equivalent analytical calculations conducted using the software package R. Given the same inputs, FEHM calculates P_c values that are identical to the analytical R values to the level of precision of the data storage type (Figure 5). Fortran variables underlying the FEHM calculations go to several more decimal points than the variable storage technique used in R, so very slight deviation on the order of 10^{-8} is observed but this is an artifact of data storage rather than a mathematical error. Based on this, FEHM is correctly calculating capillary pressure based on relevant inputs.
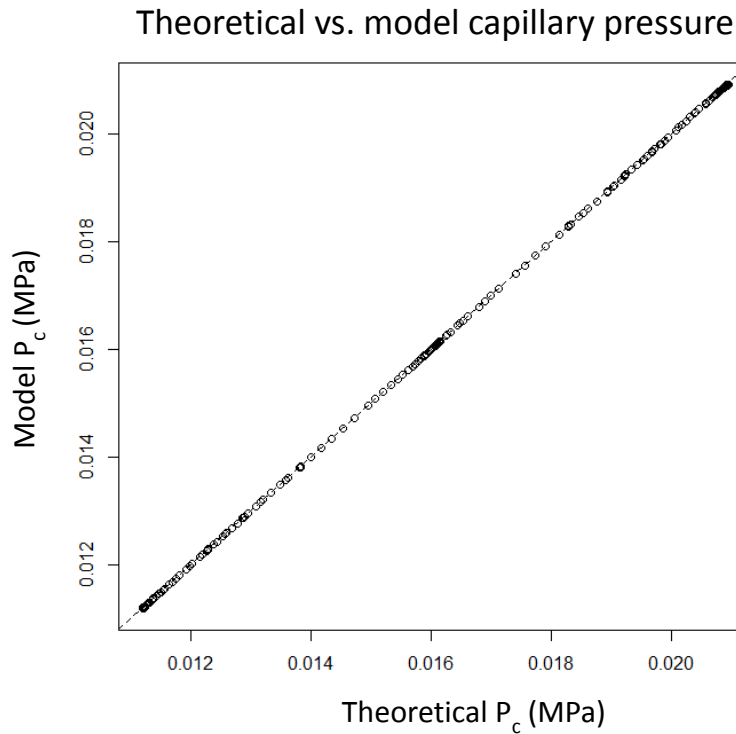
Figure 5: Capillary pressures based on input saturation and porosity calculated analytically in R (x-axis) vs. calculated using new function in FEHM (y-axis). Points fall on y=x line to within 10^{-8}.

4.1.3   *Constant-porosity comparison to linear rlp*

A second test was conducted in which porosity was not allowed to change. Capillary pressure and node saturation values in this context should be the same as a comparable setup using the linear rlp model already built into FEHM. During testing it was found that the values matched to within the variability of the convergence criteria applied in FEHM. Due to the explicit implementation of the $P_c(n, S_l)$ function, the model ran more slowly using the new function but yielded the same results to within 10^{-7} for final saturation for all nodes, well within the convergence criteria of 10^{-6} specified for the model, indicating that the model functions correctly and equivalently to the linear model for unchanging porosity (Figure 6a). With the applied derivative function, these values match exactly because the start point for the next guess is the same; lacking the derivative the initial guess is different so the final solver solution is slightly different. Capillary pressures reported from contour output files are likewise identical (Figure 6b).

Experiments and Modeling to Support Field Test Design
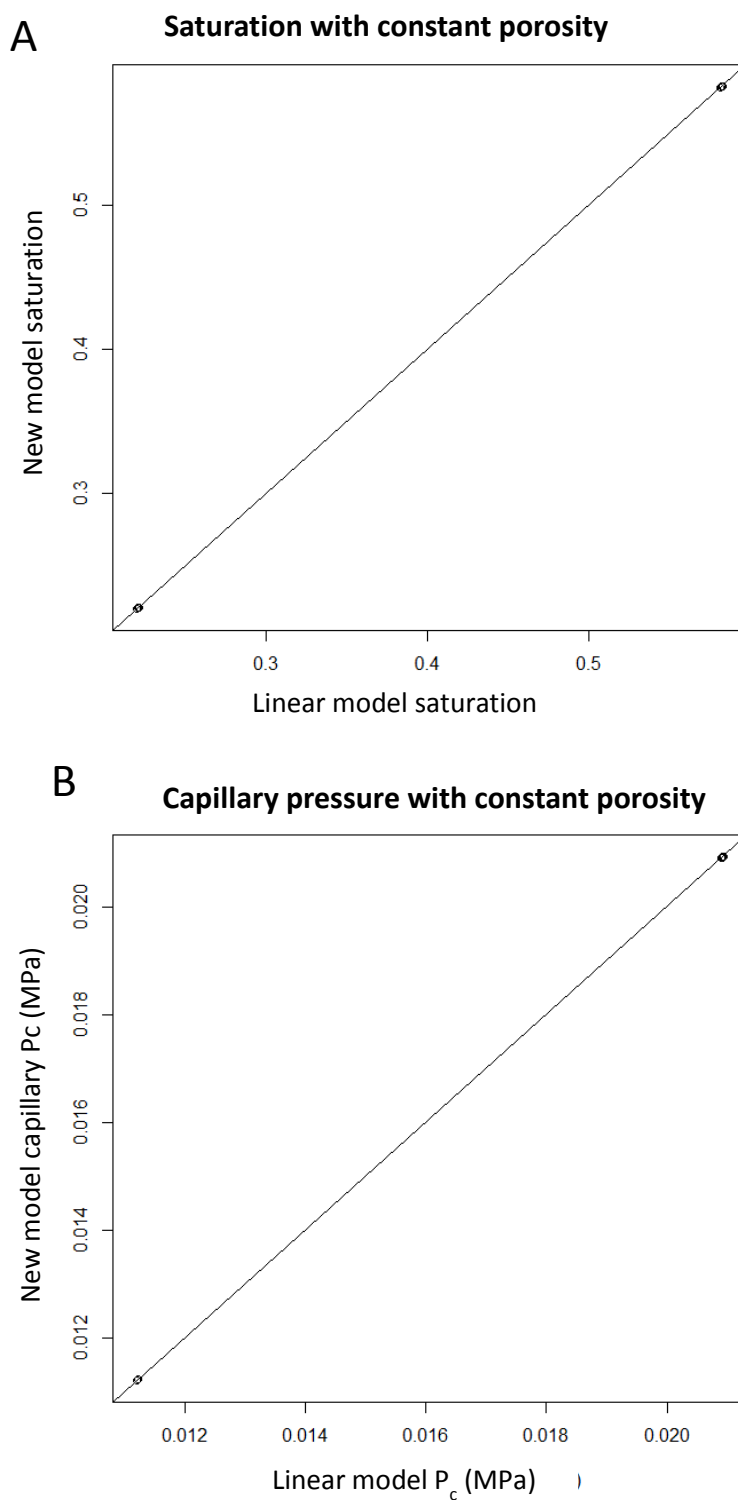
Figure 6: Comparison of linear model and new model with constant porosity. (a) Saturation values for each; (b) calculated P_c.

4.1.4 Changing porosity

The new porosity, saturation, and capillary pressure is output for each timestep. Allowing porosity to change should induce noticeable differences in the final node saturation values even with a minor change in porosity. When the new function is applied, results for saturation are on order 10^{-2} different for the nodes with greatest porosity change. As the convergence criteria are 10^{-6}, and the magnitude of difference in results with constant porosity was well within those criteria, this represents a considerable difference in result for this small scale. Since the capillary pressures are calculated correctly and the function produces clearly different results with changing porosity, it is apparent that the new function correctly changes capillary pressures and the consequent calculations of saturation and porosity are updated accordingly.

4.1.5 Summary

The updated capillary pressure function correctly calculates P_c for all nodes based on parameters sent to that function with each timestep. Results for constant porosity runs are similar to existing, successfully implemented linear functions already within FEHM, indicating that the numbers calculated in the new function are being correctly implemented in the same manner as the pre-existing model. Calculations with dynamic porosity are updating correctly and yield results that are noticeably different from the constant-porosity case.

5 Tall domain tests

5.1 Objective

Following completion of the simple 8-node problem, a more extensive set of tests was conducted on a tall, thin domain. The goal of this series was to examine a more complex problem with the new $P_c(n, S_l)$ functions with and without derivatives, compared to the old linear function, and determine whether applying the new function greatly affected model performance in terms of efficiency. We report model efficiency with regard to model duration (CPU run time) in seconds, the number of timesteps required to complete similar runs, the number of solver iterations, and the number of Newton-Raphson (N-R) iterations. Model duration is not the best measure of performance when differences in total time are small because the performance of individual processors depends on what else is happening with the computer, so that equally efficient model runs may have slightly different run times. However, greatly increased model time combined with more timesteps and/or more N-R or solver iterations can give intuition about the severity of model inefficiency.

5.2 Grid parameters and model setup

The mesh used for these tests is a 10 m tall, 1 m wide two-dimensional rectangular domain with 0.5 m node spacing (Figure 7). The x=0 and x=1 sides are no-flow boundaries with respect to both heat and mass. The top boundary is at atmospheric pressure and 5°C with a fixed saturation of 10^{-5}. A single node of 105°C fixed temperature is located at the origin.
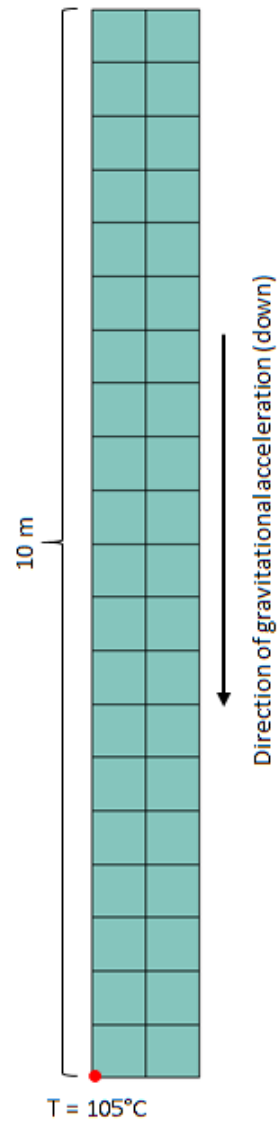
Figure 7: Tall model domain for Pc tests. Heat is input at the bottom (red dot) to hold the node at 105°C. The top of the domain is at atmospheric pressure and 5°C with a constant saturation of 10^{-5}. The sides are no-flow boundaries with respect to heat and mass.

5.3 Performance data

Ten tests were conducted: five with constant porosity and five with changing porosity. Model performance values are shown in Table 4. Applying the derivative function to the new model results in a significant improvement in model performance. Occasional timesteps still have difficulty converging but the overall number of timesteps, N-R iterations, and solver

Experiments and Modeling to Support Field Test Design

iterations is very close to the linear model values while matching within convergence criteria in final results to both other models. Further testing of the derivative-inclusive function is accomplished by having it handle larger timestep multipliers to determine if it is able to converge at similar levels. Since the no-derivative approach is clearly worse, it was not tested. The linear and derivative-inclusive functions were applied to both constant- and changing-porosity scenarios, with a timestep multiplier of 1.1. With constant porosity, the performance of the $P_c(n, S_l)$ model was slightly worse than the linear model but very close in timesteps, N-R iterations, solver iterations, and model runtime. With changing porosity, it performed much worse on all metrics than the linear model. The main reason for this is that a maximum timestep value is reached during which porosity changes are enough to require additional solver iterations to achieve a final solution. This is a consequence of the derivative being based only on saturation.

Table 4: Comparison of model performance with constant porosity and changing porosity. Comparison is made for number of timesteps, number of Newton-Raphson (N-R) iterations, number of solver iterations, and model run time in seconds. Models evaluated are the linear model with fixed timesteps, linear with a timestep multiplier (dt) applied, the new model with no derivative assignment, and the new model with derivatives with and without a timestep multiplier. The new model version without the derivative was not run with a timestep multiplier.

Constant porosity					
	Linear, no dt	New, no dt	New with derivative, no dt	Linear, dt	New with derivative, dt
Timesteps	10678	83078	10877	751	801
N-R iter	11379	179186	11907	1509	1724
Solver iter	41436	788342	45544	11451	14146
Time (s)	146	1575	145	16	18

Changing porosity					
	Linear, no dt	New, no dt	With derivative, no dt	Linear, dt	With derivative, dt
Timesteps	10726	83661	10744	802	4688
N-R iter	11444	178760	11569	1624	24223
Solver iter	42694	784311	45266	14993	155707
Time (s)	279	2897	292	39	242

5.4 Summary

Introduction of the porosity-dependent capillary pressure model has induced difficulties in model convergence under some circumstances. The variant with a pure explicit formulation of capillary pressure causes an order-of-magnitude increase in model run times, N-R iterations, and solver iterations that cause even a relatively small, simple model to be lengthy and have difficulty achieving a solution. Adding a derivative with respect to saturation of the capillary

function aids in improving model efficiency as long as timesteps do not grow enough to where porosity changes within a timestep are great. Tests of the new function on larger meshes continue and will be presented in a future milestone.

6 Olivella Experiment Modeling

6.1 Experiment description

Early brine and multiphase movement of fluids in response to heat remains a critical focus for in-drift disposal of HGNW in salt. The interactions between radiogenic heat, moisture content, brine chemistry,salt dissolution or precipitation, and mineral reactions may lead to complex changes around waste packages prior to the plastic closure of a salt gallery and are important for the overall self-sealing behavior of a salt repository (Kuhlman and Malamba, 2010). At the micro scale, experimental studies have demonstrated that porosity may migrate towards a thermal source (Caporuscio et al., 2013). At larger scales where mixed-phase flow is present in connected pores, brine may evaporate and the vapor-rich gas migrate away from pores, resulting in a migrating porosity front that moves away from the heat source over time (Kelly, 1985; Hansen and Leigh, 2012; Jordan et al., 2015c). Evaporated water, however, tends to condense as temperature decreases, resulting in dissolution of salt farther afield and increases in porosity and permeability. Previous experimental work (Olivella, 2011) was undertaken to examine this migration of porosity away from a heat source.

The Olivella et al. (2011) experiment used an insulated Plexiglas tube with a length of 10 cm and diameter of 5 cm (Figure 8) filled with crushed salt. One end of the tube was heated to 85 °C and the other end cooled to 5 °C. Measurements of porosity and brine content were taken at initial conditions and times of 7 days, 15 days, 30 days, and 65 days. We use a simple model domain based on this setup as a test for new features in FEHM that relate to salt.

It should be noted that uncertainty has been identified in the Olivella et al. (2011) experimental results that renders experimental data presented in their late periods suspect. In their work, porosity and brine content (porosity $\times$ saturation) were reported. Integrating those values based on the plot for each time period shows a gradual increase such that the end condition has about 147% brine content compared to the start of the experiment (Figure 9). For the total difference in water content and the 65 day considered time, this amounts to a constant addition of about $7.3 \cdot 10^{-9}$ kg/s of new water. Although it is unclear what exactly is happening in this experiment, this suggests that there may have been a leak in the capsule through which water entered the experiment. One possibility would be vapor diffusion from the room into the cold end of the experiment, a process that would add a small condensation flux. If this was the case, porosity changes due to temperature would be compromised by the extra water. Consequently, we compare our model results to early periods of the experiment when additional water may not have accumulated.

Experiments and Modeling to Support Field Test Design
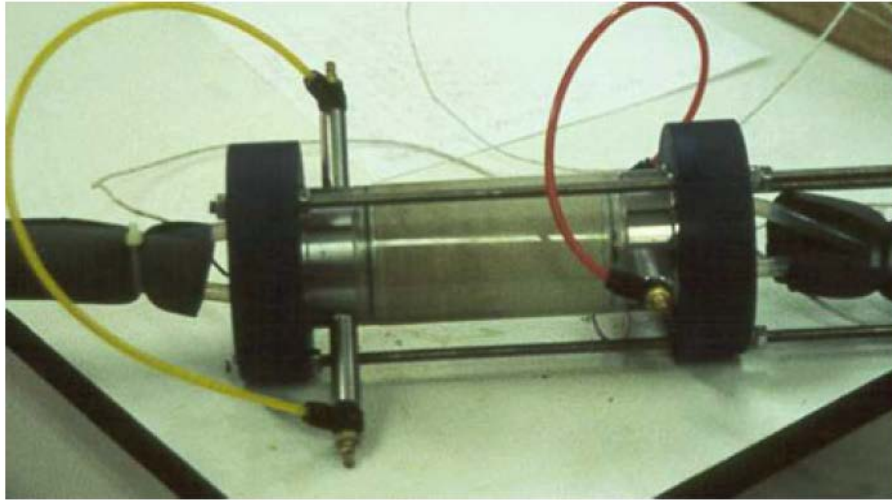
Figure 8: Experimental setup from Olivella et al. (2011).
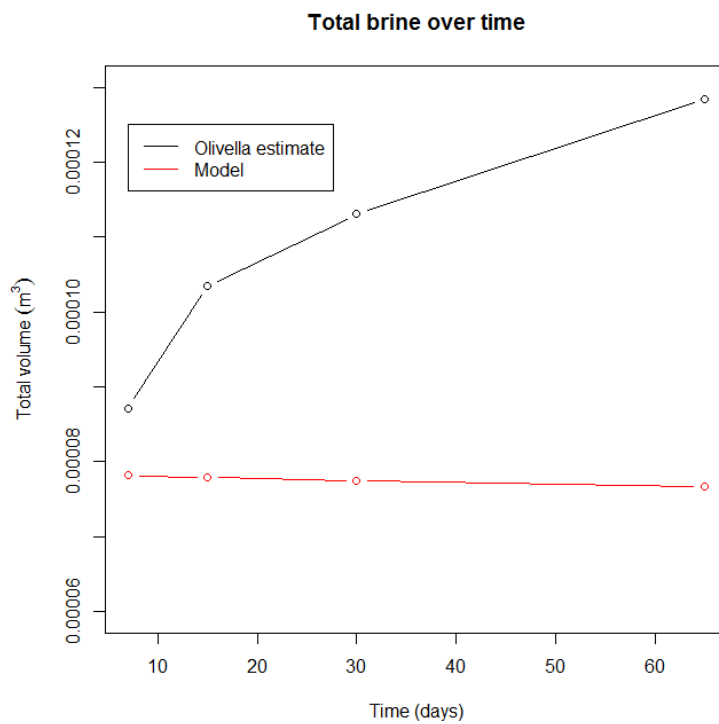
Figure 9: Scaled Olivella et al. (2011) total water volume compared to model total water volume. Experiment results show an overall increase of 47% compared to initial conditions, suggesting a system that was not completely closed. Model results show a very slight decrease in water content due to increase in average temperature of domain, which transitions liquid brine to vapor.

Experiments and Modeling to Support Field Test Design

6.2 Model setup

A simple two-dimensional mesh was generated that has 33 total nodes in an 11 by 3 node setup. Spacing between each node was 0.01 m (1 cm). Typical parameters for crushed salt were assigned to all nodes (Table 5). Based on results from Bourret et al. (2016), the insulating layers were treated as no-flow boundaries because very little heat and no mass passes through them. To test the new capillary function, four different runs were conducted: (1) a control run with capillary effects disabled ($P_c = 0$ for all timesteps); (2) A simple linear capillary function with unchanging porosity; (3) A tabular capillary function based on retention curves presented in Olivella et al. (2011), and (4) the new $P_c(n,S_l)$ function. As an additional control, a run was conducted using the linear capillary function but with an impermeable ($k = 10^{-22}$ m^2) domain. Vapor diffusion was still allowed but liquid brine could not migrate back toward the hot end. Each model was run for 65 days. Porosity, temperature, and saturation were output at 7, 15, 30, and 65 days.

Table 5: Salt properties used in modeling.

Property	Value	Units
Solid density	2165.0	kg/m^3
Specific heat capacity	931.0	J/kg·K
Permeability	1×10^{-12}	m^2
Thermal conductivity	2.0	W/m·K
Porosity	0.3	-
Initial saturation	0.4	-

6.3 Comparison of Pc models

We evaluate four different capillary models: the new porosity-dependent model, the old linear model, a tabular model based on Olivella et al. (2011) which is applied using the *rlpm* macro, and a model run where capillary suction effects are disabled. We compare porosity, temperature, brine content, and capillary pressure for each model. As described in subsequent sections, the tabular and linear models produce nearly identical results. The close match of tabular and linear models suggests that a linear approximation is valid; changing porosity is beneficial to refine this but the essential linear structure of a linear approximation is useful for this problem. However, it should be noted that the domain does not reach either very high or very low saturation where the capillary pressures in the linear and tabular models diverge from each other.

6.3.1 Brine content

Taking the product of porosity × saturation for each node following Olivella et al. (2011) yields the node brine content for each model (Figure 10). The linear and tabular models are nearly identical in their results. The new model shows a slight shifting of water in the direction of the heat source. This is logical because of the strengthening of capillary suction in this region due to reduced porosity. The slight increase in porosity in the colder half of the domain reduces capillary suction leading to less water being pulled toward the cold end. All of the active capillary models are very different from the run with capillary effects disabled. In the latter case, the water near the heat source completely vaporizes, with abundant condensation in the middle and into the colder areas of the model domain. Lacking capillary suction causes brine to remain where it condenses instead of being distributed throughout the domain.
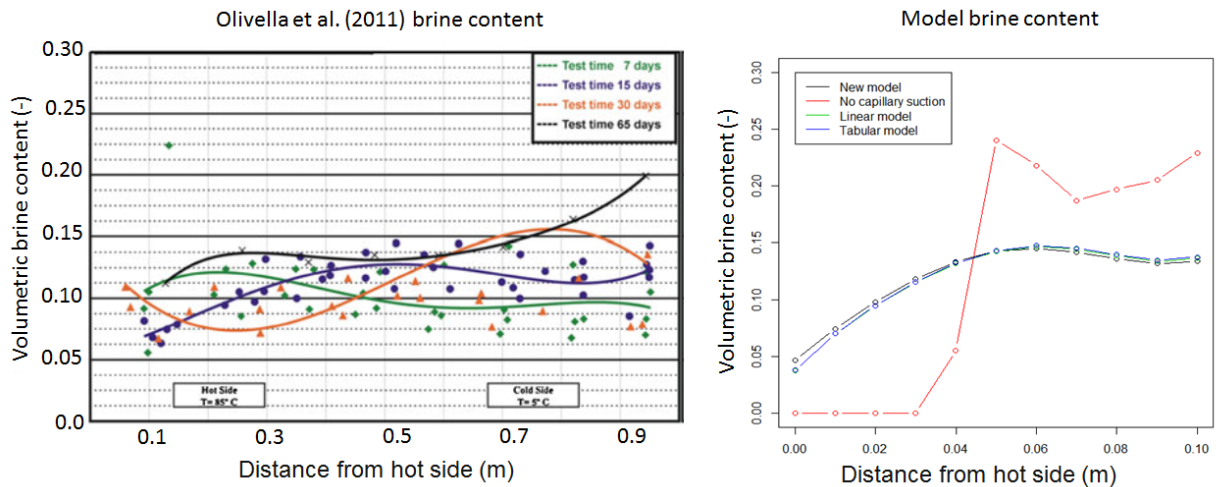
Figure 10: Experiment brine content values from Olivella et al. (2011) (left) and model brine content (right). Model values are node brine content through center of model domain with no capillary suction (red), linear and tabular models (green and blue), and new porosity-dependent model (black).

For the active capillary models, the brine content after 65 days is similar to the reported Olivella et al. (2011) values after 15 days. As discussed, this is a better comparison than the 65 day values because of the additional water entering the physical experiment.

6.3.2 Porosity

65-day porosity for each model is shown in Figure 11. Initial porosity for all nodes in all runs was 0.3. With capillary suction disabled, there is little change in porosity throughout the domain. The other models are all similar in that they show a considerable decrease in porosity near the heat source, a general increase in the middle, and a slight increase towards the cold end with a final upswing at the cold boundary. The linear and tabular formulations have shown a tendency to lower porosity slightly too much at the hot side compared to the early Olivella

experimental results. Near the head source until about 6 cm towards the cold side matches the 15-day experiment results closely; the closer to the cold end diverges, possibly as a consequence of the hypothesized leak in the tube which allows water to enter and increases saturation at this end. The increase in capillary suction in the new model raises the hot-side porosity very slightly to a value closer to the experimental values (Figure 11). Conditions at the heater itself were not recorded in Olivella et al. (2011). In general the new function causes a small but noticeable shift in porosity towards the heat source, and limits the magnitude of the porosity increase in the center of the domain slightly.
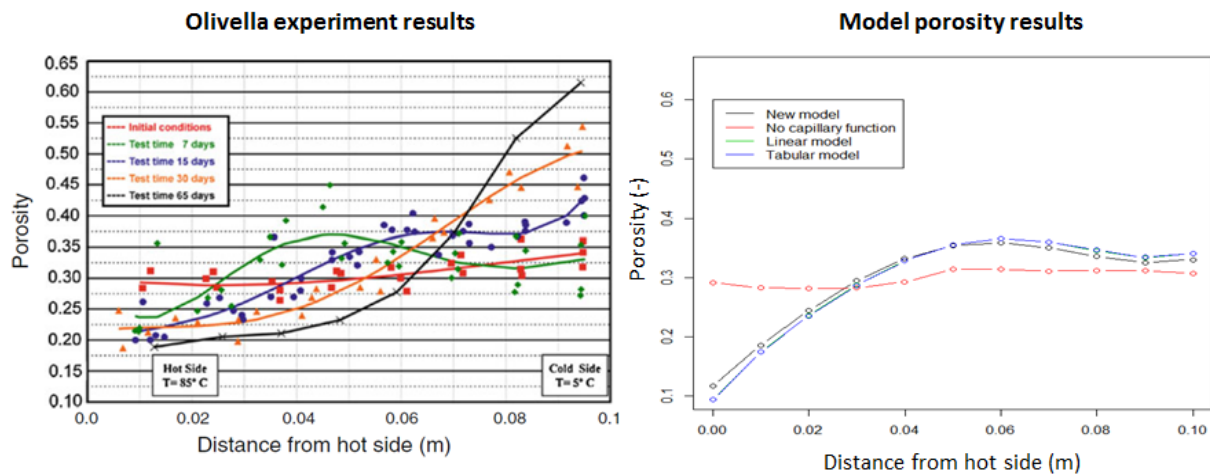
Figure 11: Comparison of FEHM model porosity after 65 days with various capillary models (right) to Olivella experimental porosity results. The new P_c model raises hot-end porosity slightly to closer to experimental values. Cold end experimental results are questionable because of apparent addition of water to experimental domain.

Based on the porosity and the brine content shown in Figures 11 and 12, it is apparent that the capillary suction pulling water back towards the heat source is vital to establish a feedback system to reduce near-heat porosity. As additional evidence of this concept, porosity results for an impermeable run with the linear capillary model more closely match the results with no capillary forces than they do with the linear model and normal permeability (Figure 12). The runs with no backflow towards the heat source rapidly attain a stable porosity that is barely different from the initial condition, and then experience no further change. This suggests that further study on proper assignment of the capillary function may be warranted, but also suggests approaches for modeling of larger domains. In particular, many FEHM applications to salt have included dense wall rock with very low porosity and permeability. In these cases, the permeability is sufficiently low that the choice of capillary model makes very little difference. These models may be increased in computational efficiency by simply excluding the capillary effect in those regions.

Model porosity comparison
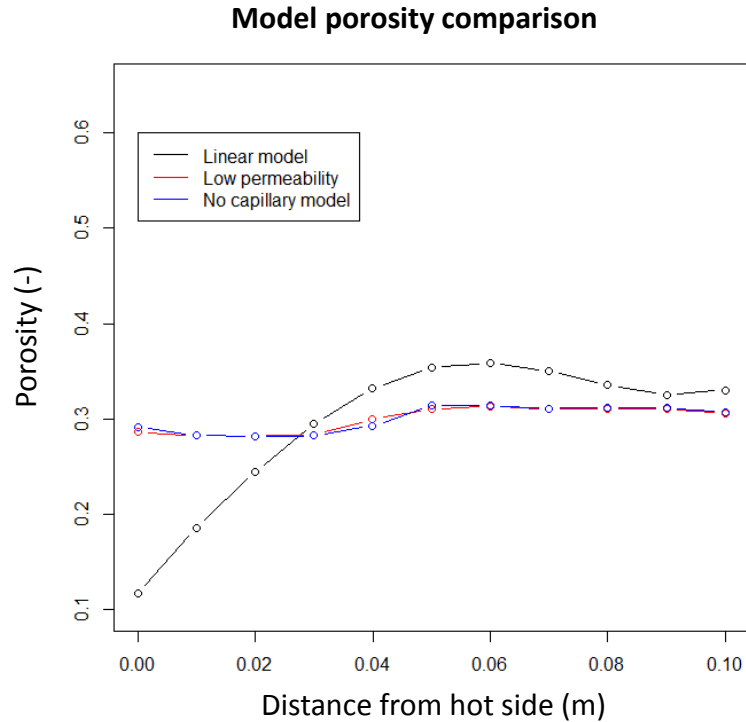
Figure 12: Model 65-day porosity for linear capillary model (black line), linear model with very low permeability (red line), and no capillary suction applied but normal porosity (blue line). Impermeable and no-capillary models show close overlap, suggesting that suction-induced recharge of hot-side nodes is critical to establishing continuous changes in porosity.

6.3.3 *Temperature and heat flow*

Brine temperature profiles from the heated side to the cold side are similar for all models with capillary suction effects, with a different and more linear profile for the run with disabled capillary effects (Figure 13). The primary influence of all non-zero capillary models is to contract heat towards the hot end of the tube. Temperature in the no-capillary case follows a linear gradient.

For further insight, we compare the energy transfer rates for the impermeable run in comparison to the permeable, capillary-driven cases. This can be accomplished by using the direct numerical output from FEHM in terms of the enthalpy balance for each timestep and for the overall run. Since the boundaries are held at constant temperature instead of a constant input or discharge of enthalpy, the total heat flux is different. The ratio of the heat transfer rates U with fluid flow compared to the no-flow case yields a dimensionless parameter, Nu*, similar to the Nusselt number, or ratio of convective to conductive heat transfer,

$$Nu^* = \frac{U_{flow}}{U_{noflow}}$$

Eq. 10

Experiments and Modeling to Support Field Test Design

Comparing the $P_c(n, S_l)$ model to the impermeable case yields a Nu* of 0.968, indicating slightly less efficient heat transfer when fluid is able to migrate. This seemingly counterintuitive result is a consequence of the dissolution in the center of the domain of the salt which has a high thermal conductivity relative to the fluid phases. Strong convection cannot occur in this small domain with low flow velocities and small height, so the heat transfer is dominated by conduction. Temperature-dependent thermal conductivity follows Clayton and Gable (2009) and porosity-dependent conductivity follows Bechthold et al. (2004); these two factors together reduce conductivity of the salt in the dissolved section, requiring a steeper driving gradient to reach thermal equilibrium between the hot and cold ends. Brine content is also decreasing slightly, further inducing a mild increase in the amount of relatively less conductive vapor in nodes experiencing dissolution.
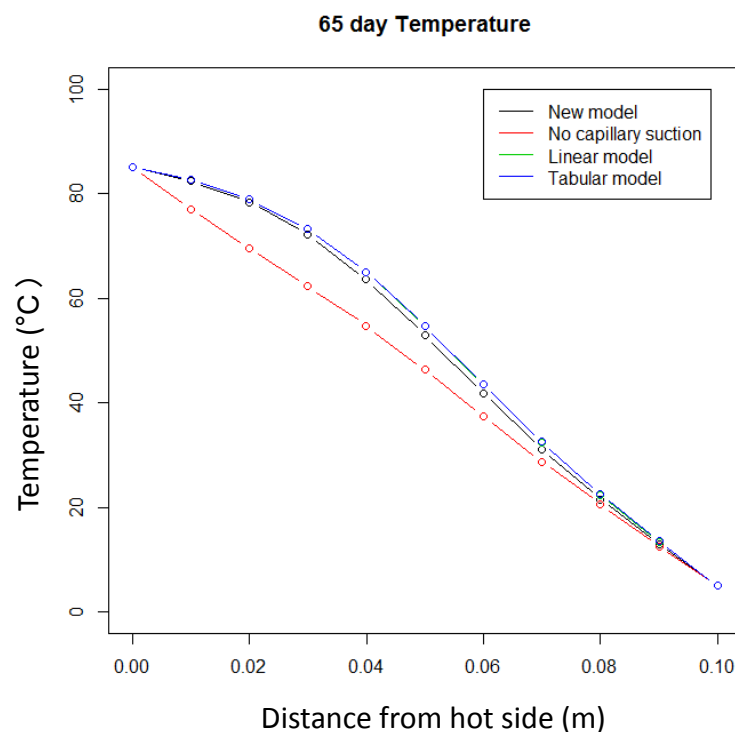
Figure 13: Temperature profiles for new suction model (black), model with no capillary suction (red), linear capillary model (green), and tabular model (blue).

6.4 Evaluation of new P_c model performance

The new $P_c(n,S_l)$ model presents an improvement in its analysis of the low-porosity behavior of the model compared to the old models. As discussed in Olivella et al. (2011), the experimental results showed a mild decrease in porosity near the hot end of the tube and a considerable increase in porosity at the cold end. FEHM has tended to slightly overestimate the extent of pore closure near the hot end of the tube. The increase in capillary forces as porosity

drops, due to the implementation of the new model, draws more brine toward this end relative to the old capillary model, keeping saturation higher. A small amount of salt is also dissolved during the return flow, as lower temperature water is below solubility equilibrium when it moves to higher temperatures. Consequently, porosity at this end is closer to the values reported in the experiment. 65-day model porosity is comparable to the 7-day experiment porosity and varies from the Olivella et al. (2011) 65-day results. Brine content (Figure 10) is similar to the 15-day experimental values, and remain similar throughout the runs with closed boundaries. Replication of the 65-day experimental is not possible in a closed system, and uncertainty remains concerning the sealing of the experimental tube which likely affected experimental results.

6.5 Analysis of physical processes

Based on the previously reported model results, an enhanced discussion of the physical processes driving the porosity migration in brine is possible. As suggested by Caporuscio et al (2013), Jordan et al. (2015a), Rutqvist et al. (2016), Bourret et al., (2017), and others, the evaporation of brine near a heat source and condensation of brine as it moves away and cools causes porosity to migrate away from the heat source so long as sufficient permeability is present for vapor to transport. As brine evaporates near the heat source, more fluid is drawn toward the heat source by capillary forces. This feedback effect allows a constant recharging of available dissolved salt which in turn causes porosity to further decrease. The close agreement between no-suction and impermeable runs clearly indicates that this particular recursive system has a huge effect on the final state of the system, with capillary suction forces serving to evenly distribute porewater from the center of the domain outward. Compounding this effect with the new model is even greater capillary suction at the hot end as porosity further decreases, and the relatively reduced suction in the middle which allows a small portion of condensed brine to be drawn towards the cold side. In the low-permeability case, local equilibrium is achieved and no further changes result; the lack of water migration means that brine content does not change once the local fluid temperature is equal to the ambient salt temperature and the brine is fully saturated with salt. In the absence of capillary suction but with a permeable system, water boils off near the heat source and condenses in the middle of the domain, but the lack of suction pulling water back means in effect that this process can only happen once.

Extrapolating this modeling to a larger system, the ability of the crushed salt around a heat-generating canister to draw water towards the heat source is a critical consideration for evaluation of the early period of HGNW disposal. For example, for a canister emplaced in a borehole carved into dense, low porosity, impermeable salt, this feedback system would be unlikely to have a major effect. For in-drift disposal, however, this suggests that a low-porosity, low-permeability rind could form around a canister due to suction effects constantly pulling brine in to replace evaporated brine. This concept is further tested and discussed in Section 9.

7 Simulations supporting a borehole heater test

7.1 Background

This section describes simulations created to support a new round of DOE-NE funded field testing in salt. In the phased field testing approach (Stauffer et al., 2015; Kuhlman et al., 2017, plans call for starting with horizontal boreholes containing heaters designed to isolate phenomena such as brine and vapor migration and geomechanical effects. Additionally, the tests will allow a new generation of scientists to become familiar with work in the underground, including testing new equipment in the harsh environment of a deep, geological salt formation (e.g. WIPP). FY17 work on this project included preliminary training and scoping visits to WIPP to explore options for initiating borehole experiments.

Based on a consensus of scientific opinion, the borehole heater design consists of a central sub-horizontal 10.2 cm diameter borehole containing a heater (Figure 14). Sub-horizontal boreholes were chosen instead of vertical boreholes to limit the geological complexity, allowing the borehole to follow the Map Unit 0 (MU-0) horizon which should avoid major mapped clays and anhydrites. The central borehole is surrounded by smaller diameter (5.1 cm) observation boreholes to allow measurements to be taken during the heater test. The deviation from true horizontal will be low, with just enough of an angle to ensure that water does not pond near the heater.
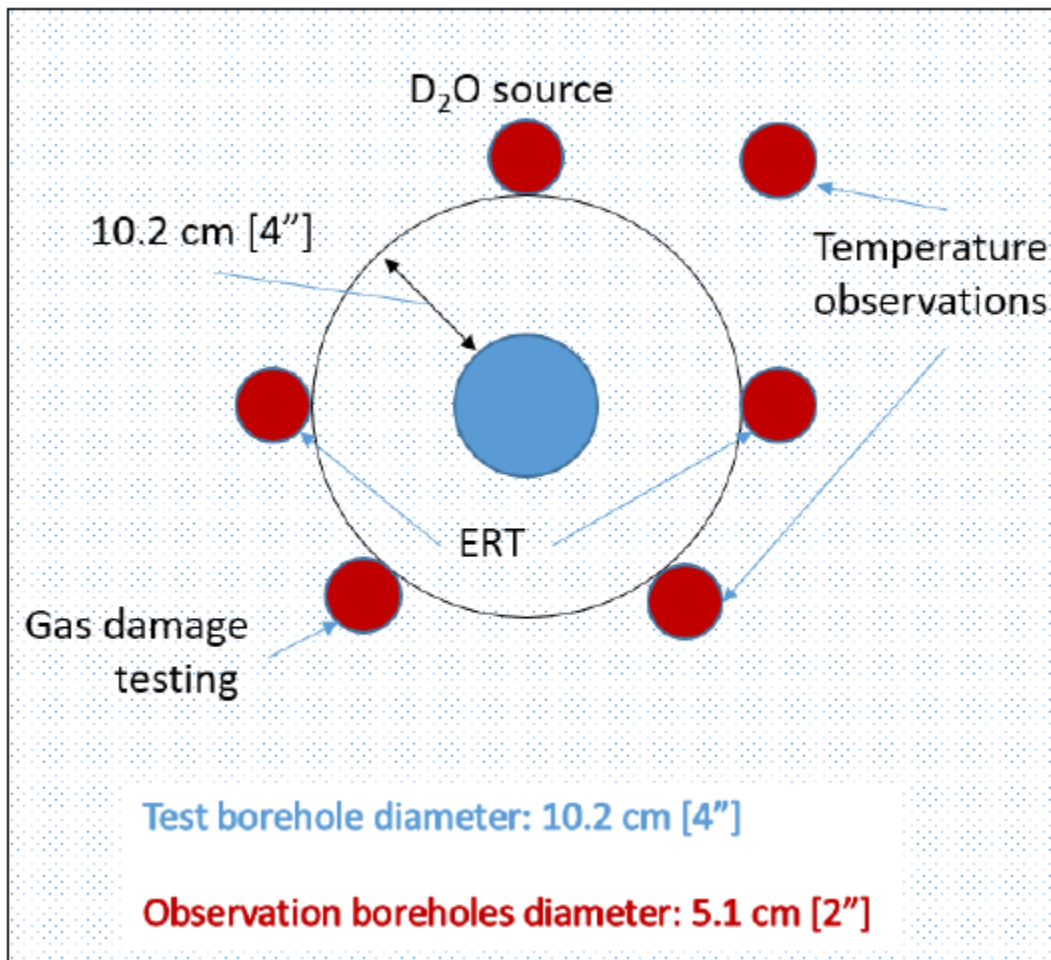
Figure 14: Borehole test concept after Kuhlman et al. (2017) Figure 7.

The heater element is planned to be isolated by an inflatable packer on order of 3.5 m deep in a 6.1 m borehole to avoid impacts of damage associated with primary drifts damaged rock zone (DRZ). A side view of the experimental plan is shown in Figure 15. Further, in some configurations of the experiment, dry nitrogen gas will flow through the heated section to evaporate any water that flows into the borehole, allowing water inflow mass to be measured.

Experiments and Modeling to Support Field Test Design
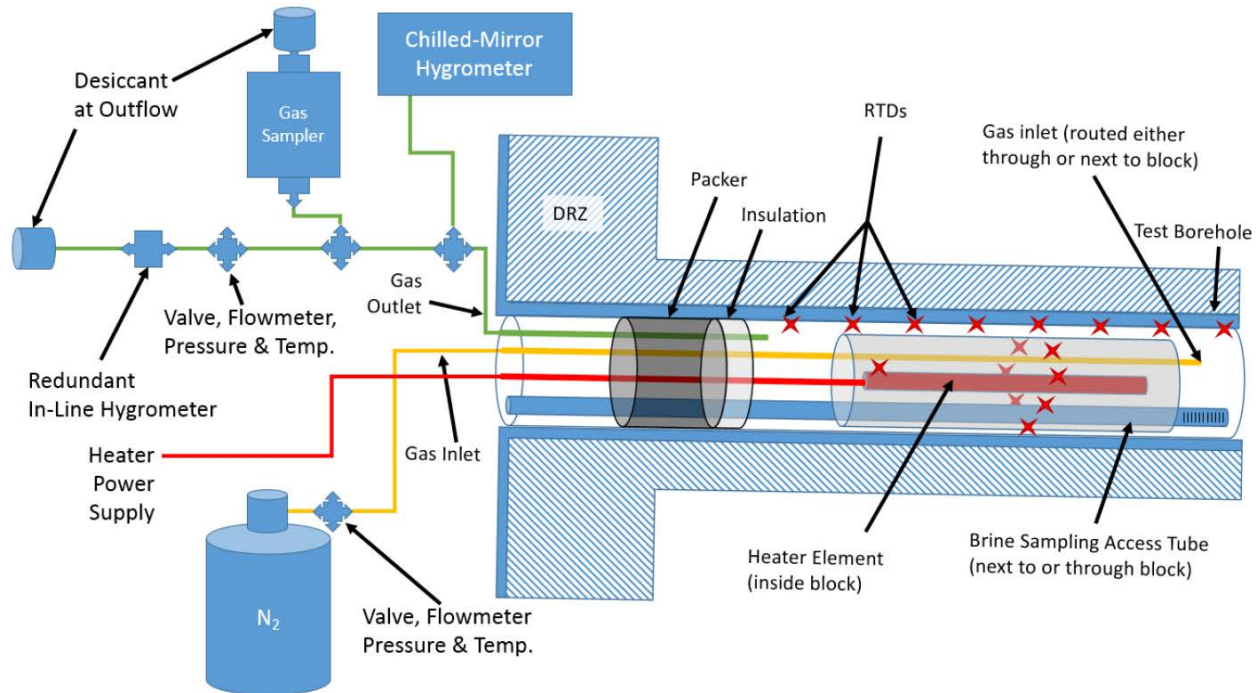
Figure 15: Schematic of borehole test equipment, after Kuhlman et al. (2017) Figure 8.

7.2 Numerical Mesh

A 3-D numerical representation of the proposed borehole test design has been created using the LaGrit (lagrit.lanl.gov; Miller et al., 2007) mesh generation software. Figure 16 shows the conceptualization of the experimental design. The numerical domain is centered on the borehole where the borehole enters the drift wall (x=y=z=0.0 m). The mesh extends 3 m across the vertical and horizontal drift face where the borehole enters the rock salt drift wall, and 7 m into the rock salt. A numerical mesh, with higher resolution near the central borehole was generated from this conceptual template (Figure 17). The final mesh contains 238107 nodes with a fully conforming Voronoi geometry. A 20 cm long section of the central borehole was identified to represent the heater cartridge, running from 3.5 to 3.7 m from the drift face, (Figure 18). The red ring on the brown borehole in Figure 16 shows the location of the heater cartridge.

Experiments and Modeling to Support Field Test Design
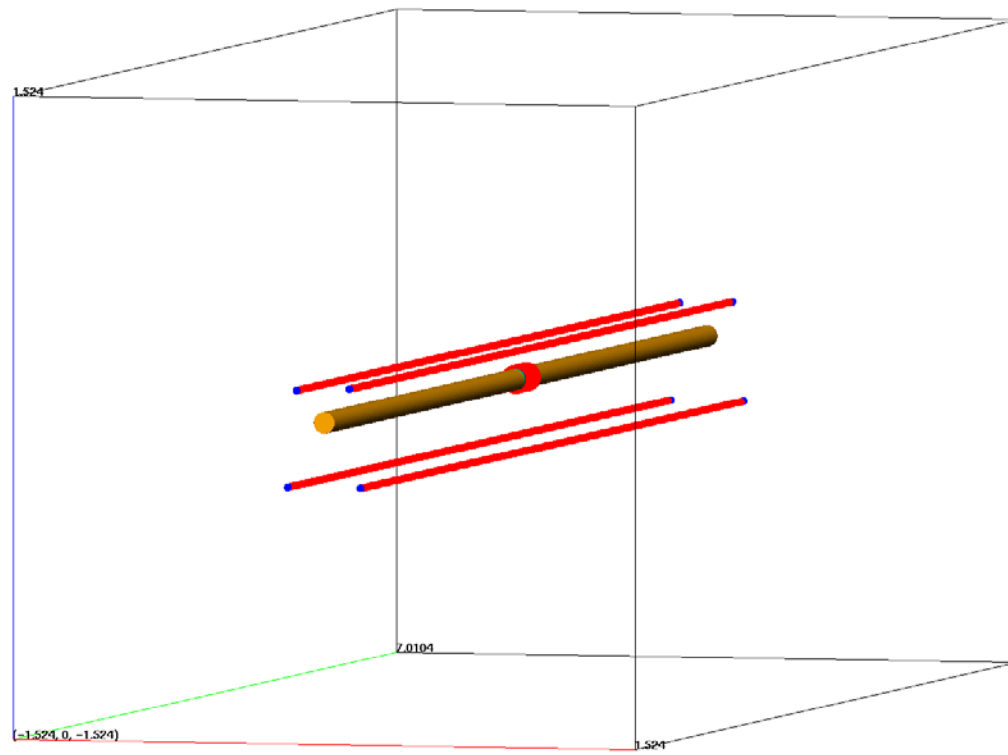
Figure 16: Test conceptualization. Observation boreholes (red) surround the primary heater borehole (brown).

Experiments and Modeling to Support Field Test Design
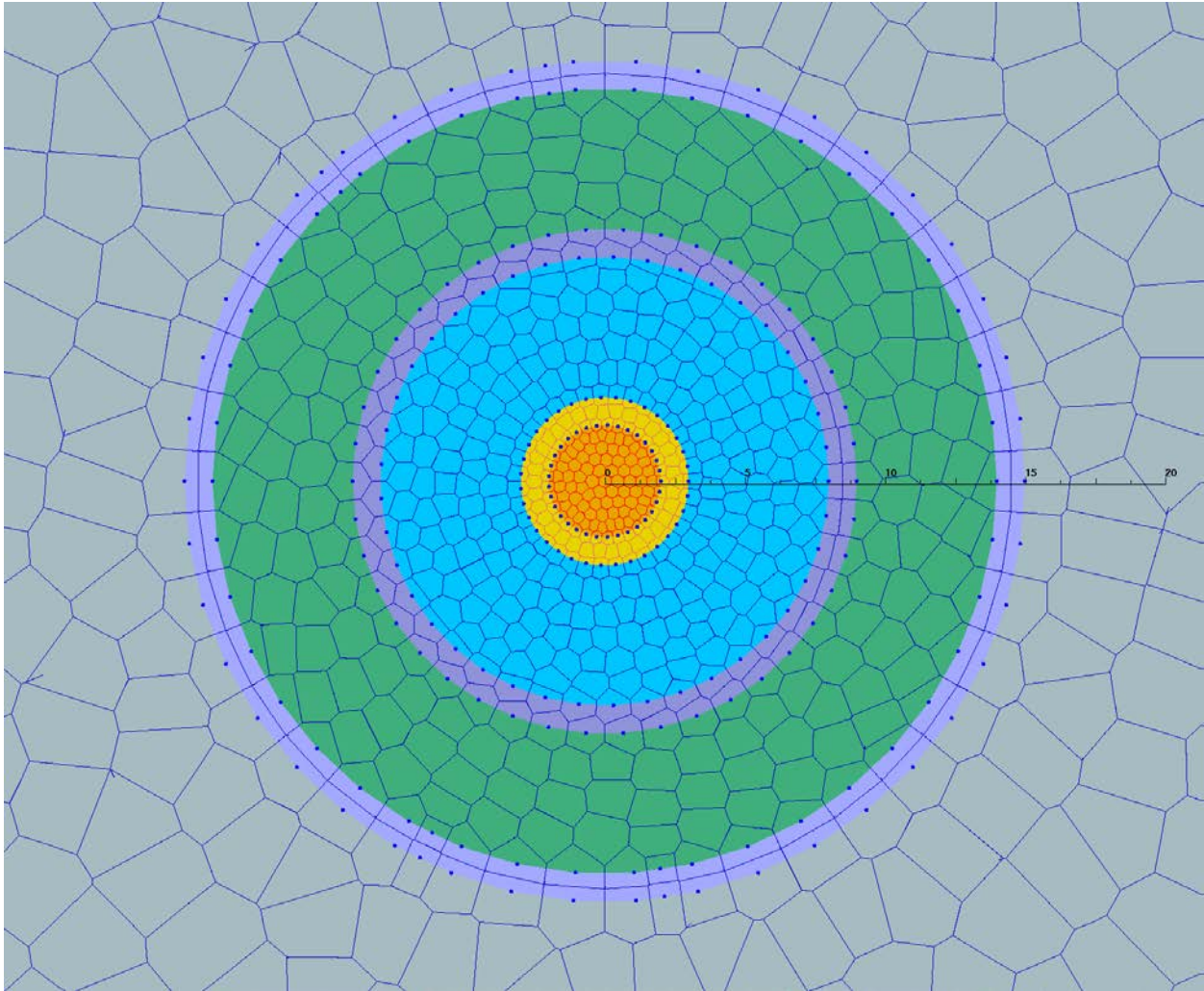
Figure 17: High-resolution interior of the numerical mesh (vertical slice through the borehole).
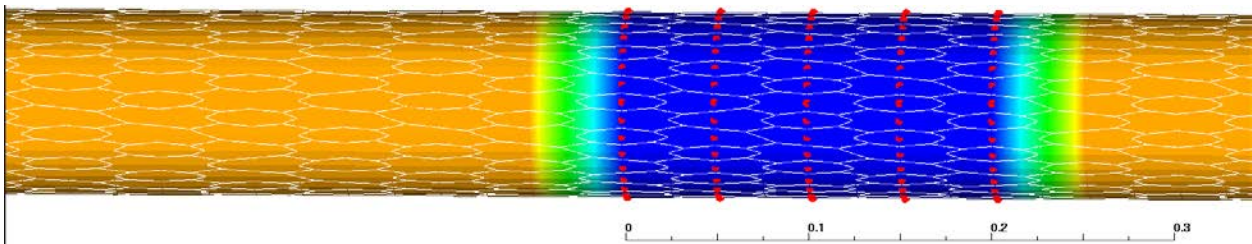
Figure 18: 20 cm section of the central borehole chosen to represent the heater cartridge.

7.3 500W Heater example

This example demonstrates conditions desired for the first heated test described in Kuhlman et al. (2017). Maximum temperatures are chosen to remain well below 150 °C (Figure

Experiments and Modeling to Support Field Test Design

19) and be low enough to avoid complications caused by decrepitation and hydrochloric acid generation.

In this example, the far-field is held constant at 28 °C, while the heater canister is loaded with 500W evenly distributed over the 515 nodes within the heater zone. Material properties of the rock salt and borehole air are given in Table 6. Thermal conductivity of air was increased from static conditions of 0.03 W/(m K) to 0.5 W/(m K) to represent possible radiative/advective transfer of heat in this region. The thermal conductivity function for intact salt is described in Stauffer et al. (2013). For the initial temperature calculations presented here, several simplifying assumptions were made, including the lack of a DRZ in the borehole, very low permeability of intact salt, and near full saturation in the low porosity intact salt. Precipitation and dissolution were also turned off for these simulations. The initial state was an isothermal block at 28 °C and background 0.1 MPa pressure. Thus, no flow of brine driven by background pressure gradients was generated in these runs.

The time evolution of temperature in the domain is shown in Figure 20, with steady state reached quickly in a little over 10 days. This is not surprising given the high thermal conductivity of the intact salt. Temperature perturbations in the top (t) and bottom (b) observation boreholes are shown starting at the center of the heater canister (Y=3.6) and progressing out to 1 m from the edge of the canister (Y= 4.7 m). Measurable perturbations at these distances give guidance for placement of thermocouples in the observation boreholes.

Table 6: Material parameters of borehole model units

	Initial density (kg/m^3)	porosity	Permeability (m^2)	Thermal conductivity (W/m K)	Heat Capacity (J/(kg K))	Initial Saturation %
Borehole air	1.2	0.999	1e-12	0.5	0.46	0.1
Intact Salt	2165.	0.001	1e-22	Function (Stauffer et al., 2013)	931.	99.5
Heater	2230.	0.1	1e-12	15.	710.	0.1

Experiments and Modeling to Support Field Test Design
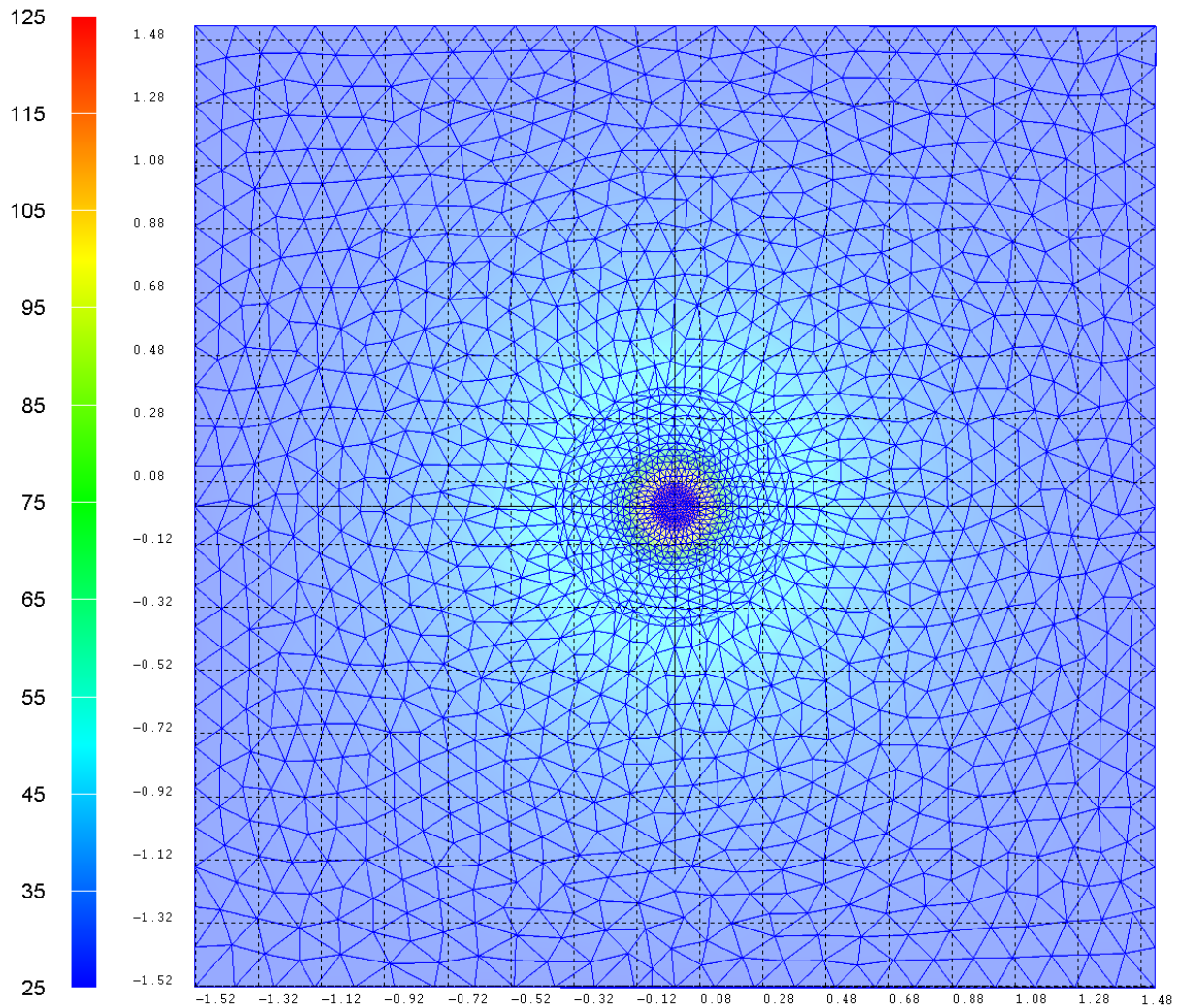
Figure 19: Temperature in the 500 W heater example at 90 days.

Simulated temperatures in near-field to the heater are shown in Figure 21, where there is a fairly sharp contrast between the heater (red) and the surrounding wall rock at lower temperatures (120 °C) in yellow. Interestingly, these simple simulations do include vapor transport, with water being evaporated from the wall rock in a region out to approximately 0.15 m as shown in Figure 22. The drying leads to increase in capillary pressure and a corresponding decrease in water pressure shown in Figure 23.

Experiments and Modeling to Support Field Test Design
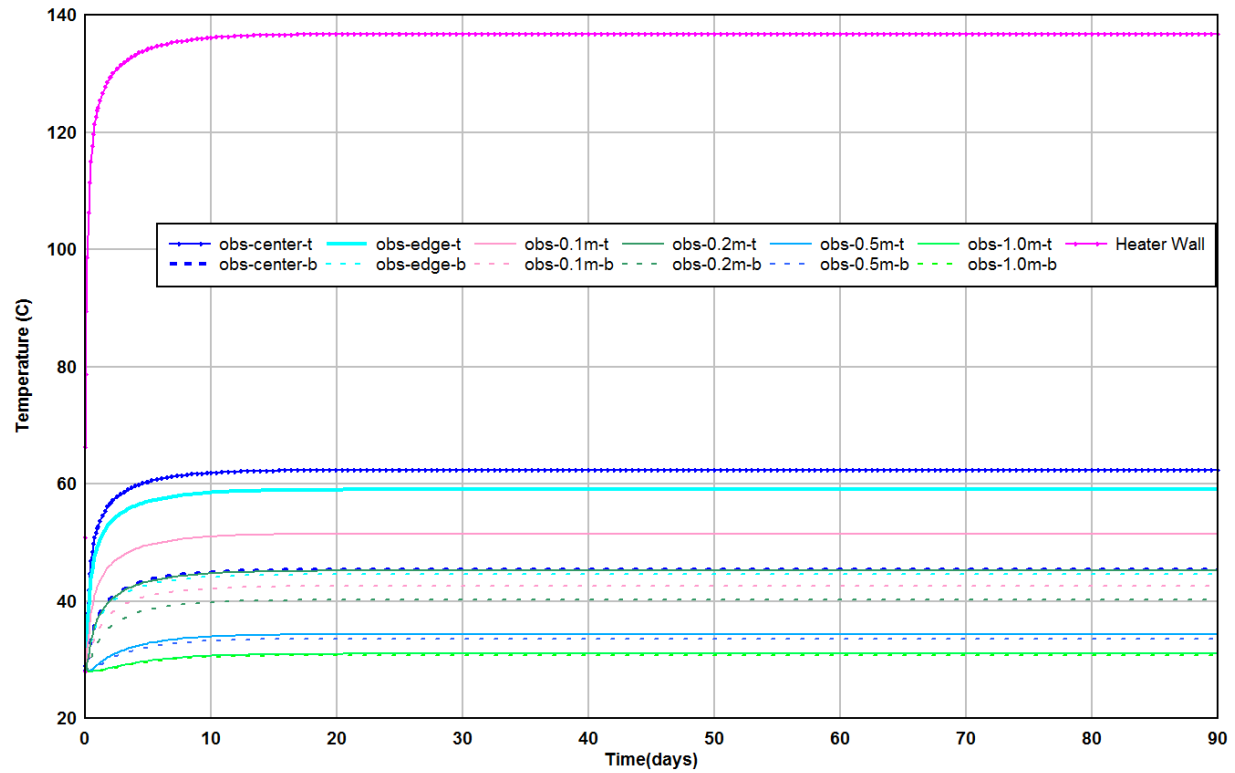
Figure 20: Temperature in the 500 W heater example for points in the top (t) and bottom (b) observation boreholes (obs) and one point at the intersection of the heater and the borehole wall.
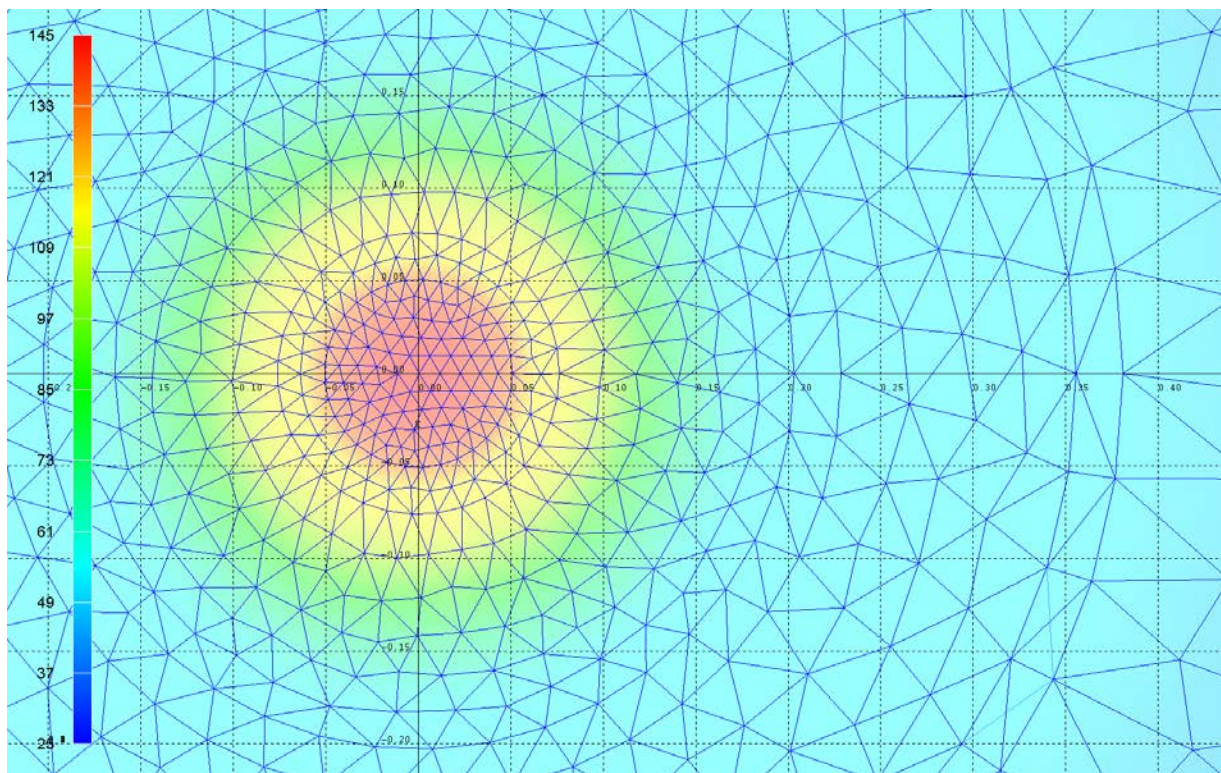
Figure 21: Near-field temperature around the heater (-0.05 to +0.05 m) at 90 days with 500 W.

Experiments and Modeling to Support Field Test Design
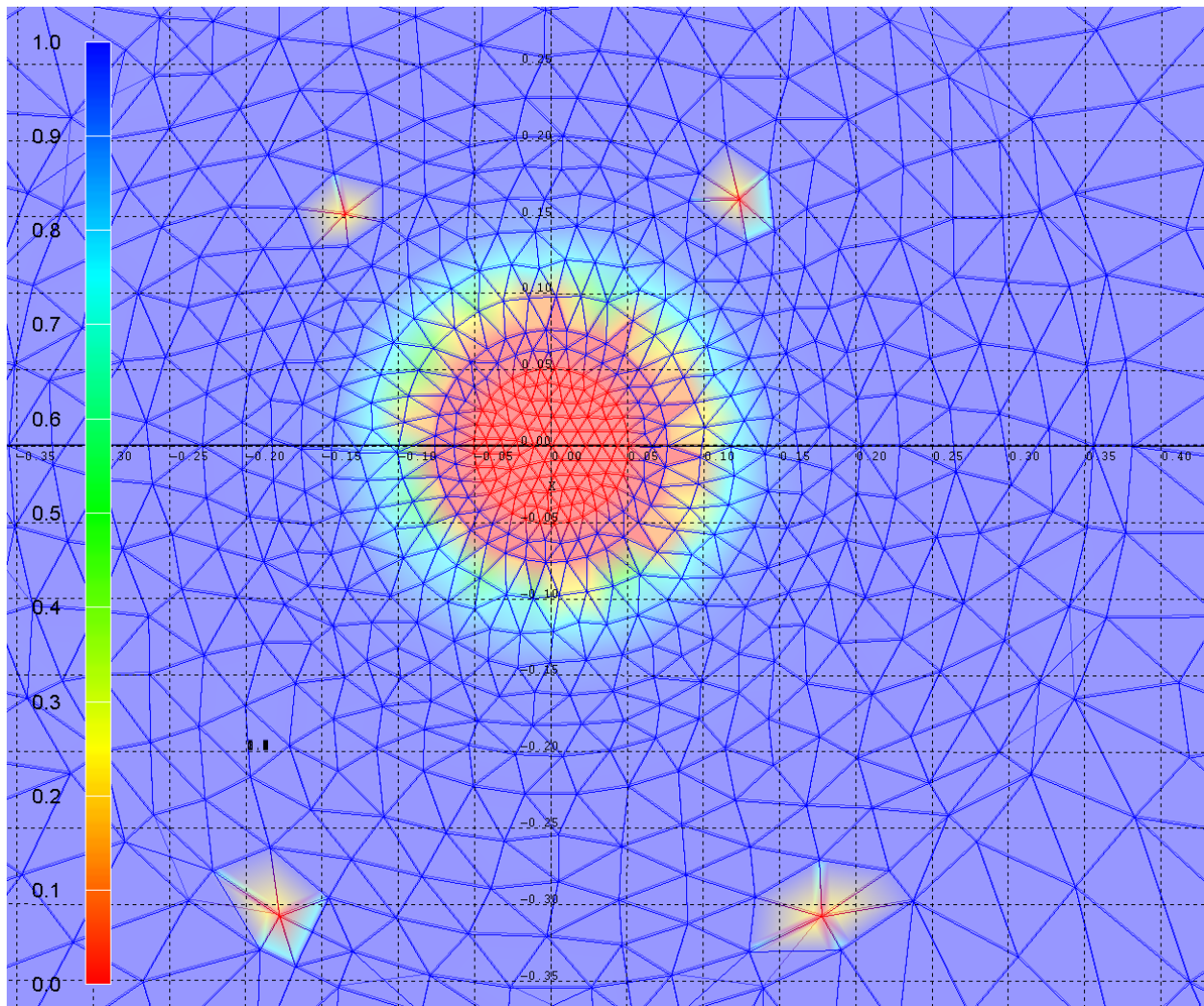
Figure 22: Saturation in the near field of the heater at 90 days with 500W. Observation holes can be seen as low saturation nodes in this slice.
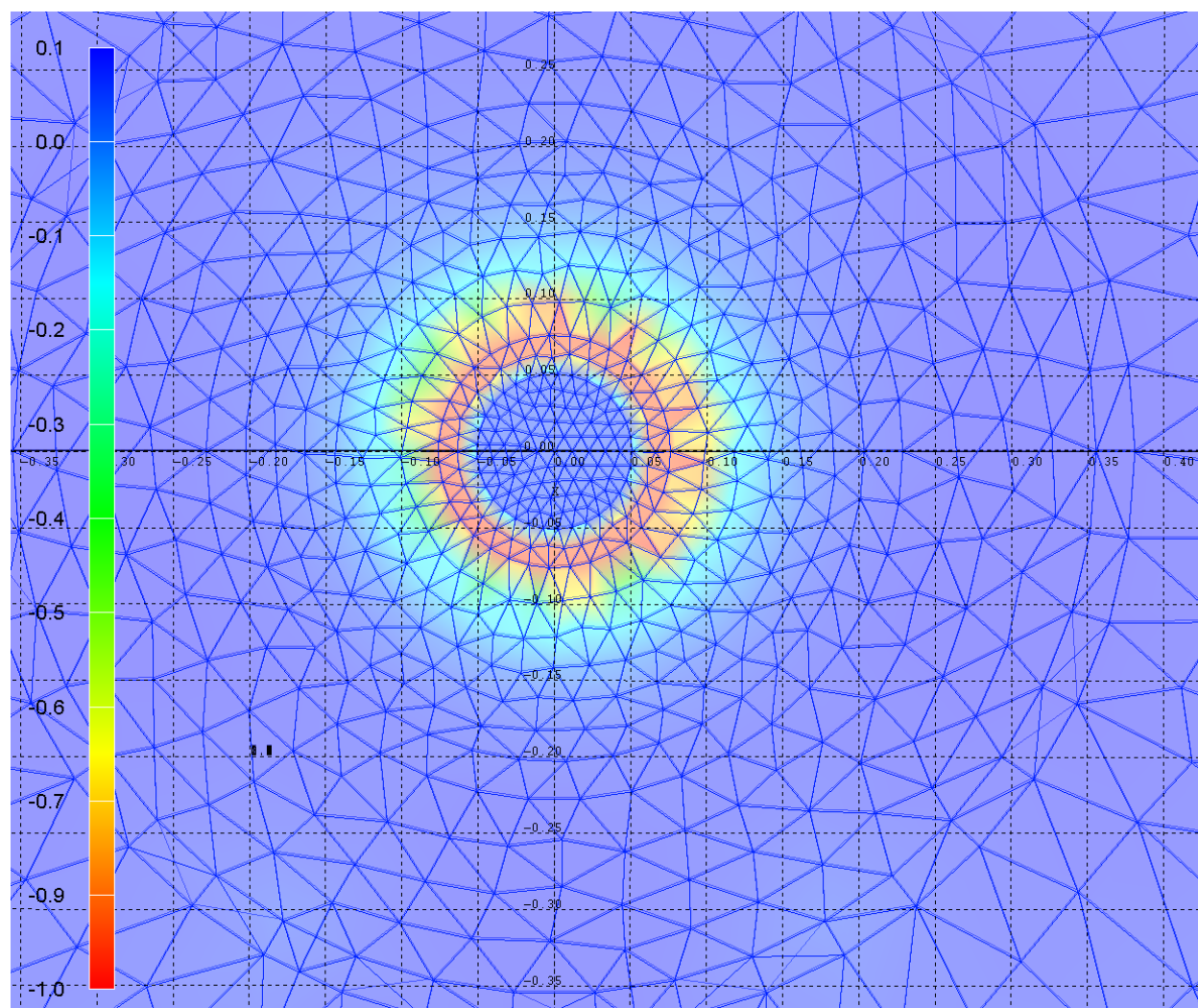
Figure 23: Water pressure in the near field of the heater at 90 days with 500 W.

8 Laboratory activities supporting a borehole heater test

8.1 WIPP brine composition

This section describes experiments proposed to support a new round of DOE-NE funded field testing in salt (See Section 7.1 for more details). Heating will likely impact brine composition and brine inflow into proposed heated boreholes. Knowledge of the brine composition and how it is impacted by heating is one of the goals of the small-diameter borehole heater test. The composition of the brine is useful for understanding brine mineral interactions that occur during heating, but more importantly, for its implications in the corrosion of waste packages, radionuclides transport, and safety considerations. Effectively, some components of the brine undergo important phase transformations that can result in significant volume changes and production of corrosive gases such as HCl. Historical records and reports from Sandia National Laboratory (Molecke, 1983) have documented the composition of different brines relevant to WIPP. The data in Table 7 summarize the ionic compositions for the major cations

Experiments and Modeling to Support Field Test Design

and anions of Brines A and B (also called WIPP Brines A and B), WIPP fluid inclusion Brines No. 1 and No. 2, and WIPP-12 (brine flow and downhole brine samples). More details on the origin and use of the different brines for testing can be found in the Sandia report (Molecke, 1983).

Table 7: Ionic compositions for the major cations and anions of selected brines relevant to the small-diameter borehole heater testing. Concentrations are expressed in mg/L.

Ions	WIPP Generic Brines A	WIPP fluid inclusion No. 1	WIPP fluid inclusion No. 2	WIPP Generic Brines B	WIPP-12 brine
Na^+	42,000	63,000	32,000	115,000	114,000
K^+	30,000	8,700	6,800	15	3,100
Mg^{2+}	35,000	23,000	40,000	10	1,700
Ca^{2+}	600	210	150	900	410
Sr^{2+}	5			15	15
Zn^{2+}					0.5
Li^+	20			20	220
Rb^+	20			20	
Cs^+	1			1	
Fe^{3+}	2			2	3.6
Cl^-	190,000	160,000	160,000	175,000	160,000
SO_4^{2-}	3,500	13,200	13,200	3,500	17,000
B as BO_3^{2-}	1,200			1,200	1,200
HCO_3^-	700			700	2,600
Br^-	400			400	430
I^-	10			10	
F^-					4.3
pH	6.5			6.5	7.17

In general, the brines can be classified in two classes based on their Mg-K-Na content. Brine A has a high potassium and magnesium content and is very close in composition to brines found in fluid inclusions. Brine A represents brines that percolate through formations containing potash. Brine B is very low in potassium and magnesium and is very close to saturation, and so represents brines that interacted with relatively pure halite.

The composition of the brine is important because of the reactivity of certain components of the bine at elevated temperatures. For example Mg reacts with silica and aluminosilicate components to yield hydrated Mg silicates (mineral name – talc) (Molecke et al., 1981).

$$3MgCl_2 + 4SiO_2 + 4H_2O \rightleftharpoons Mg_3Si_4O_{10}(OH)_2 + 6H^+ + 6Cl^- \qquad 1$$
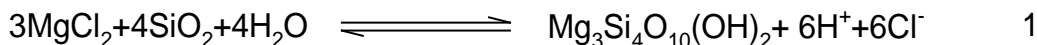
Reactions of magnesium chloride with silica leads to the decrease of pH as a result of the formation of HCl. Past studies from Sandia National Laboratory have reported low pH in some of the corrosion experiments performed in magnesium-rich brines at elevated temperature (Molecke et al., 1981). Some of the pH decreases can be attributed to the formation of the magnesium silicates. The dehydration of magnesium chloride can also lead to the formation of HCl at elevated temperatures. Reactions 2-8 summarize the series of reactions involved in the dehydration of magnesium chloride salts.

$$MgCl_2 \cdot 6H_2O_{(s)} \rightleftharpoons MgCl_2 \cdot 4H_2O_{(s)} + 2H_2O \qquad 2$$

$$MgCl_2 \cdot 4H_2O_{(s)} \rightleftharpoons MgCl_2 \cdot 2H_2O(s) + 2H_2O \qquad 3$$

$$MgCl_2 \cdot 2H_2O_{(s)} \rightleftharpoons MgCl_2 \cdot 2H_2O(s) + 2H_2O \qquad 4$$

$$MgCl_2 \cdot 2H_2O_{(s)} \rightleftharpoons MgCl_2 \cdot H_2O(s) + H_2O \qquad 5$$

or

$$MgCl_2 \cdot 2H_2O_{(s)} \rightleftharpoons MgOHCl_{(s)} + HCl_{(g)} + H_2O \qquad 6$$

$$MgCl_2 \cdot H_2O_{(s)} \rightleftharpoons MgCl_{2(s)} + H_2O \qquad 7$$

or

$$MgCl_2 \cdot H_2O_{(s)} \rightleftharpoons MgOHCl(s) + HCl_{(g)} \qquad 8$$
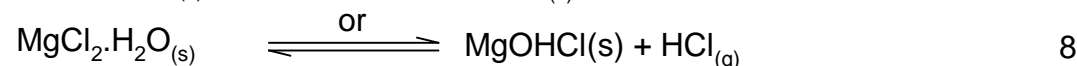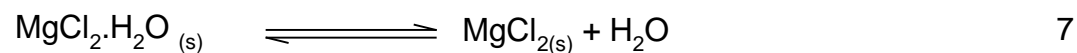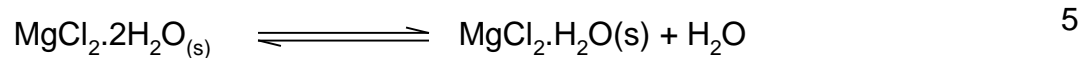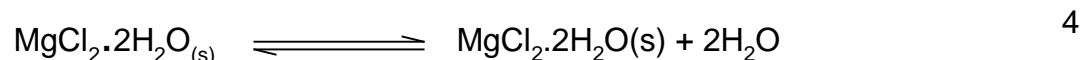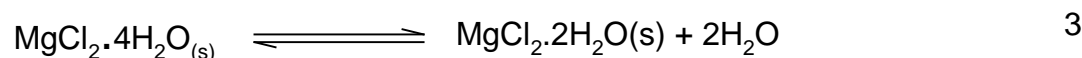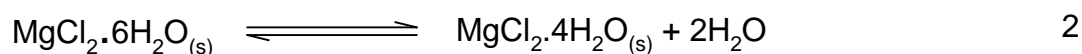
The production of HCl gas by the dehydration of $MgCl_2 2H_2O$ depends of the partial pressure of water and HCl. Historical records from Sandia National Laboratory have reported the production of HCl gas in some of the heater tests performed at WIPP (Krumhansl et al., 1991). Production of HCl can impact the waste corrosion rate, be detrimental to equipment, and, in sufficient quantities, can constitute a health hazard.

During a planning field visit to WIPP, samples of brine were collected from boreholes SNLCH111 and SNLCH114 in the SDI experimental area (Figure 24). The samples collected were analyzed by Mills, Melissa Marie at Sandia National Laboratory (Kuhlman et al., 2017). The composition of the brine is shown in Table 8.

Figure 24: Picture of boreholes used to collect brine samples for analysis. Boreholes are located at the SDI experimental area at WIPP.

These data show that brine samples accumulated in the SNLCH boreholes closely resemble the WIPP generic Brine A. Note the high sulfate content relative to any of the historical brines reported at WIPP. Magnesium and potassium concentrations are also elevated.

The composition of the brine is likely to change during heating experiments. It is expected that calcium and magnesium will react with sulfate to precipitate anhydrate or gypsum. Magnesium and calcium will also react with silica and aluminosilicate to form insoluble precipitate of Ca and Mg aluminosilicates. Brine composition will also change because of the inflow of brine from surrounding rock salt driven by the temperature gradient. The source of brine in the rock salt includes brine from fluid inclusions and intrusion from brine pockets. However, if the temperature is sufficiently high the brine will vaporize. Based on the initial composition of the migrating brine that will transport under saturated conditions, it is likely that during heating conditions the brine reaching the heating element will likely resemble the current brine and will be close to the generic Brine A.

Experiments and Modeling to Support Field Test Design

Table 8: Ionic compositions for major cations and anions of selected three brine samples collected from WIPP boreholes SNLCH114 and SNLCH111.

Ions	SNLCH114 (yellow)	SNLCH111 sample 1	SNLCH111 sample 2	SNLCH111 sample 2	WIPP Generic Brine A
Na^+	44,900	44,000	45,000	45,000	42,000
K^+	30,500	32,200	33,000	33,000	30,000
Mg^{2+}	49,600	52,300	53,700	53,700	35,000
Ca^{2+*}	10	10	10	10	600
Sr^{2+}					5
Zn^{2+}					
Li^+	40	40	40	40	20
Rb^+					20
Cs^+					1
Fe^{3+}					2
Cl^-	259,000	271,000	280,000	280,000	190,000
SO_4^{2-}	29,900	32,100	33,100	33,100	3,500
B as BO_3^{2-}					1,200
HCO_3^-					700
Br^-	2,900	3,100	3,200	3,200	400
I^-					10
F^-	20	20	20	20	
pH					6.5

*Measurements were uncertain for Ca. It is likely that calcium concentration is much higher.

8.2 Thermogravimetric analysis (TGA) of brine collected from boreholes from SNLCH111 and SNLCH114

Selection of heating parameters suitable for the small-scale borehole heater tests must consider the mineralogical composition of the rock salt at the location of the test, the composition of the brine, and how the different components of the rock salt and brine will react with temperature. To support this effort, we performed a limited number of experiments focused on identifying the transformations that occur in the brine as it is heated up to 250 ℃. The plots in Figure 25 show the thermogravimetric analysis of filtered and unfiltered brine samples collected from borehole SNLCH111.

Experiments and Modeling to Support Field Test Design
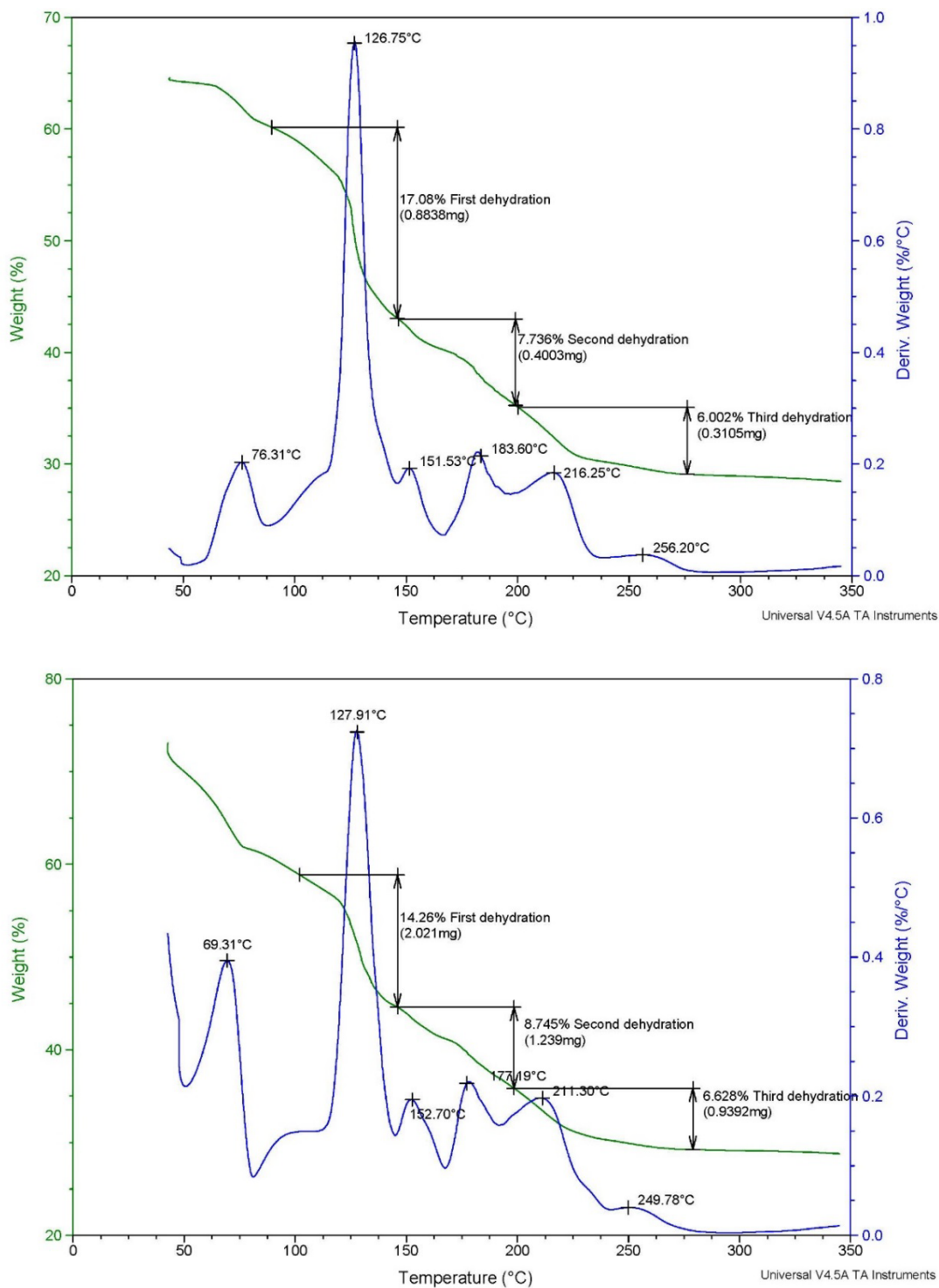
Figure 25: Dehydration measurements of filtered (top) and unfiltered (bottom) WIPP brine collected from borehole SNLCH111. The brine samples were equilibrated at 45°C and heated to a final temperature of 350°C at a rate of 10°C/minute under nitrogen atmosphere.

Dehydration profiles of the filtered and unfiltered brine are similar (Figure 25). The analysis shows that the brine dehydration starts at ambient temperature and accelerates with temperature to about 100 °C. Some distinct transformation events can be identified, but in general the behavior shows a continuous loss of water with increased temperature. This behavior is expected for the dehydration of salt mixtures. This behavior is also expected for the dehydration of magnesium salts which are known to have a very complex dehydration profiles (Figure 26; Chipera and Vaniman, 2006).
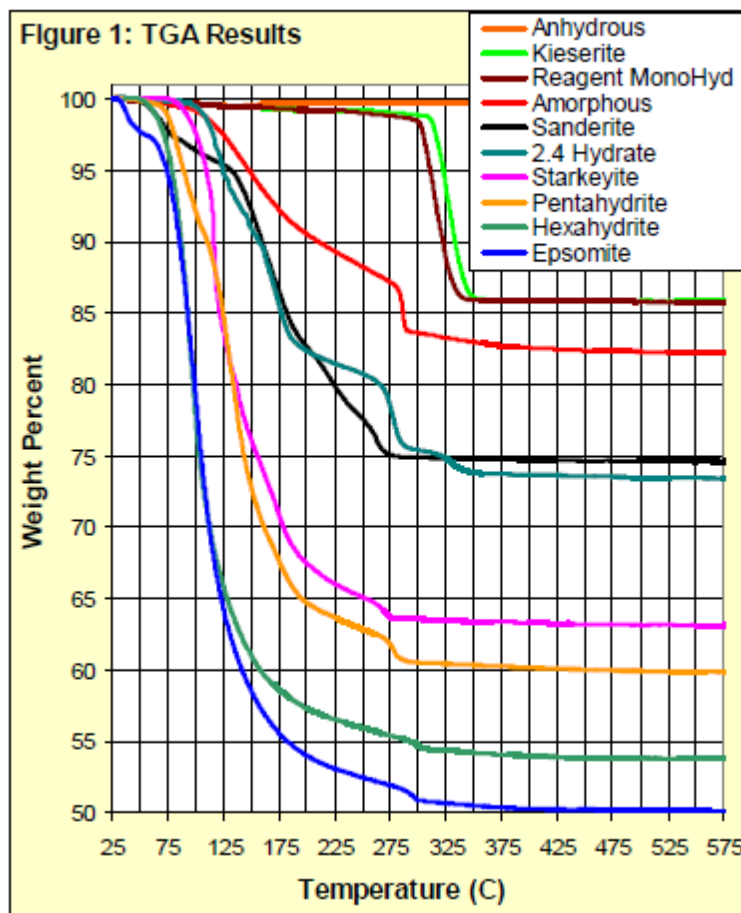
Figure 26: TGA analysis of various MgSO4 hydrates plotted as sample weight vs. temperature upon heating. Figure from Chipera and Vaniman (2006).

The initial weight loss of approximately 30% is attributed to the evaporation of the brine water. The first visible transformation event between 60 °C and 90 °C is tentatively assigned to the dehydration of magnesium chloride according to reactions 2 (Figure 27). The second transformation is a major endothermic event that occurs between 110 °C and 140 °C and results in a loss of 14 to 17 wt.%. As can be seen from the TGA plot at about 150 °C a total mass loss of about 60 wt.% occurs. This mass loss is attributed to the transformation of magnesium chloride through reactions 2 to 7 and the gradual dehydration of magnesium sulfate through reaction 9.

Experiments and Modeling to Support Field Test Design

$$MgSO_4.nH_2O_{(s)} \rightleftharpoons MgSO_4.(n-1)H_2O(s) + H_2O_{(g)} \qquad 9$$

The dehydration and transformation events occurring at temperatures higher than 150 °C are also attributed to the transformation of magnesium chloride through reaction 5 -8. This is also the same temperature domain in which magnesium sulfate loses its remaining water to form magnesium sulfate anhydrate.
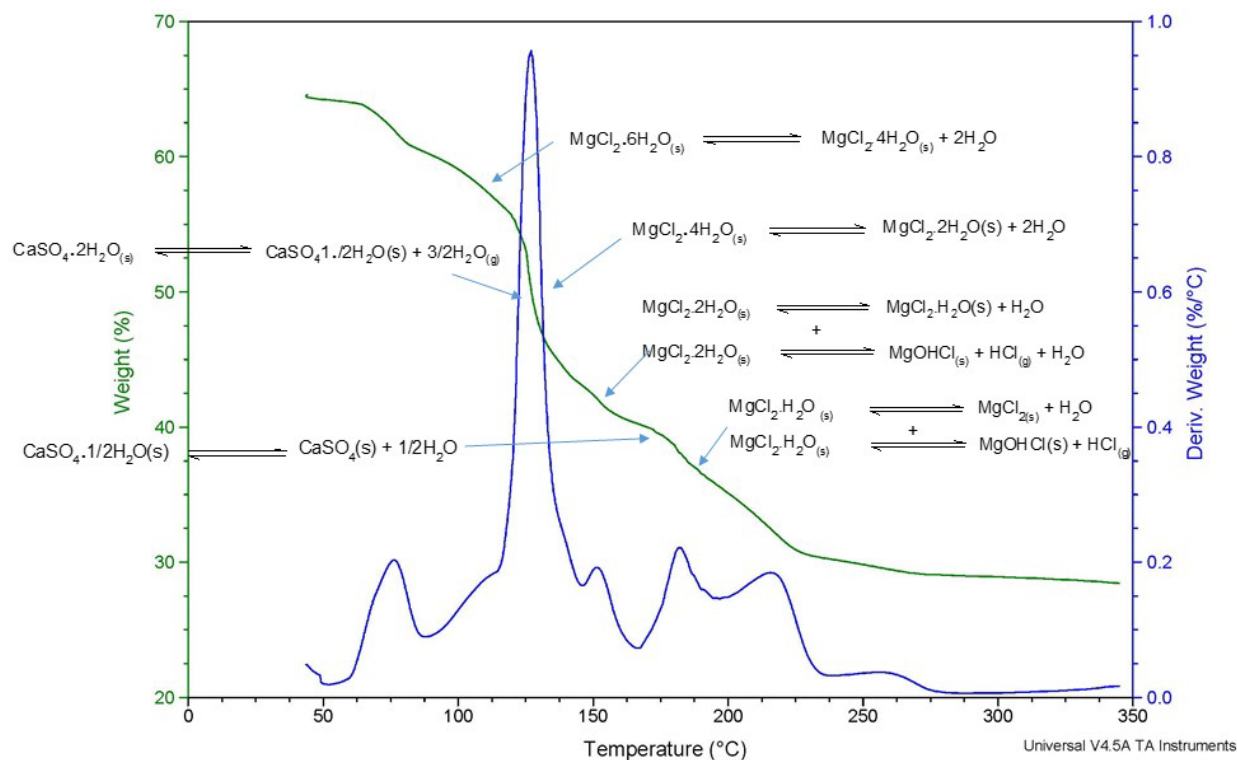
Figure 27: Chemical reactions assigned to the events observed in the plot of mass loss as a function of temperature and the first derivative of the same plot for WIPP brine collected from borehole SNLCH111.

Note that dehydration of $MgCl_2.2H_2O$ per reaction 5 and its irreversible transformation to MgOHCl occur in the same temperature domain between 150-210 °C. Both dehydration reactions are endothermic and produce water. However, the decomposition reaction 6 produces HCl gas. The ratios of transformation of $MgCl_2.2H_2O$ per reactions 5 and 6 is dependent on the reaction conditions including the relative concentration of water and HCl gas. Under our experimental conditions the samples were constantly exposed to dry nitrogen stream which could favor reaction 5 over decomposition reaction 6. In a more confined environment with conditions of high saturation, reaction 6 might be more favorable, but in dry environments reaction 5 might be more important. The two competing reactions 7 and 8 can also lead to the formation of MgOHCl or the anhydrous magnesium chloride. The ratio of each reaction will be determined by

the experimental conditions including temperature and relative humidity and might be strongly dependent on the confinement of the reaction.

The presence of gypsum was not confirmed by the brine analysis. However, calcium measurements are unreliable because of an interference from magnesium in the IC system. It is likely that gypsum is present and is contributing to the observed weight loss as a function of temperature. Gypsum dehydration can be caused by two dehydration events described by the reactions 10 and 11.

$$CaSO_4 \cdot 2H_2O(s) \rightleftharpoons CaSO_4 \cdot 1/2H_2O(s) + 3/2H_2O_{(g)} \qquad 10$$

$$CaSO_4 \cdot 1/2H_2O(s) \rightleftharpoons CaSO_4(s) + 1/2H_2O \qquad 11$$
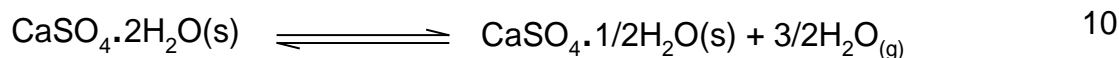
The first dehydration occurs between 100-170 ºC and therefore would contribute to the second major endothermic event. The second dehydration that results in the loss of the remaining water occurs between 100-180 °C (Yu and Brouwers, 2012).

In general these preliminary data point to a complex dehydration and transformation processes which occur in the temperature domain between 45 ºC and 250 ºC. These mineral transformations result in a weight loss of about 70 wt. %. Some of the transformations could lead to the production of HCl gas. However, this will depend on the temperature and relative humidity and reactivity of HCl gas produced. At temperatures below 150 ºC, the dehydration of magnesium chloride is not expected to progress to reactions 5, 6, 7 and 8 and therefore HCl generation can be controlled by operating under temperatures below this threshold.

8.3 Heater assembly design

The small-scale borehole heater test developed in the consensus document (Kuhlman et al., 2017) proposes the use of an electrically powered heater placed in a central borehole with satellite observation boreholes arranged at multiple distances from the central bore hole. The desired maximum borehole wall temperatures are 50°C, 120°C, 160°C, and 200°C. The details of the heater construction and emplacement in the borehole were discussed in the consensus document (Kuhlman et al., 2017) including the emplacement of the heater in the borehole, backfilling the space, and construction of brine sampling devices. Designs of the appropriate packer system and sampling devices for gases and liquids were also discussed. To gain practical insights on the heater construction, deployment, and sampling devices, we designed and constructed a heater and liquid gas sampling devices in support of the proposed heater test. These setups were designed to perform a scoping heating experiment to test sampling and measurement equipment. In the following section, we summarize the equipment built and show preliminary results from laboratory testing.

Experiments and Modeling to Support Field Test Design

8.3.1 Heater specifications

A block heater was constructed from a stainless steel cylinder and a heater cartridge (Figure 28).
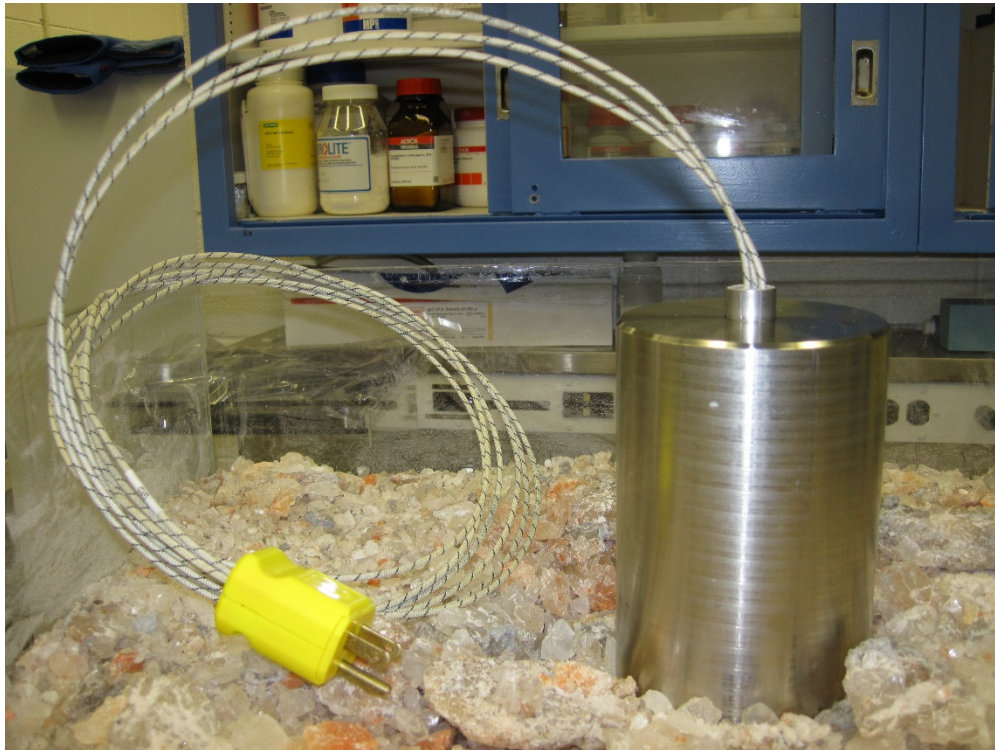
Figure 28: Photograph of a block heater constructed by inserting a cartridge heater in stainless steel cylinder.

The cartridge heater was from Walton and the specifications are as follows:

Diameter [in] (B) .746" +/- .002"
Overall Length [in] (A) 5.500
Length Tolerance + /- 2%
Voltage [V] 120
Power [W] 1,000
Wattage Tolerance [%] + 5%,- 10%
Terminations LA Options
End Seal No Seal
Lead Type Fiberglass (GGS)
Lead Length [in] (E) 76
LA Style Option E = Swaged In Leads
Ground Lead Length [in] (E) 74
Sheath Materials Incoloy 800
Lead End No Heat [in] 'NOM' (D) 0.500
Disk End No Heat [in] 'NOM' (C) 0.25

Watt Density [w/in2] nom 87

The stainless steel cylinder specifications are as follows:
Heater block material: stainless steel 360
Length [in] 6"
Diameter [in] 4.5"
Heater cartridge insert housing diameter .8"
Heater cartridge insert housing depth 5"

Experiments and Modeling to Support Field Test Design
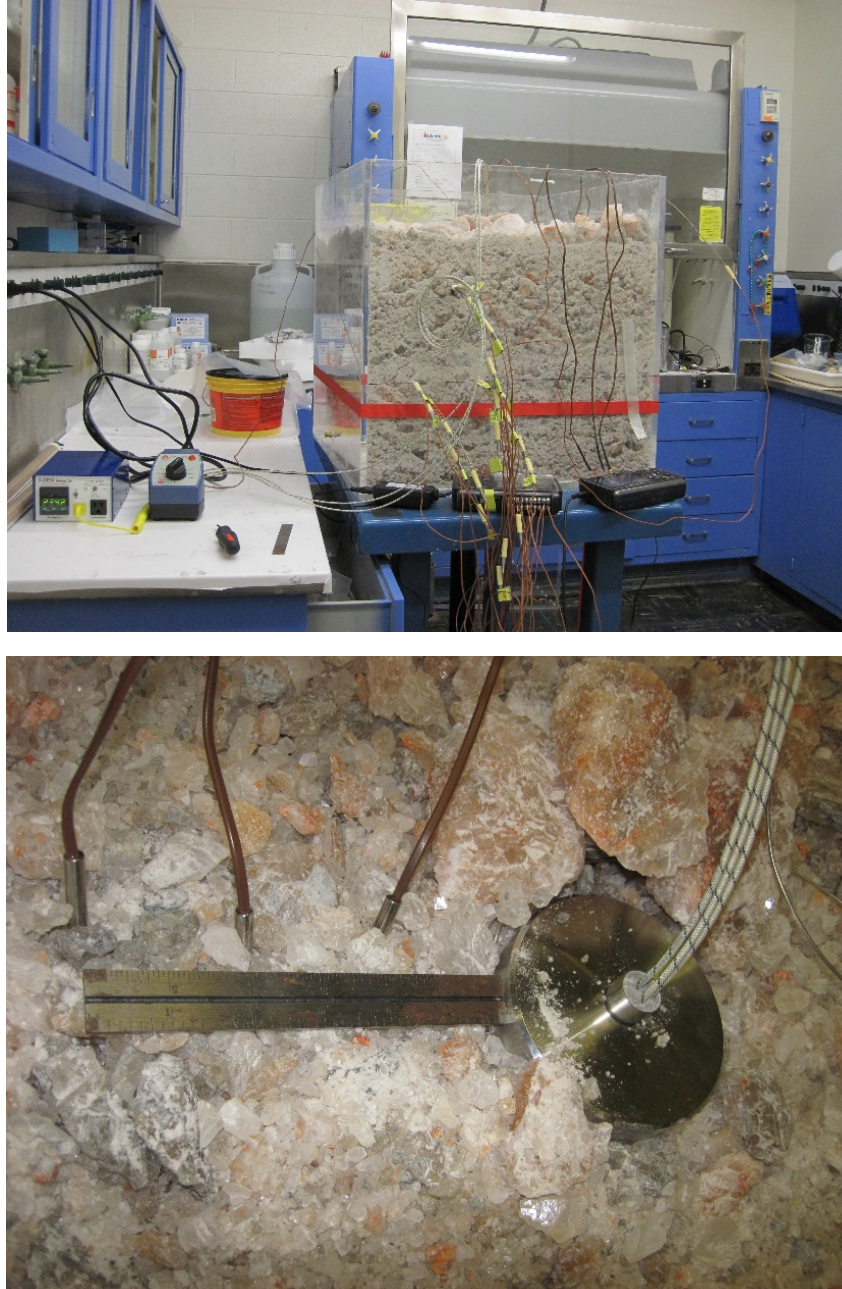
Figure 29: Photograph showing a salt box filled with ROM salt and equipped with a heater, temperature controller, and thermocouples used to test the heater assembly (top), and photograph of the heater assembly with thermocouples placed at increasing distances from the heater (bottom)

A heating test was performed with the heater assembly in a box filled with Run-of-Mine salt (Figure 30). The testing was performed to test the ability of the heater assembly to heat up salt homogeneously for an extended time.
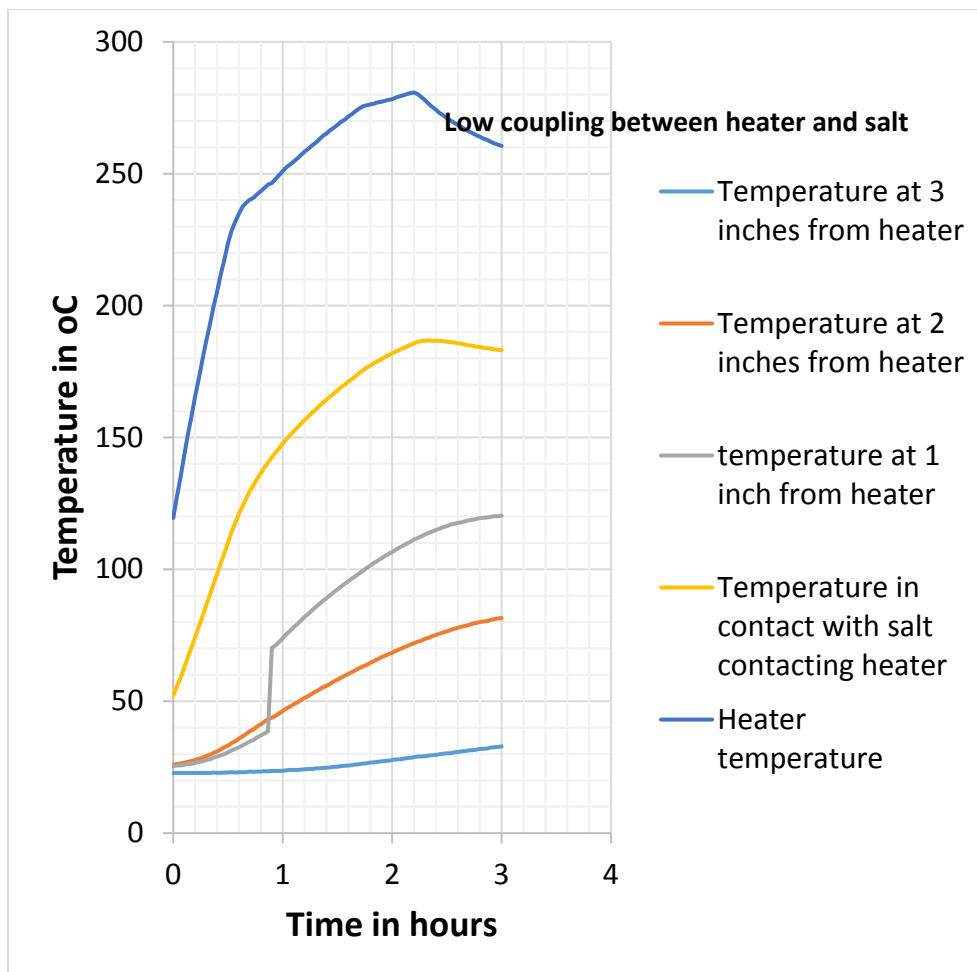
Figure 30: Data showing temperature of the surface of the heating assembly and temperatures recorded in the crushed salt in contact with the heater and at incremental distances of 1, 2, and 3 inches from the heater.

The heater assembly was effective at heating salt very quickly and the temperature regulator was effective at maintaining the temperature of the heater assembly to the target temperature. However, the data show a low coupling between the heating block and salt, which results in up to 100 °C difference between the temperature at the surface of the heater and the salt contacting the heater. This low coupling between the salt and the heater is likely to be an important parameter to consider for the borehole heated test design. Reaching the target maximum temperatures of 50°C, 120°C, 160°C, and 200°C might require adjusting the heater assembly to tens of degrees higher than the target maximum temperatures.

8.3.2 Underground heater test design for equipment testing

A simple borehole test was designed to test the heater and sampling equipment. The design took advantage of existing boreholes that are already drilled in the SDI experimental area. The properties of the boreholes shown in Figure 24 above are summarized in Table 9.

Experiments and Modeling to Support Field Test Design

Table 9: Summary of boreholes available for heater testing.

Borehole id	Approximate diameter, Centimeters	Approximate depth, meters	Approximate distance between boreholes in cm	Comments
SNLCH111	12	4.4		Large amount of pooled brine at end of borehole
SNLCH112	12	3.96	48.76 cm between SNLCH112 and SNLCH111	Large amount of pooled brine at end of borehole
SNLCH113	12	19.8	32 cm between SNLCH113 and SNLCH112	Large amount of pooled brine at end of borehole
SNLCH114	12	6	30 cm between SNLCH114 and SNLCH113	Large amount of pooled brine at end of borehole
no id/ little borehole	3.35	3.96	23 cm between SNLCH112 and small borehole	Large amount of pooled brine at end of borehole

We propose to insert the heating assembly in borehole SNLCH 13. A simple packer assembly will be used to isolate the atmosphere of the borehole from the outside and a collection of Teflon tubing will be inserted in the heated borehole to allow sampling of the gas and liquid brine pooled in the back of the borehole. To test the transport of tracers and ability to collect viable samples, borehole SNCH 14 will be used to introduce a D_2O tracer. All existing boreholes will be equipped with thermocouples to monitor temperature. Brine migration will be qualitatively monitored by monitoring brine availability in all available boreholes. A matrix summary of the suggested heating and monitoring parameters is summarized in Table 10.

Experiments and Modeling to Support Field Test Design

Table 10: Borehole heater test components

Heating conditions	Duration	Measured parameters	When	Follow-up Lab analysis	Schedule
Ambient	24 hours	Temperature of rock salt	Continuous		Start date: July 10th-14th
		Brine samples	Initial	Brine Composition	
		Air samples	Initial before heating	Tracers in air samples	
50 °C	24 hours	Temperature	Continuous		Start date : July 10th-16th
		Brine samples	After heating	Brine Composition	
100 °C	1 week	Temperature of rock salt in test borehole and surrounding boreholes	Continuous	Temperature profiles simulations	July 10th-17th
		Brine samples	After heater removal	Brine Composition	
		Efflorescence	After heater removal	Composition	
		Air samples	daily daily		

Execution of the test did not proceed beyond the initial scoping effort.

9 Simulations supporting an in-drift experiment

Several experimental designs have been proposed over the past few years for larger scale, in-drift emplacement of non-radioactive heaters (see Stauffer et al., 2015, section 3 and Bourret et al., 2016, section 7). A proposed plan to have up to five canisters has been delayed, but a scaled down version of a single heated canister covered in ROM salt has recently (late August, 2017) been installed at WIPP through DOE-EM funding. We are leveraging this experiment to learn how modern data loggers, thermocouples, and other instrumentation behave in the underground salt environment. Further, the data from the DOE-EM experiment provide a good benchmarking exercise for our conceptual and numerical models of post emplacement processes. Modeling in support of this effort has been undertaken to establish expected results from the experiments. The design and emplacement of the canister and full model domain are in shown in Appendix C.

9.1 Purpose

The active experiment has installed a canister which will produce a constant output of 1500 watts for one year. Conceptually, the experiment is a scaled up variant of brine/vapor/porosity interactions described elsewhere in this report. Additional processes occur within the pile when scaled up in this manner compared to the Olivella et al. (2011) work; for example, heat transfer in a larger pile within an open gallery becomes more complicated due to the development of a convective chimney. Brine may also be available from the drift wall and floor as well as humidity from the surrounding gallery air. It is hypothesized that the pile around the canister will dry and experience deposition of salt, causing pore closure and the formation of a low-porosity, low-permeability "rind" of salt encasing the canister. Moisture evaporated near the canister is expected to condense farther away from the canister where the pile is cooler, causing an increase in porosity and permeability in these areas. Although this broad concept is reasonable in the context of the known physics, specifics of rind thickness, maximum temperature, and maximum porosity are unclear. Behavior of the experiments will allow us to constrain numerical modeling and aims to reduce uncertainty in predictions related to the safety basis.

The current experiments will also provide an opportunity to validate new model functions against a large scale physical test. Although FEHM has been applied successfully to numerous situations, many new capabilities have been developed for salt work. Validation has occurred in some areas (Stauffer et al., 2015; Jordan et al., 2015a,b,c; Bourret et al. 2016; Bourret et al., 2017), but additional large scale, carefully controlled experiments provide an excellent opportunity to further test these functions and build confidence in the new salt functions.

9.2 Model domain and parameters

A thin (0.2 m) mesh (nominally 2-D) and full three-dimensional mesh have both been developed for this problem. However, it should be noted that the three-dimensional mesh takes

much longer (many days to over a week for a single run) than the 2-D mesh (a few hours). Consequently, current efforts have used the thin slice mesh. Full three-dimensional modeling will be employed after optimization of the 2-D mesh is complete. The total model domain for the 2-D mesh is shown in Appendix C. Overall dimensions of the domain are 18.7 m width (x direction), 0.2 m depth (y direction), and 36.6 m height (z direction). The canister (Figure 31, orange) is placed centered at the origin, with a radius of 0.6 m (2 feet). The canister is mostly surrounded by a zone (yellow) defined with ROM salt properties (Table 11), but the very bottom of the canister is placed on the floor of the gallery. Above and in the positive-x direction of the pile is open air (blue), which extends in the positive-x direction to the edge of the domain. The top, bottom, and left sides of the domain are restricted by dense, very low permeability intact salt (effectively bedrock (brown)). Since the gallery is carved into salt and places atmospheric pressure air against deep salt, decompression unloading occurs in the wall rock which causes the salt at the edges of the air to be damaged (grey). This damage is expressed as an order of magnitude increase in porosity and an increase in permeability. The left side of the salt pile is abutted against the wall to facilitate movement of personnel through the remainder of the drift. Properties for each unit are shown in Table 11.

Table 11: Rock properties for each salt unit

Property	ROM salt	Damage zone salt	Rock salt
Porosity (-)	0.35	0.01	0.001
Permeability (m^2)	10^{-12}	10^{-17}	10^{-20}
Density* (kg/m^3)	2165.0	2165.0	2165.0
Thermal conductivity (W/mK)	1.5	4.0	5.5
Initial saturation	**	1.0	1.0
Initial temperature	29.38	29.38	29.38

*Note that density is specified for the solid matrix and is modified within the model by porosity.

**ROM salt saturation is a parameter of interest and varies between runs
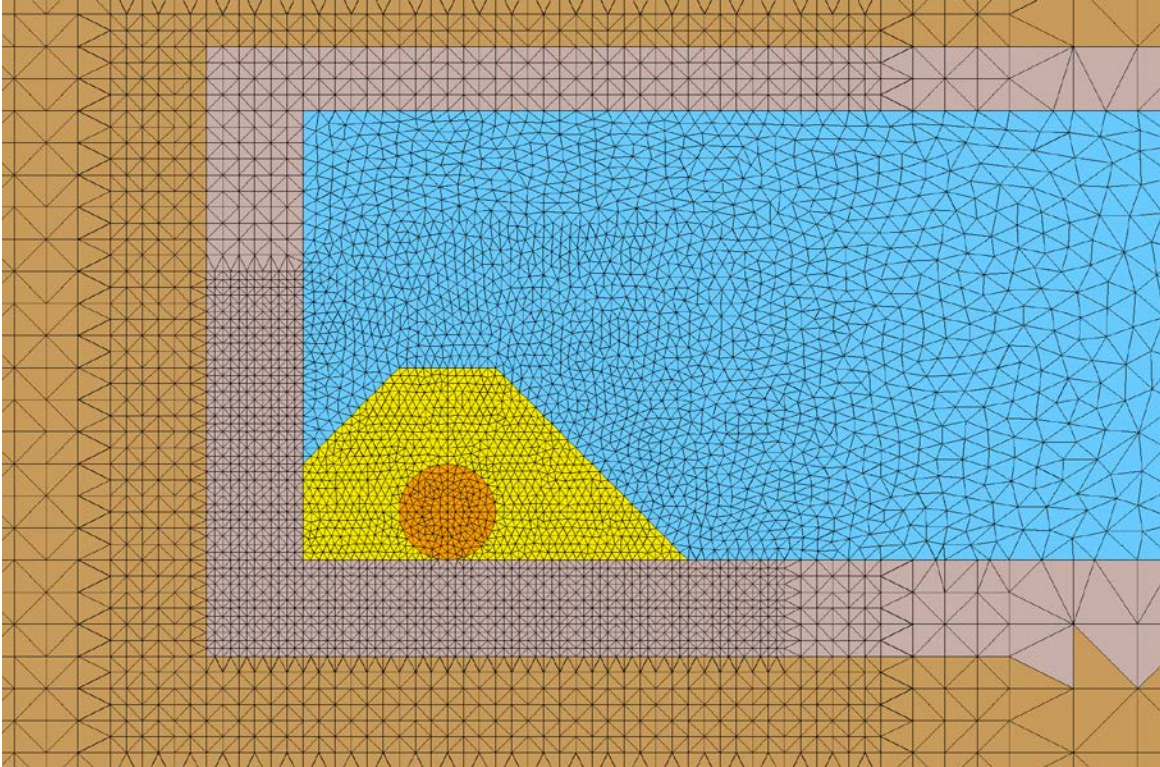
Figure 31: Model domain in the vicinity of the canister (orange). ROM salt is piled next to and on top of the canister (yellow), in an open air gallery (blue). Dense rock salt surrounds the gallery (brown). Due to decompression unloading and the process of carving the gallery, a damaged zone (grey) extends into the wall rock a short distance from the open gallery.

9.3 Approach

Brine and vapor migration resulting from heat transfer are two primary processes of interest in this experiment. Energy characteristics are established for the canister and unknown but constrainable in the air surrounding the pile. Consequently, the main parameters of interest for modeling work pertain to the drying of the pile, which relates to moisture content at the start of the model run and the ability of water or vapor to enter or exit the pile. Permeability of the pile is broadly known, but the moisture characteristics are less certain. There is uncertainty in the initial saturation of the pile and high uncertainty in the capillary pressure/saturation function for ROM salt. Consequently, simulations were conducted for initial pile saturations of 10^{-3}, 10^{-2}, 0.1, and 0.3. Expected pile saturation is towards the low end of these values, but this approach allows examination of a range of pile behaviors. Each set of simulations has two background runs conducted prior to the final setup. In the first background run, temperatures were held constant and permeability was set exceedingly low (10^{-22} m^2). This ensures that all nodes are populated with material parameters, proper initial saturation and temperature conditions, and there are no holes or other unexpected phenomena in the model. Following this, a second background is run for 7200 days (representing 20 years of the drift being open) with a constant uniform temperature of 29.38°C, the average temperature of a year-long set of collected data for WIPP (Bourret et al., 2017). Finally, a run is conducted with heat turned on and the pile permeability set to reasonable values for a pile of crushed salt. For the simulations presented

here, we do not include any contribution of water from hydrous mineral dehydration, another important source of uncertainty in the salt/water mass balance (Jordan et al., 2015).

A set of simulations is conducted first to establish a basic control setup and examine the general overall behavior of the pile, wall rock, and canister in order to target further exploration. Sensitivity to two initial parameters was conducted: first, the initial saturation, and second, the capillary model used. As there was little effect on the wall rock under any modeled conditions, altered parameters described hereafter apply to the pile of ROM salt. Initial pile saturation values of 10^{-3}, 10^{-2}, 10^{-1}, and 0.3 were used. For each of these three values, three linear relative permeability models were applied which were identical except for the residual saturation value. Three values of 0.05, 0.1, and 0.3 were applied for the residual saturation to test sensitivity to this parameter for each condition. However, the runs with the highest residual saturation values did not run to completion for initial saturations above 0.01. All of these runs used a maximum capillary pressure of 1 MPa. The true maximum value for ROM salt at WIPP has not been determined. As a final alternative possibility, the same initial and residual saturation sets were run but with much lower capillary suction pressures. All of the model runs described herein use the old linear formulation of capillary pressure; optimization of the model for complete 365 day runs using the new function (with retention as a function of porosity) is ongoing and will be presented in a subsequent milestone.

9.4 Results

9.4.1 Saturation

For the suite of model runs with low maximum capillary suction pressure, the pile rapidly desaturates for all runs (Figure 32). The walls of the gallery remain generally saturated and little overall effect is observed on the pile. If capillary suction within the pile is low, or there is little coupling between the pile and the floor such that water cannot be drawn out of the floor, then moisture of the experimental pile should rapidly approach zero.
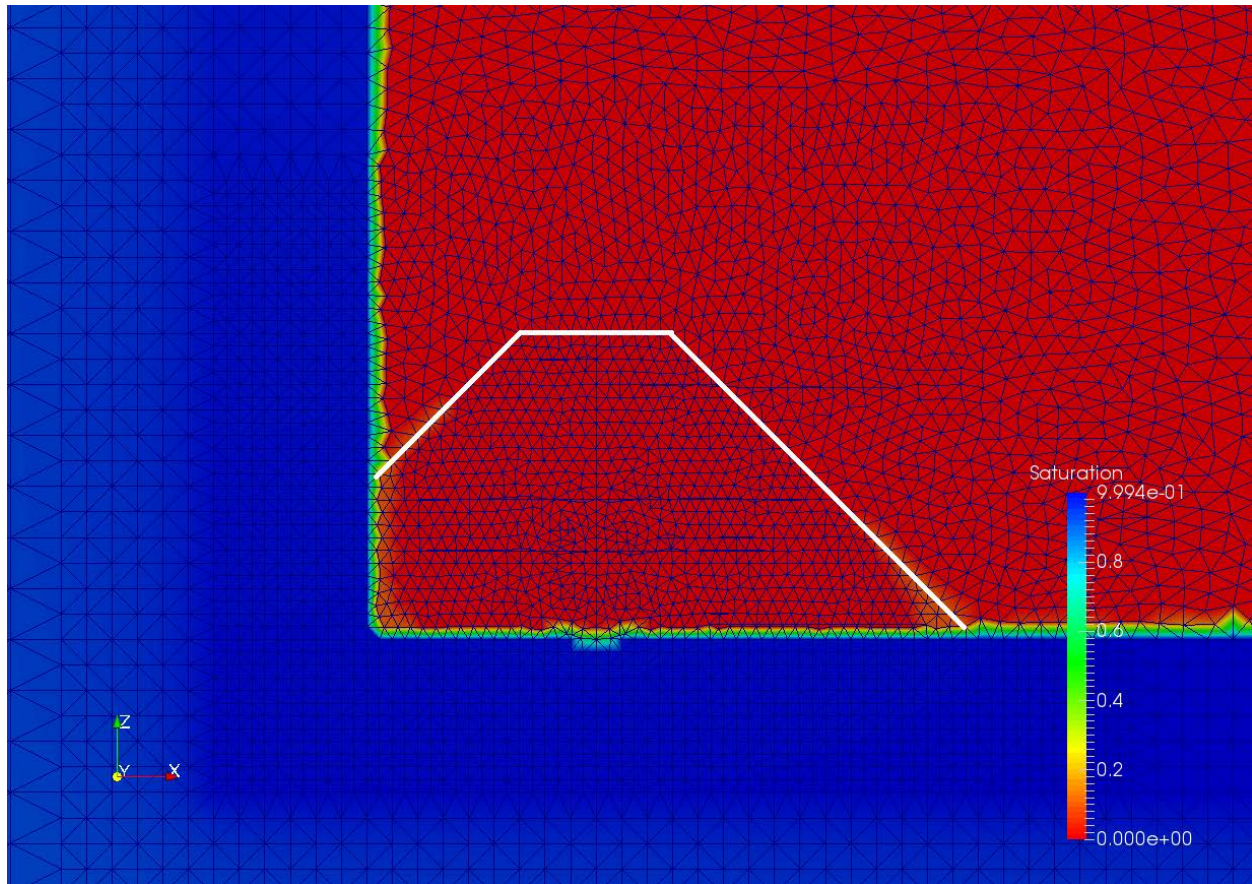
Figure 32: 365-day saturation results with a low capillary suction pressure. Red color indicates low saturation. Pile margins outlined in white.

For higher capillary suction effects, two general types of output result. When initial saturation is high or with low saturation but high residual saturation, water is retained through much of the pile (Figure 33) with saturations typically around the residual saturation value. The damaged zone surrounding the gallery shows partial drainage into the pile and the gallery, with much of the water below the pile being drawn upward by capillary effects to replace displaced water. These "wet" piles exhibit specific temperature and porosity characteristics that arise from the relatively high continuous saturation. The high saturation values are a product of the single specification of capillary pressure and single residual saturation at the beginning of the simulation when using the unmodified original capillary model (See Section 2). High initial residual saturations induce continuous high capillary suction pressures throughout the model run even in nodes where porosity is increasing, preventing drying of nodes.
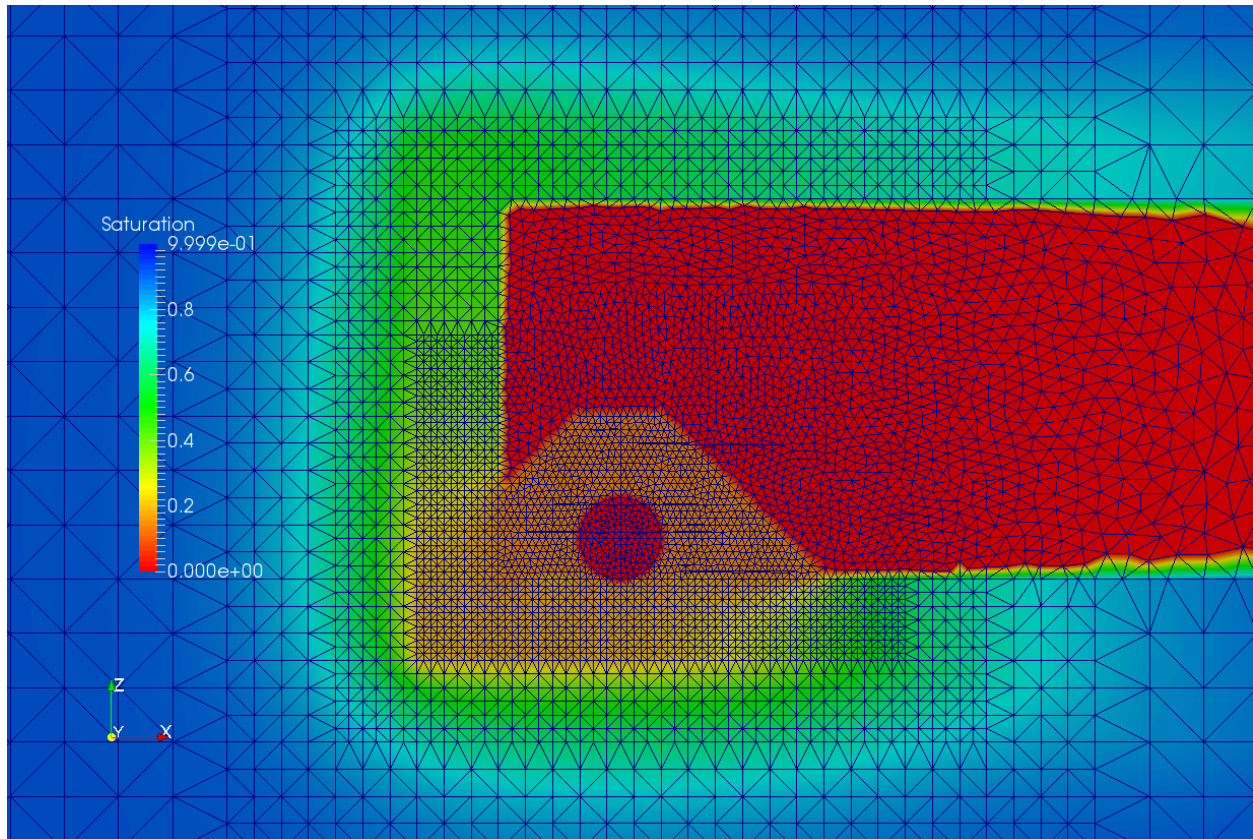
Figure 33: Pile saturation with high capillary pressure and high residual saturation after 365 days. This model has a residual saturation of 0.1, comparable to saturation of all salt pile nodes shown. Despite high canister temperature, the pile does not dry.

The second dominant mode is for the pile to dry out with progressive desiccation of nodes extending away from the canister (Figure 34). Overall saturation of the pile decreases considerably, and decreases are also seen in the damaged zone below and adjacent to the pile. This mode occurs when initial saturation is low if the residual saturation is not high. Overall capillary pressures are consequently lower until saturation has decreased considerably, by which point heat transfer has slowed enough to continue evaporating water. As a result, a desaturation front spreads upward and outward from the canister. As with the previous model set, the damaged wall rock partially desaturates in this case as well as capillary suction draws water from these nodes into the pile. These results represent a likely-case scenario for saturation if capillary suction in WIPP ROM salt is strong and moisture is available.

Experiments and Modeling to Support Field Test Design
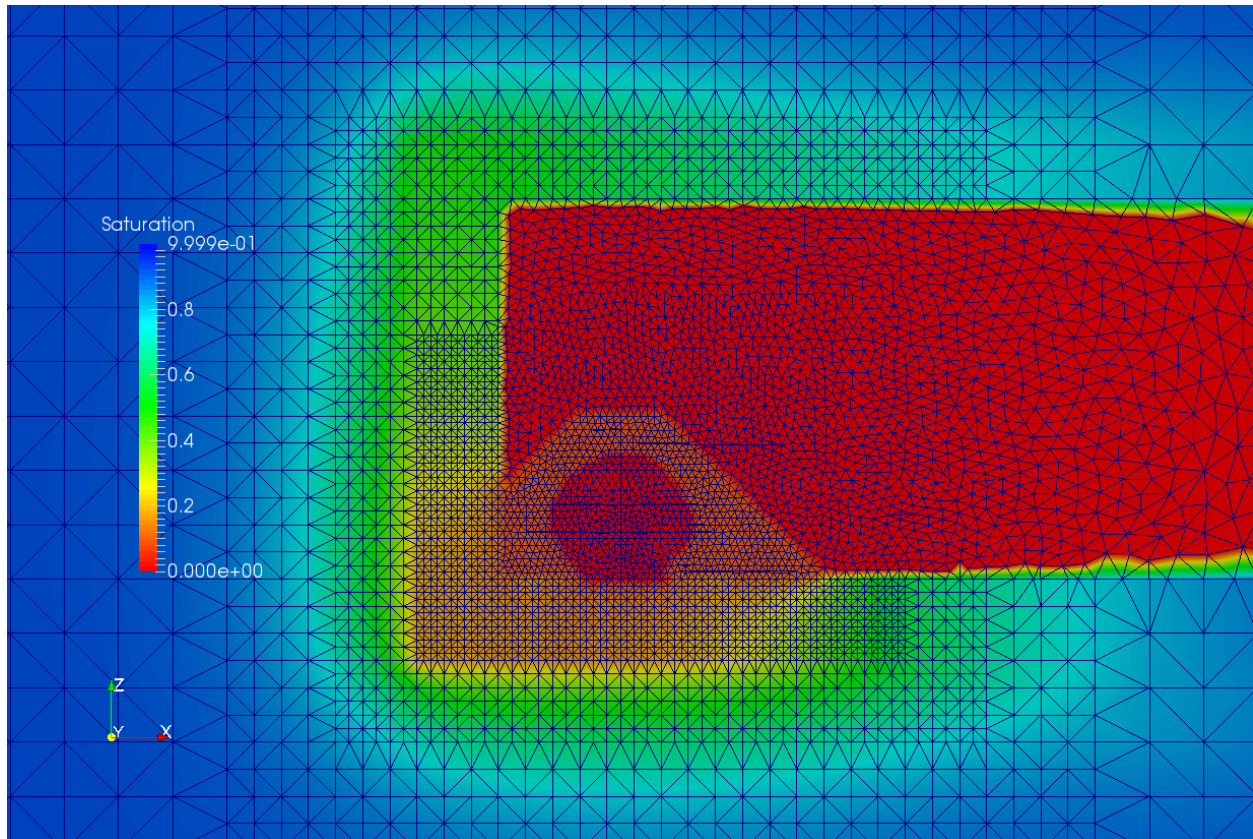
Figure 34: Pile with high maximum capillary pressure but low residual saturation. Capillary pressure near the canister is insufficient to keep nodes wet, allowing drying of pile near canister.

9.4.2 Temperature

Temperature profiles are similar qualitatively in all runs, but the actual temperature varies depending greatly on moisture content of the pile. Higher temperatures generally occur in piles that experience drying; the equal energy inputs into each model indicate that moisture retention affects temperature results, rather than the pile otherwise attaining higher temperatures for unrelated reasons and driving the water out. Evaporation of water consumes heat, especially when it condenses elsewhere within the pile and is recycled. This effect is further enhanced when capillary suction pressure is high and draws additional water into the pile. Escaping water vapor carries further heat away from the pile, but this effect relies on the presence of additional water entering the pile to continue. If water escapes the pile then this heat sink and enhanced heat transfer is negated and heat moves only through conduction and relatively inefficient convection in dry air.

When maximum capillary pressure is low and the pile dries rapidly, maximum temperature is high throughout the pile, with a peak value of 211.6°C in the canister (Figure 35). The surface of the pile reaches more than 70°C in portions. Air above the canister is relatively cool, with temperatures around 50-60°C. The rounded temperature pattern within the pile

indicates dominantly conductive heat transfer; the relatively conductive floor dissipates heat rapidly so that a wider area heats to a lower temperature.
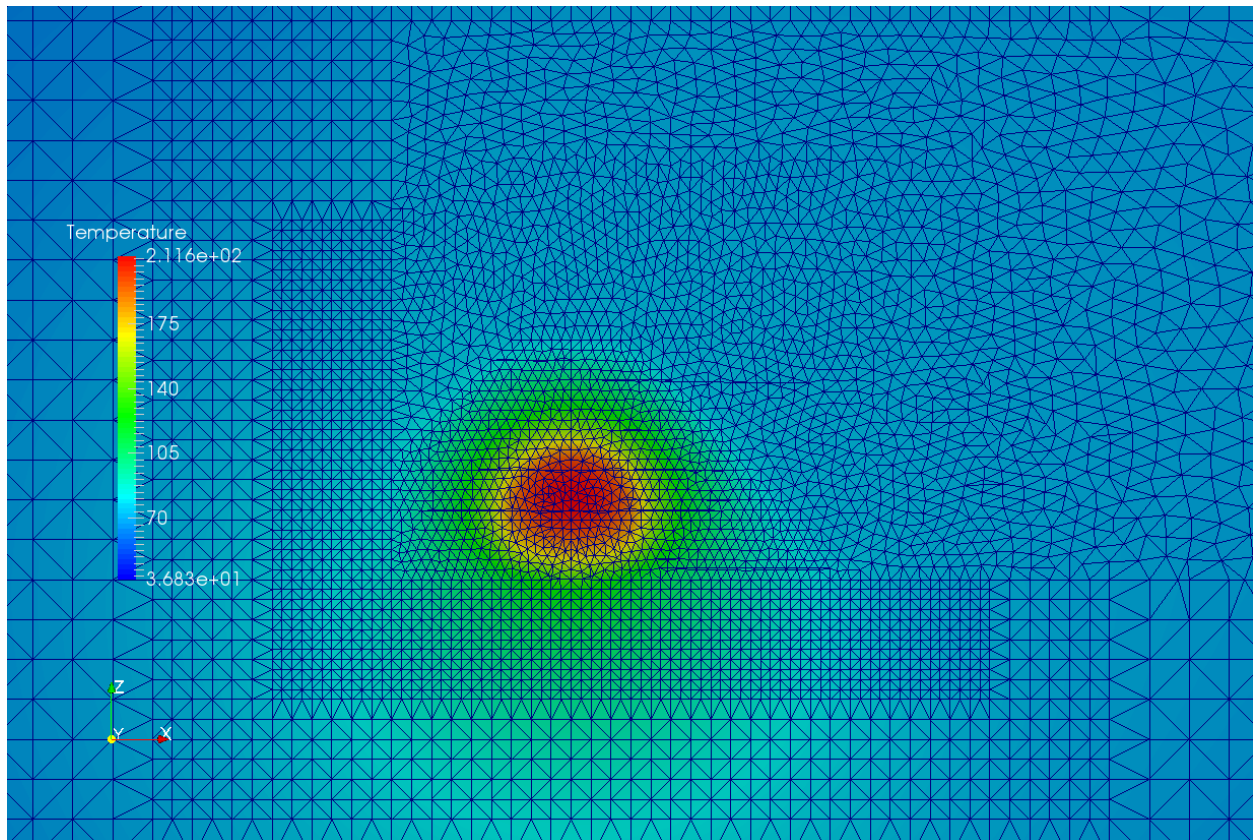
Figure 35: Temperature profile with low capillary suction in pile. Rounded shape indicates dominantly conductive heat transfer with heat dissipating in relatively conductive floor. Maximum temperature is 180.2°C.

When capillary pressure is high enough to draw water out of the floor and into the pile, but low residual saturation allows the pile to progressively dry, overall temperature of the pile is reduced (Figure 36). Temperature contours are wider relative to their height. Surface temperature in the pile is similar to the low-pressure runs, but peak temperature in the canister is reduced to 152°C and the overall thermal gradient is reduced. Note that the temperature scale in Figure 36 is the same as Figure 35. The presence of water through much of the run and the additional water drawn into the pile by capillary suction provides a considerable heat sink, enhanced further by boiling. If residual saturation is higher, then even greater amounts of water are pulled into the pile and temperatures are further suppressed. When water is retained in the pore space, the higher thermal conductivity of water relative to air permits more rapid heat transfer.

Experiments and Modeling to Support Field Test Design
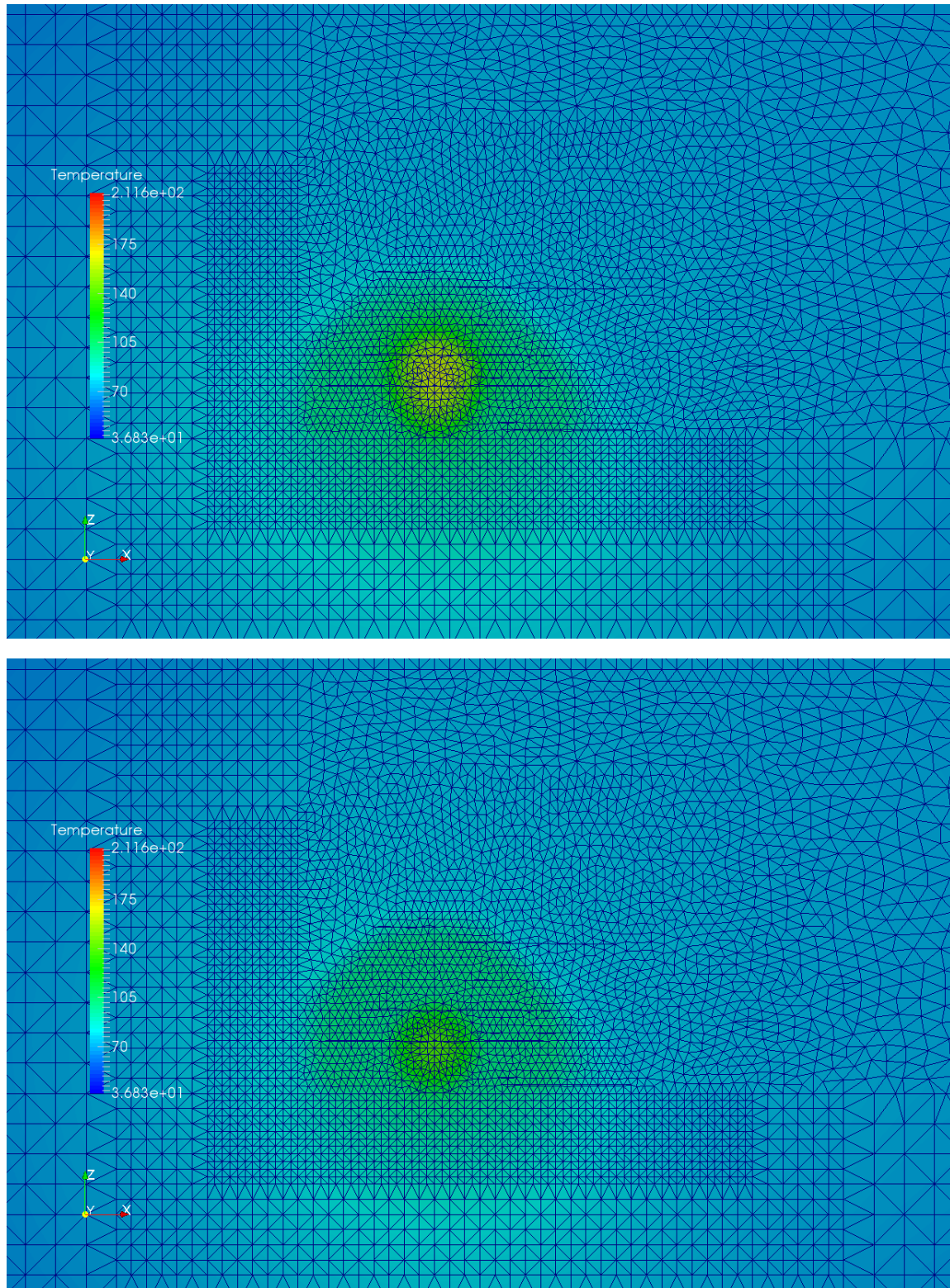
Figure 36: (Top) Temperature in runs with high capillary suction but where pile dries near canister; (bottom) temperature in runs where pile remains wet. Temperature scale is same as Figure 35, clearly showing relatively low temperatures when water is able to recharge in the pile for some or all of the model runtime.

Although the patterns of heat are indicative of primarily conductive heat transfer, a plot of vertical flow velocities (Figure 37) shows that convection is induced in the gas phase. Upflow occurs along the drift wall with a downward countercurrent pulling air into the pile on the side outward into the gallery, causing a chimney effect. This aspect is important to consider for its impacts on porosity. Generally air being drawn into the pile on the outside would be relatively humid compared to rising air once the pore water on the rising air side boils off. As a result, additional air moisture may be available to the pile which can provide a water source even in the absence of an input of water from beneath the pile. Humidity fluctuations were not accounted for in the present work and are a topic for future exploration.
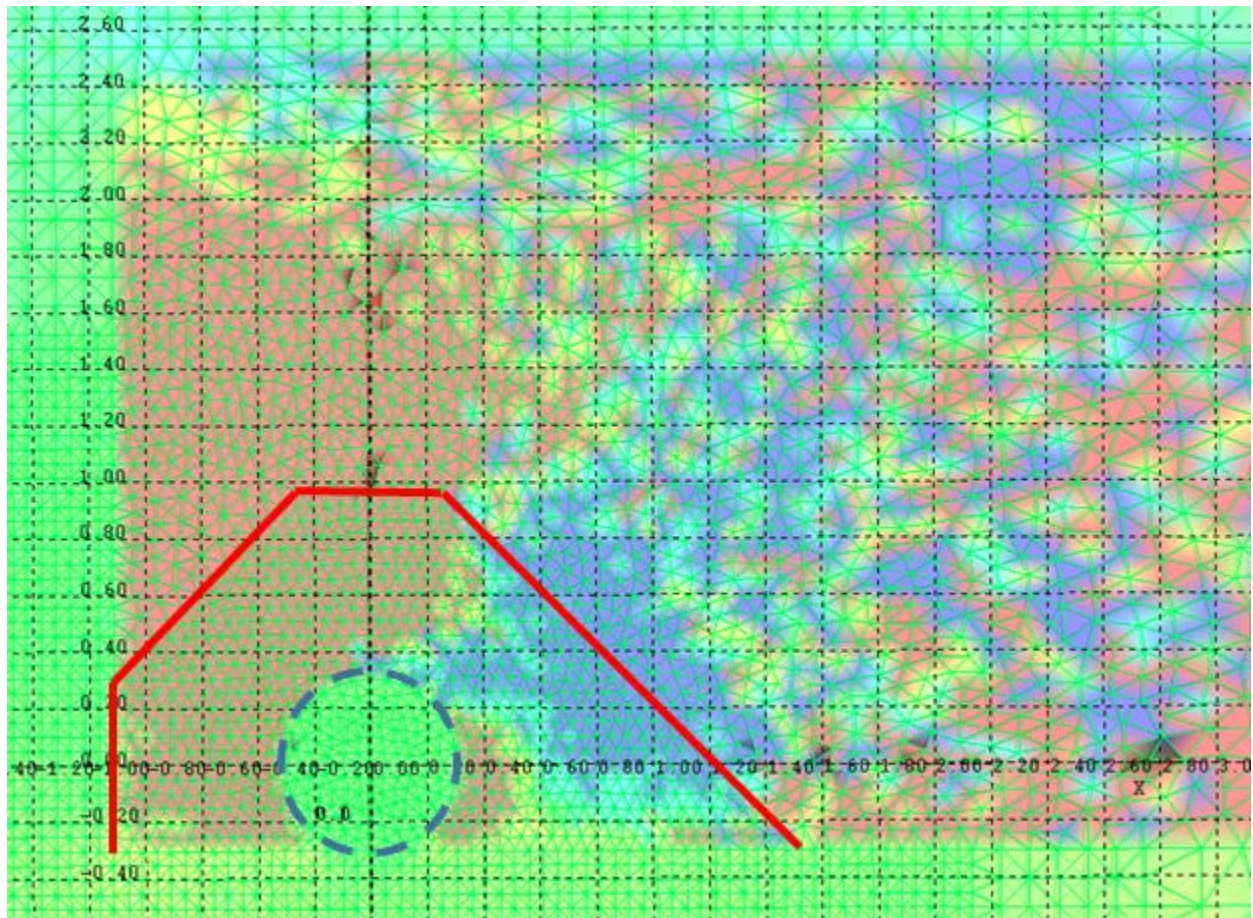
Figure 37: Vertical flow velocities in pile (red outline) and surrounding air. Orange colors indicate upward velocities, blue colors indicate downward velocities. The pile and air against the gallery wall experiences upflow, with downward flow pulling air into the pile on the side jutting outward into the gallery.

Experiments and Modeling to Support Field Test Design

9.4.3 Porosity

As was the case in the Olivella-type models with no capillary suction or with an impermeable model domain, the migration of porosity depends heavily on the ability of the domain to recharge water. For the model runs where capillary suction pressures are low, there is essentially no change in the pile except for very minor increases where the pile meets the wall and floor of the gallery (Figure 38). Inability to draw additional water into the domain once the starting moisture content has boiled off prevents any further change from occurring.
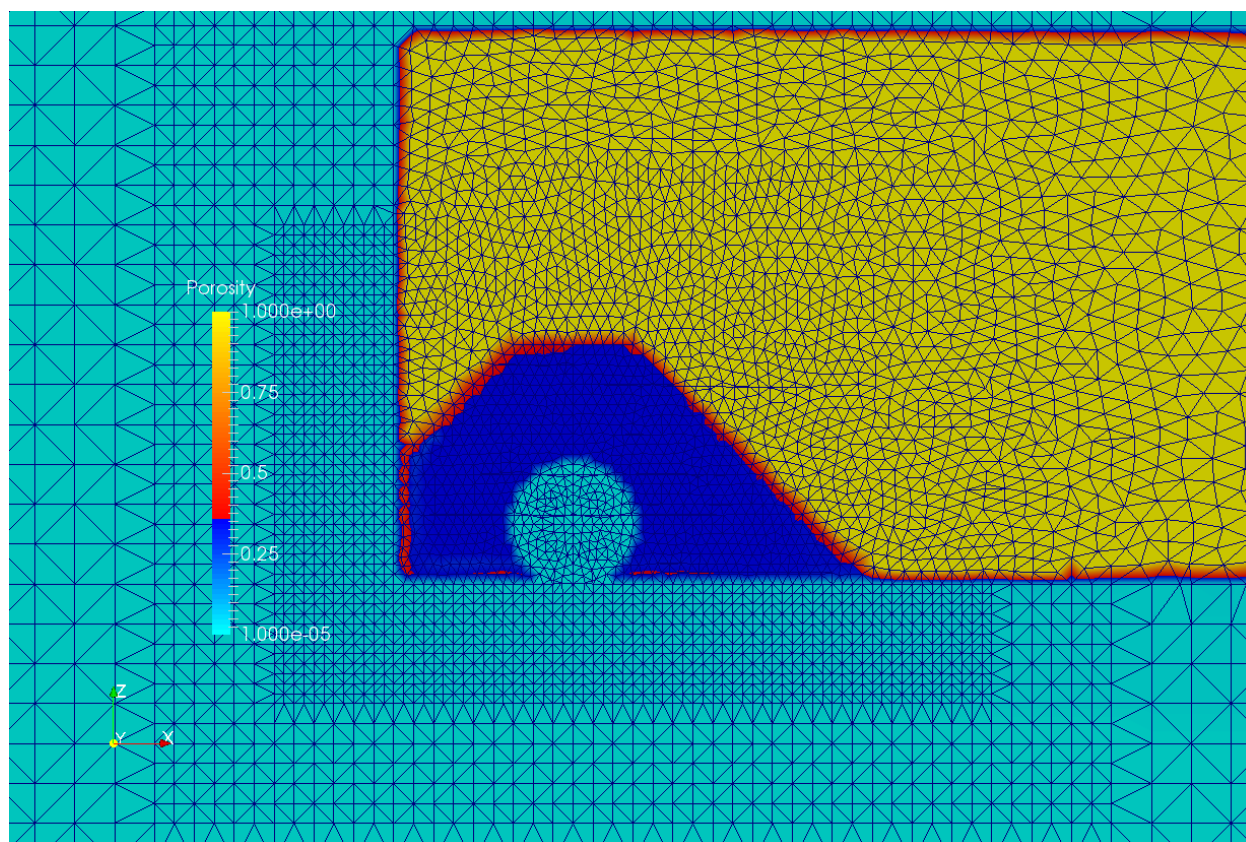
Figure 38: 365-day porosity with very low capillary suction. Dark blue color indicates porosity at or very slightly below 0.35. Red color indicates porosity slightly above 0.35, showing where dissolution has occurred. Note that much of the red color along the gallery walls other than around the pile is a contouring effect in the visualization software and not indicative of dissolution.

Porosity results with higher capillary suction generally follow one of two patterns which relate to the saturation of the pile over time and are distinguished by the location and magnitude of the dissolution front surrounding the canister (Figure 39). In both cases, porosity generally decreases to near zero within the first few centimeters of the heater, forming an essentially impermeable rind around the canister. The thickness and precise shape of this rind varies between runs. When the pile is able to dry, the rind is thickest horizontally along the middle of the canister and thinnest near the base. Condensing brine tends to flow downward and collect in the bottom of the pile, increasing porosity and thinning the rind downward and away from the canister and leaving a localized high porosity. In runs with more water available or higher

residual saturation, the rind is rounder and more uniform in thickness. Typical rind thickness is approximately 20 cm at the top and sides and down to a few cm around the bottom of the canister.

The dissolution front is highly variable between runs. When the pile remains wet, a strong dissolution front develops above the canister, with porosity approaching 1. These nodes retain some degree of saturation (typically near residual saturation) despite being highly porous, permeable, and surrounded by similarly porous nodes. This combination of high saturation and high porosity motivates the continuing development and refinement of the $P_c(n, S_l)$ capillary suction model (Section 2). If the pile dries, a porosity increase to about $n = 0.75$ is observed for a few nodes on the sides of the canister, but the pile above the canister increases to only about $n = 0.5$. Areas with high dissolution are not as extensively saturated. These differences result from the drying of the pile before full dissolution can occur in most nodes.

The surface of the pile in both cases shows a general increase in porosity where the upflowing chimney effect occurs. Portions of the pile surface show an etching effect where small clusters of nodes experience severe dissolution. Additional dissolution occurs where the pile meets the wall of the gallery and is able to draw water out of the wall. On the gallery side where relatively cool ambient air is drawn into the pile, less dissolution occurs in most model runs, and the toe of the pile where it sticks out farthest into the gallery shows very little change in some runs. Lower porosity increases in this region may be a product of the overall heating throughout the pile which counteracts the incorporation of moisture from the air, prevents condensation, and focuses changes toward the top of the chimney where temperatures drop the most rapidly. Further efforts are in progress to examine the effects of variable humidity in the air.

Both the damaged wall rock and the denser intact salt beyond the gallery show little effect in any of the models. Long term minor desaturation occurs in the background run due to the high pressure gradient between ~15 MPa groundwater at depth and the induced atmospheric air pressure within the carved gallery. Total volumes of water released from the intact wall are minor, however, due to the low porosity. Some small amount of the remaining brine turns to vapor during the heating of the domain, but this amount is negligible because the temperature change is only a few tens of degrees Celsius and there is so little fluid present. Permeability is low enough in even the damaged salt region that brine and vapor migration is limited. Between the very low volumetric brine content and the inability of that brine or its vapor to move, no noticeable changes occur to the porosity or permeability of the wall rock. The primary function of these regions is as a source of a small amount of water and as a heat sink. However, because there are changes in moisture content and temperature of these areas, it is preferable to leave them in the model domain rather than defining them as boundaries with steady conditions.

Experiments and Modeling to Support Field Test Design
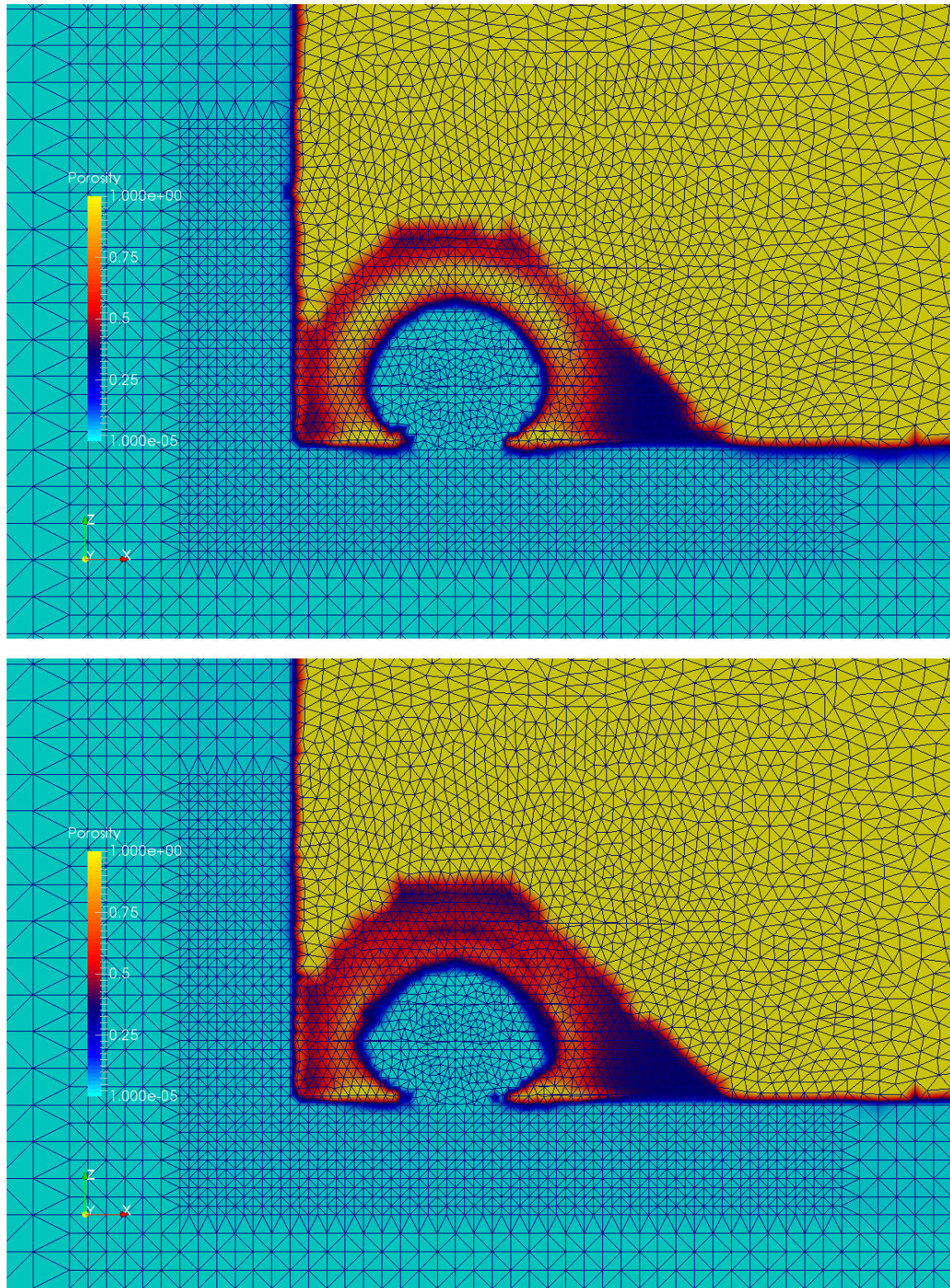
Figure 39: (Top) Porosity of pile with strong capillary suction and high residual saturation, showing severe dissolution of pile above canister. (Bottom) Porosity of pile with lower residual saturation, showing weaker dissolution in much of pile. In both cases a rind of low-porosity salt has developed around the canister.

9.5 Discussion

Three potential types of results are predicted based on the presented numerical models, with a dominant sensitivity to the capillary suction pressure of the domain and its consequent draw of water into the pile to replace evaporated brine water. If capillary suction is low, the inability of the pile to recharge water causes the pile to dry quickly. Porosity changes very little in this scenario, but temperatures throughout the pile are much higher due to the lack of heat sinks and inefficient heat transfer through air.

When capillary pressures are higher, one of two outcomes will result depending on whether capillary forces are sufficient to keep water in the pile despite heating. If the pile is still able to gradually dry, then a rind of low-porosity, impermeable salt will grow around the canister that is thickest in the middle of the pile. Much of the pile will experience moderate dissolution beyond this rind, but with that dissolution distributed throughout much of the pile. Maximum temperature will be in the vicinity of 150°C with pile surface temperatures around 70°C. A stronger capillary influence model predicts a wet, relatively cool pile in which a round rind develops around the canister surrounded by a zone of near total dissolution of the salt. Three scenarios can be described based on these varying model results:

(1) Little effect on the porosity of the pile with higher temperatures, resulting from immediate and permanent drying of the entire pile;
(2) Moderate increases in porosity throughout much of the pile, accompanied by the development of a rind of dense, impermeable salt around the canister, resulting from capillary replenishment of water into the pile that adds additional water but is insufficient to prevent gradual pile drying; and
(3) Formation of a rind around the canister with strong dissolution of a band immediately beyond this rind, resulting from strong capillary forces preventing permanent drying of the pile surrounding the canister.

From these outcomes it is clear that a major factor in need of resolution for WIPP, and by extension a critical variable to determine at any generic salt repository in which in-drift disposal is considered, is the strength of capillary suction in the ROM salt covering the canister. Unfortunately, at this time experiments have not been conducted with WIPP salt. Retention curves described in Olivella et al. (2011) and the capillary experiments of Cinar et al. (2005) used table salt which is both physically different, in that it has a very consistent grain size compared to the poorly sorted WIPP ROM salt, and chemically different in that it lacks the variety of impurities found in rock layers at WIPP (Krieg, 1984; Lappin, 1988). Cinar et al. (2005) attempted to compact their samples and were able to reduce porosity to typical values for tightly packed spheres, but could not capture the variety of grain sizes that a ROM sample would include. Capillary pressures reported by both authors can range from <1 atmosphere (~0.1 MPa) to >4 atmospheres (0.4 MPa). Nevertheless, with the uncertainties in ROM salt characteristics, capillary suction may maximize at values even greater than that. Resolution of this variable is an important future step to improve numerical modeling procedures and constitutive relationships.

10 Future Work

Several areas of future exploration are possible depending on project needs for the coming 2018 fiscal year. Further efforts are required to enhance understanding of the constitutive functions for a generic salt disposal concept. These include experimental and numerical approaches to address uncertainties remaining with mechanical, thermal, and fluid processes in ROM and rock salt.

A large-scale single-heater experiment in ROM salt has begun at WIPP. Over the course of the 2018 fiscal year, this experiment will generate temperature and moisture data as well as a final assessment of the post-heating status of the ROM salt pile. Continued numerical experiments will be validated against this data set. In addition, small scale laboratory work directed towards an enhanced understanding of the unsaturated flow and capillary effects in WIPP ROM salt may help improve model inputs and results. This can be accomplished relatively quickly using established experimental techniques if programmatic goals require it. Experiments can combine with refinement and further application of capillary suction model functions in FEHM, especially the porosity-dependent function which is currently a unique capability with broad applications to any modeling work of generic salt that considers the fluid in the unsaturated zone. Related to this, several new code additions are planned or in progress, including a temperature-dependent specific heat capacity function which may be readily applied to the large temperature changes observed in the salt system. A further possible addition to FEHM is a module to account for deformation of salt beyond dissolution and precipitation, such as thermal strain-induced porosity changes as heated salt expands, or the creation of cooling joints when salt rapidly cools.

11 References

Bechthold, W., E. Smailos, S. Heusermann, W. Bollingerfehr, B. Sabet, T. Rothfuchs, P. Kamlot, J. Grupa, S. Olivella, and F.D. Hansen, 2004. Backfilling and sealing of underground repositories for radioactive waste in salt (Bambus II project). Final Report for European Atomic Energy Community EUR 20621, Office for Official Publications of the European Communities, Luxembourg.

Birkholzer, J.T. 2004. Estimating liquid fluxes in thermally perturbed fractured rock using measured temperature profiles. Journal of Hydrology 327(3-4): 496-515, doi:10.1016/j.jhydrol.2005.11.049.

Bourret SM, Johnson PJ, Zyvoloski GA, Chu SP, Weaver DJ, Otto S, Boukhalfa H, Caporuscio FA, Jordan AB, and Stauffer PH, 2016. Experiments and modeling in support of generic salt repository science. Los Alamos National Laboratory, USDOE Used Fuel Disposition Campaign, Final Report LA-UR-16-27329

Bourret SM, Otto S, Johnson PJ, Weaver DJ, Boukhalfa H, and Stauffer PH, 2017. High level waste in salt repositories: Experiments and simulations of evaporation in the underground. Waste Management 2017 Proceedings.

Brooke RH and Corey AT, 1964. Hydraulic properties of porous media. Hydrology Papers, Colorado State University, Fort Collins, Colorado.

Brunnengräber A, Di Nucci MR, Isodoro Losada AM, Mez L, and Schreurs MA, 2015. Nuclear waste governance: An international comparison. Springer Fachmedien Weisbaden, German, ISBN 978-3-658-08961-0, DOI 10.1007/978-3-658-08962-7

Buckles RS, 1965. Correlating and averaging connate water saturation data. Journal of Canadian Petroleum Technology 9(1), 42-52.

Caporuscio, F.A., H. Boukhalfa, M.C. Cheshire, A.B. Jordan, and M. Ding. 2013. Brine Migration Experimental Studies for Salt Repositories. FCRD Used Fuel Disposition Campaign Milestone FCRD-UFD-2013-000204, September 25, 2013.

Chipera SJ and Vaniman DT, 2007. Experimental stability of magnesium sulfate hydrates that may be present on Mars. Geochimica et Cosmochimica Acta, 71, 241–250.

Cinar, Y., G. Pusch, and V. Reitenbach. 2006. Petrophysical and capillary properties of compacted salt. Transport in Porous Media 65(2), 199-228.

Clayton DJ and Gable CW, 2009. 3-D Thermal analyses of high-level waste emplaced in a generic salt repository. Advanced Fuel Cycle Initiative, AFCI-WAST-PMO-MI-DV-2009-000002, SAND2009-0633P, LA-UR-09-0089.

Doughty, C., and K. Pruess. 1990. A similarity solution for two-phase fluid and heat flow near high-level nuclear waste packages emplaced in porous media. International Journal of Heat and Mass Transfer 33(6): 1205–1222.

Fahland S and Heusermann S, 2013. Geomechanical analysis of the integrity of waste disposal areas in the Morsleben repository. Rock Characterisation, Modelling, and Engineering Design Methods, Taylor & Francis Group, London, ISBN 978-1-138-00057-5

Fahland S, Heusermann S, Schäfers A, Behlau J, and Hammer J, 2015. Three-dimensional geological and geomechanical modelling of a repository for waste disposal in deep rock salt formations. 13th ISRM International Congress of Rock Mechanics, International Society for Rock Mechanics, ISRM-13CONGRESS-2015-005

Fitts CR, 2013. Groundwater Science, second edition. Elsevier Inc., Waltham, MA, ISBN: 978-0-12-384705-8.

Forsyth PA, 1988. Comparison of the single-phase and two-phase numerical model formulation for saturated-unsaturated groundwater flow. Computer methods in applied mechanics and engineering 69, 243-259.

Hansen, F.D., and C.D. Leigh. 2011. Salt disposal of heat-generating nuclear waste. Sandia National Laboratories Report SAND2011-0161. Albuquerque, NM.

Hansen FD, Leigh C, Steininger W, Bollingerfehr W, and von Berlepsch T, 2015. Proceedings of the 5th US/German Workshop on Salt Repository Research, Design, and Operation. Sandia National Laboratories, FCRD-UFRD-2015-00514, SAND2015-0500R

Hansen FD, Steininger W, and Bollingerfehr W, 2016. Proceedings of the 6th US/German Workshop on Salt Repository Research, Design, and Operation. Sandia National Laboratories, FCRD-UFRD-2016-00069, SAND2016-0194 R

Hansen FDM Steininger W, and Bollingerfehr W, 2017. Proceedings of the 7th US/German Workshop on Salt Repository Research, Design, and Operation. Sandia National Laboratories, SFWD-SFWST-2017-000008, SAND2017-1057R

Holmes M, Holmes A, Holmes D, 2009. Relationship between porosity and water saturation: methodology to distinguish mobile from capillary bound water. AAPG Annual Convention and Exhibition, Denver, CO.

Jordan, A.B., H. Boukhalfa, F.A. Caporuscio, and P.H. Stauffer. 2015a. Brine Transport Experiments in Run-of-Mine Salt. Los Alamos National Laboratory Report LA-UR-15-26804. Los Alamos, NM.

Jordan, A.B., Zyvoloski, G.A., Weaver, D.J., Otto, S., and Stauffer, P.H., 2015b. Coupled Thermal-Hydrologic-Chemical Model for In-Drift Disposal Test. Los Alamos National Laboratory Report LA-UR-15-27442. Los Alamos, NM.

Jordan, A.B., H. Boukhalfa, F.A. Caporuscio; B.A. Robinson, P.H. Stauffer. 2015c. Hydrous Mineral Dehydration around Heat-Generating Nuclear Waste in Bedded Salt Formations. Environmental Science & Technology, 5:1-13. DOI: 10.1021/acs.est.5b01002.

Krieg RD, 1984. Reference stratigraphy and rock properties for the Waste Isolation Pilot Plant (WIPP) project. Sandia National Laboratories Report, SAND-83-1908

Krumhans JL, Stein CL, Jarrell GD, and Kimball KM, 1991. Summary of WIPP Room B heater test brine and backfill material data. Sandia National Laboratories SAND90-0926.

Kumar G and Prabhu KN, 2007. Review of non-reactive and reactive wetting of liquids on surfaces. Advances in Colloid and Interface Science 133, 61-89. Doi: 10.1016/j.cis/2007.04.009

Kuhlman, K.L., and B. Malama. 2013. Brine Flow in Heated Geologic Salt. Sandia National

Laboratories Report SAND2013-1944. Albuquerque, NM.

Kuhlman KL, Mills MM, and Matteo EN, 2017. Consensus on intermediate scale salt field test design. Sandia National Laboratories, SFWD-SFWST-2017-000099, SAND2017-3179-R

Lappin, A.R. 1988. Summary of site-characterization studies conducted from 1983 through 1987 at the Waste Isolation Pilot Plant (WIPP) site, southeastern New Mexico. In: Post, R.G; High-level waste and general interest: Volume II, p. 371-376. Waste Management: Symposium on Radioactive Waste Management, Tucson, AZ, 28 Feb – 3 Mar 1988.

Masoodi R and Pillai KM, 2012. A general formula for capillary suction-pressure in porous media. Journal of Porous Media 15(8), 775-783. DOI: 10.1615/JPorMedia.v15.i8.60

Miller TA, Vessilinov VV, Stauffer PH, Birdsell KH, and Gable CW, 2007. Integration of geologic frameworks in meshing and setup of computational hydrogeologic models, Pajarito Plateau, New Mexico. New Mexico Geological Society Guide Book, 58th Field Conference, Geology of the Jemez Mountain Regions III.

Molecke MA, Bradley DJ, and Shade JW, 1981. PNL-Sandia HLW package interactions test: Phase one. Scientific Basis for Nuclear Waste Management 6, SAND81-1442C.

Molecke MA, 1983. A comparison of brines relevant to nuclear waste experimentation. Sandia National Laboratories, SAND83-0516.

Olivella, S., S. Castagna, E.E. Alonso, and A. Lloret. 2011. Porosity variations in saline media induced by temperature gradients: experimental evidences and modeling. Transport in porous media, 90(3): 763-777.

Powers DS, Lambert SJ, Shaffer S, Hill LR, and Weart WD, 1978. Geological characterization report Waste Isolation Pilot Plant (WIPP) site, southeastern New Mexico. Sandia National Laboratories, SAND78-1596, Vol. 1

Robinson, B.A., N.Z. Elkins, and J.T. Carter. 2012. Development of a US Nuclear Waste Repository Research Program in Salt. Nuclear Technology, 180(1): 122-138.

Rutqvist, J. L.B. Martin, S. Molins, D. Trebotich, and J. Birkholzer. 2016. Modeling Coupled THM Processes and Brine Migration in Salt at High Temperatures. UFD Document FCRD-UFD-2015-000366, LBNL-191216.

Spinelli GA and Fischer AT, 2004. Hydrothermal circulation within rough basement on the Juan de Fuca Ridge flank. Geochemistry Geophysics Geosystems 5(2), Q02001, doi:02010.01029/02003GC000616.

Stauffer PH, Birdsell KH, Witkowski MS, and Hopkins JK, 2005. Vadose zone transport of 1,1,1-trichloroethane. Vadoze Zone Journal 4(3), 760-773.

Stauffer PH, Harp DR, Jordan AR, Lu Z, Kelkar S, Kang Q, Ten Cate J, Boukhalfa H, Labayed Y, Reimus PW, Caporuscio FA, Miller TA, and Robinson BA, 2013. Coupled model for heat and water transport in a high level waste repository in salt. Los Alamos National Laboratory Document, LA-UR-13-27584.

Stauffer PH, Jordan AB, Weaver DJ, Caporuscio FA, Ten Cate JA, Boukhalfa H, Robinson BA, Sassini DC, Kuhlman KL, Hardin EL, Sevougian SD, MacKinnon RJ, Wu Y, Daley TA, Freifeld BM, Cook PJ, Rutqvist J, and Birkholzer JT, 2015. Test proposal document for

phased field thermal testing in salt. FCRD Used Fuel Disposition Campaign Milestone FCRD-UFD-2015-000077.

Van Genuchten MT, 1980. A closed-form equation for predicting the hydraulic conductivity of unsaturated soils. Soil Science Society of America Journal 44(5).

Winslow DM, Fisher AT, Stauffer PH, Gable CW, and Zyvoloski GA, 2016. Three-dimensional modeling of outcrop-to-outcrop hydrothermal circulation on the eastern flank of the Juan de Fuca Ridge. Journal of Geophysical Research: Solid Earth 121(3), DOI: 10.1002/2015JB012606

Wollrath J, Mauke R, Mohlfeld M, Niemeyer M, and Becker DA, 2014. Morsleben repository – Interdependence of technical feasibility and functionality of geotechnical barriers and safety case development. Radioactive Waste Management NEA/RWM/R(2013)9

Yu Q and Brouwers HJH, 2012. Thermal properties and microstructure of gypsum board and its dehydration products: A theoretical and experimental investigation. Fire and Materials, 36(7), 575-589.

Zyvoloski GA, Robinson BA, Dash ZV, Kelkar S, Viswanathan HS, Pawar RJ, Stauffer PH, Miller TA, and Chu SP, 2012. Software users manual (UM) for the FEHM Application Version 3.1-3.X, LANL Report, LA-UR-12-24493

Appendix A: **Additions and Usage of New Capillary model**

Usage and sample model inputs for the new capillary suction models are collated here. All specifications go under control statement *rlp*. The user inputs the model number as -666, consistent with numeric flags applied elsewhere in the salt model. Inputs of initial residual saturation (S_{ri}), initial porosity (n_i), initial maximum capillary pressure (P_{cmaxi}), and a flag indicating whether to apply a saturation above which capillary pressure goes to zero (S_{lmax}) are read and must be filled. At the present time Sri is calculated using the linear method. S_{lmax} is a binary usage specified with flag *fS_{lmax}*, where it is either held at 1 or decreases linearly as porosity increases. If the initial porosity input is specified at 0 then porosity is read from the global variables within FEHM. If n_i is greater than 0, then the user entered value is used instead.

Relevant inputs for the new model follow:

Control statement rlp (optional)

Group 1 – IRLP(i), S_{ri}, n_i, P_{cmaxi}, fS_{lmax}

Group 2 – JA, JB, JC, I

Input Variable	Format	Description
IRLP(i)	Integer	Relative permeability model type; -666 specifies new function
S_{ri}	Float	Residual saturation
n_i	Float	Initial porosity, if 0 then global variable is used instead
P_{cmaxi}	Float	Initial maximum capillary pressure at residual saturation
fS_{lmax}	Integer	Flag denoting whether the saturation at which capillary pressure goes to zero changes (0) or remains fixed at 1 (>0)

Example 1: Global variable porosity input (n_i), decreasing S_{lmax}. S_{ri} is specified at 0.1and P_{cmaxi} at 0.013 MPa.

rlp
 -666 0.1 0 0.013 0

1 0 0 1

Experiments and Modeling to Support Field Test Design

Example 2: User entered initial porosity n_i of 0.35, decreasing S$_{lmax}$.

rlp
 -666 0.1 0.35 0.013 0

1 0 0 1

Example 3: User entered initial porosity, S_{lmax} held fixed at 1.

rlp
 -666 0.1 0.35 0.013 1

1 0 0 1

Appendix B: Paper published in WM 2017 journal

High Level Waste in Salt Repositories: Experiments and Simulations of Evaporation in the Underground – 17167

Suzanne Bourret*, Shawn Otto**, Peter J. Johnson***, Douglas Weaver**, Hakim Boukalfa****, Philip Stauffer*

*Computational Earth Sciences Group, Los Alamos National Laboratory

**Repository Science and Operations Program, Los Alamos National Laboratory

***University of Buffalo, Department of Geology

****Earth Systems Observation Group, Los Alamos National Laboratory

LA-UR-16-28158

ABSTRACT

Advances in simulation of coupled heat and mass transfer in granular salt using the Finite Element Heat and Mass Transfer Code (FEHM) is presented in this paper. The modeling focuses on reproducing the results of an in-situ subsurface evaporation experiment beginning during the summer of 2015 carried out in the underground at the Waste Isolation Pilot Plant (WIPP). Run-of-mine (granular) salt was placed in a metal pan, and sample mass, as well as ambient temperature and humidity, were measured continuously on a data logger through May 2016. Changes in moisture content of the salt are interpreted from the change in mass, and these data provide insight into evaporation and water retention characteristics from salt in the WIPP underground.

To allow simulation of the experimental data, FEHM was modified to include a variable humidity boundary condition. The new humidity boundary condition can adjust streams of inflowing air to reflect fractions of air and water at prescribed temperature and pressure conditions that in turn represent relative humidity. Attributes for the flow such as temperature, air mass fraction, and humidity can be specified for inflowing air. The in-situ experiment provided data for validation of FEHM code development to accurately compute water-vapor pressure lowering due to dissolved salt and capillary pressure for pore water stored granular WIPP salt. Using this new boundary condition capabilities, a numerical representation of the pan experiment was created. The numerical domain is a 2-dimensional square grid of 30 by 30 cm axes. Salt and air properties are assigned based on measured values. A low flow rate of air is specified across the pile of salt to represent drift ventilation airflow. Humidity and temperature of the flowing air are fixed to measured values, and the simulated pile of salt is allowed to take up or release water based only on gradients in humidity and water-vapor pressure. Mass changes of the modeled salt pan were compared to measured mass changes in the bench-scale experiment. Directionality of the modeled changes tracks well with measured values, with good correlation between peak and valley inflection points. This shows that in situations with airflow where the relative humidity boundary can apply, FEHM can produce accurate values if humidity, air flow, and initial conditions are well established. Finally, this work supports phased-field-thermal testing in salt planned for the underground at

Experiments and Modeling to Support Field Test Design

WIPP that is expected to begin in early 2017.

INTRODUCTION

As part of the Department of Energy's (DOE) Environmental Management (EM) and Nuclear Energy (NE) research programs into nuclear waste repositories, Los Alamos National Laboratory (LANL) has been involved in both experiments and simulations that seek to increase our understanding of the complex and coupled processes that occur when hot waste interacts with salt formations in the underground. Specific objectives related to disposal system performance are defined in an update to the UFD Campaign Implementation Plan [1]. For 2013-2016 the research has focused on using theory, experiments, and modeling in combination with existing underground research laboratory (URL) data to assess disposal system performance, including reduction of uncertainty associated with heat-generating nuclear waste (HGNW). HGNW is defined herein as the combination of both heat-generating defense high-level waste (DHLW) and civilian-spent nuclear fuel (SNF). Thermal, hydrological, mechanical, and chemical (THMC) coupling and related modeling, as well as development of a field testing plan are discussed in this objective.

Salt is an attractive material for the disposition of HGNW because of its self-sealing, viscoplastic, and reconsolidation properties [2]. The rate at which salt consolidates and the properties of the consolidated salt depends on the composition of the salt, including its weight percent of accessory minerals and moisture content, and the temperature under which consolidation occurs. Physicochemical processes, such as mineral hydration/dehydration, salt dissolution, and precipitation significantly influence the rate of salt structure changes.

Brine and mixed-phase migration of fluids in salt is important for understanding the self-sealing behavior of a salt repository [3]. Experimental studies have demonstrated that porosity may migrate towards a thermal source for small-scale fluid inclusions within salt crystals [4]. However, in some conditions when pore space in salt is sufficiently connected for fluid migration to occur, porosity may be expected to migrate away from a heat source [5]. As saline water evaporates, salt concentrations increase until saturation is reached; as further water is removed, salt will begin to precipitate into void spaces previously occupied by water. Consequently, areas in which evaporation is occurring tend to be self-sealing, with reductions in porosity and permeability [2]. Evaporated water, however, will condense as temperature decreases, resulting in dissolution of salt farther afield and increases in porosity and permeability [6]. The water, brine, and gas content of the salt is dynamic in the subsurface at the WIPP, and will change with the temperature and humidity conditions of the forced ventilation air in the waste storage galleries and access drifts. Properly representing saturation in our modeling efforts of HGNW repositories at WIPP is critical for predicting the THMC deformation and self-sealing behavior of the salt that create a safe long-term environment for HGNW storage.

Another behavior of vapor and liquid water in salt to consider for HGNW storage is the vapor pressure lowering for saline water. Water-vapor pressure (P_{wv}) lowering due to dissolved salt in liquid water is an important process to accurately represent in simulations of gas and water flow in porous salt. P_{wv} can be thought of as the tendency of liquid water to change phases. As this value approaches ambient (i.e. atmospheric) pressure, increasing amounts of water will go into the vapor phase. As temperatures increase, P_{wv} will also increase because the air has a greater capacity to hold water vapor at warmer temperatures; the temperature-P_{wv} relationship follows an exponential curve with P_{wv} increasing more rapidly as air warms (Figure 40). In contrast, increased solute concentration has the opposite effect. The addition of salt lowers the P_{wv} of saline brine compared to equivalent pure water and therefore raises the boiling point of water.
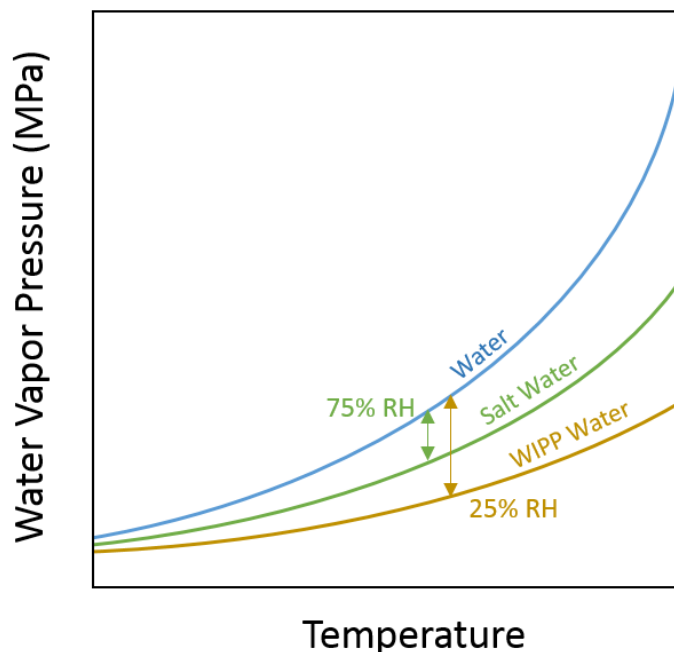
Figure 40: Conceptual model of water vapor pressure for pure water (blue), water containing salt (green), and water in granular WIPP salt (yellow).

The P_{wv} lowering tendency of water with dissolved WIPP run-of-mine (RoM) salt is greater than for salt-saturated water, and likely depends on the capillary pressure in pore spaces of RoM salt. P_{wv} for water saturated with pure salt is lowered, requiring the relative humidity of the air to be about 25 % lower than the relative humidity for a phase change to occur for pure water. With the combination of the dissolved salt (and other accessory minerals) along with the liquid-water retention caused by capillarity in granular salt, it may be expected that P_{wv} would be depressed even more than in pure salt (Figure 1). Field observation of in WIPP RoM salt suggests that as vapor pressure is lowered, the relative humidity of the air must be about 75 % lower to cause phase changes, as compared to pure water. This is a considerable decrease in the exchange between the liquid water and vapor-phase water. The added influence of salt on P_{wv} is important for retention characteristics of water within pores and the consequent dissolution and precipitation of salt in the presence of a thermal gradient.

Understanding the behaviors of these complex and coupled processes that control the self-sealing behavior of salt is important for safe design for disposal of HGNW in salt formations, so experimentation and modeling is underway to characterize these processes. Because of the complicated physics involved with the THMC changes in granular salt, numerical modeling of salt has required the addition of many capabilities to the Finite Element Heat and Mass Transfer Code (FEHM; https://fehm.lanl.gov), a hydrologic multiphase flow and transport model developed at Los Alamos National Laboratory [7, 8, 9]. Although the code was originally intended to simulate geothermal reservoirs, subsequent revisions and additions in the past 30 years have allowed it to solve for unsaturated flow, reactive chemistry, stress, and carbon dioxide. FEHM uses a finite volume method for solving the conservation of mass and momentum equations. These additions consist of a new module specifically designed for simulation of salt, as well as

Experiments and Modeling to Support Field Test Design

minor changes to the fundamental FEHM code. Subsequent code corrections have been implemented for numerical efficiency and accuracy.

To validate the new physics included for modeling salt with FEHM, we are comparing simulation results to those of simple experiments and analytical solutions to isolate specific behavior. The work presented in this paper builds on previous experimental work, code development, and associated modeling [10, 11, 12, 13, 14, 15]. This paper discusses an experiment performed at WIPP, in the URL, and shows how FEHM simulations are reproducing physical behaviors of the system. An experiment was constructed underground at WIPP in which RoM salt was placed in a metal pan, and ambient temperature, humidity, and sample mass were measured continuously from May 2015 through May 2016. Comparison of modeled to experimental results allow for validation of FEHM salt-modeling capabilities, and build confidence in results for further modeling for HGNW testing and disposal design.

DESCRIPTION

Experimental Setup

A simple, long-term experiment was constructed for observing mass fluctuations of RoM salt in response to changes in relative humidity of air in a gallery In the URL at the WIPP site. Two pans were filled with RoM salt and placed on scales to measure the mass changes for the period of July 10, 2015 to May 3, 2016. The humidity and temperature of the air in the gallery was also measured; the three measurements were recorded simultaneously every 10 minutes.

Figure 41: Salt pan experiment in WIPP salt gallery. Pans with salt piles are on left.

Model setup

Experiments and Modeling to Support Field Test Design

Modeling of the WIPP salt pan experiment is on a 2-dimensional, 0.3 m by 0.3 m square grid (Figure 3). The grid has uniform 0.01 m spacing resulting in 960 nodes and 900 elements. Salt and air zones are defined; salt properties are as described in TABLE I. Porosity and initial saturation estimates were determined from lab measurement of RoM salt in the rock mechanics laboratory at LANL. The permeability was based on estimates of permeability of granular rocks of other mineralogies (Fetter, 2001). The salt zone is asymmetric to create the cone geometry in a radial space of the pans in the experiment as the salt was higher in the middle than the sides.
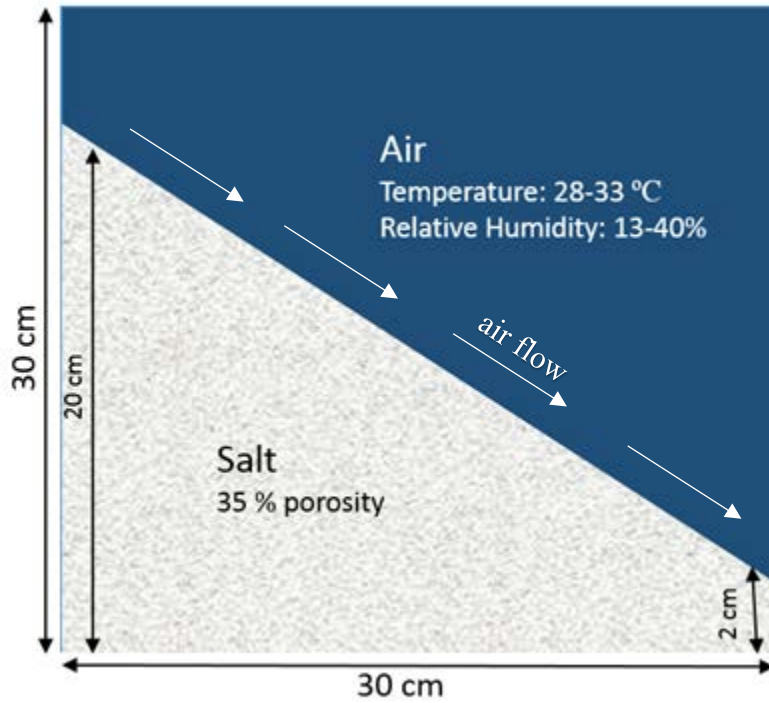
Figure 42: Model domain for salt pan experiment.

APPENDIX B - TABLE XII: Salt properties used in modeling.

Property	Value	Units
Solid Density [16]	2165.0	kg/m^3
Specific Heat Capacity *	931.0	J/kg·K
Permeability ♦	1×10^{-12}	m^2
Thermal Conductivity [14]+	2.0	W/m·K
Porosity ♦	0.35	-
Initial saturation ♦	0.4	-

* Bulk value based on porosity of 35 %, $cp,bulk = (1 - \phi)cp,salt + \phi cp,air$

+ Eq. 2-4 in *Stauffer et al.*, 2013, based on porosity of 35%

♦ Based on lab measurement

To represent the changing humidity boundary condition, the macro control statement *fxa* was implemented. This statement applies a time-variant mixing ratio of air mass to water-vapor mass. We determined the mass-fraction of air to water from the measured record of humidity in the gallery from the field measurements of temperature and humidity. For reference, a mixing ratio approaching 1 represents dry air, and as the mass of water in the vapor phase increases as the air is wetted, the ratio will decrease. The input values for *fxa* statement require simulation of flowing air. To accommodate this in the model, a pressure change of 1×10^{-5} MPa (10 Pa) over 30 cm was applied causing a slight inflow of air directly above the peak of the cone and a slight outflow of air directly above the low point at coordinates (30, 0.3) cm. A low flux of air with the desired water vapor mixing ratio would pass across the top of the salt cone and evaporate or condense pore water based on proportional water content of the air. The transient mixing ratio applied with *fxa*, in conjunction with measured temperature in the galley, provides FEHM the data to calculate a relative humidity boundary condition in the air.

A background run was conducted first to reach a steady-state, initial condition for subsequent simulations. A 12-day model run was conducted using laboratory-measured temperature and humidity conditions.

RESULTS AND DISCUSSION

Experiment

We observed from the RoM-salt-filled pan that increased evaporation tends to track with decreases in the relative humidity in the surrounding air. Figure 4 shows the comparison of the measured change in mass of the pan to the relative humidity of the air in the gallery. We assume that all changes in the mass of the salt are the result of evaporation and condensation of water in the liquid phase being stored in the pore spaces of RoM salt. We observed a significant drop in the mass of the pan in the first 30 days of the experiment, when the relative humidity of the air is relatively high (generally above 40 %), but we attribute this to evaporation of water from salt that was recently exposed to air. The transient salt saturation following the granular salt being newly exposed to air would explain this early-time mass loss. Following the first 30 days, we observe a drop in pan mass, and thus drying of the salt, when the relative humidity decreases, and a rebound in pan mass when there are increases in the relative humidity.

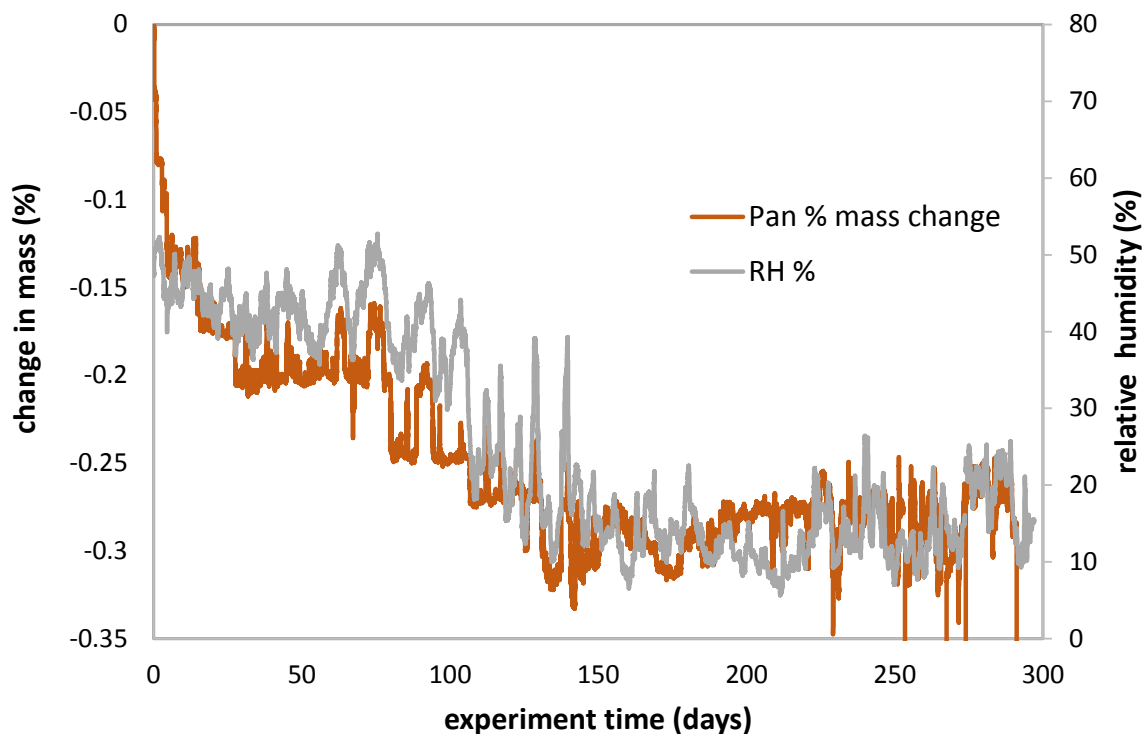Experiments and Modeling to Support Field Test Design

Figure 43: Change in mass (%) of crushed salt and relative humidity of air measured in the underground pan experiment at the WIPP site for the salt pan, for a portion of the experiment run-time between 7/10/2015 and 5/5/2016.

Modeling

Mass changes of the simulated salt cone are compared to measured mass changes in the bench-scale pan experiment for the same time period in Figure 5. Due to uncertainty in the exact dimensions of the salt cone, mass changes were normalized to the percentage change of the total mass. The model results are only reported for an eight-day period (4.5 – 12.5 days); the length of the modeled record was limited by simulation run-time and numerical convergence difficulties. Thus we only observe mass % fluctuations between about 0.1 % and 0.15 % over the 8-day record, a small range when compared to the 12-month experimental record shown in Figure 4 that ranges from 0.0 % to 0.4 %.

Directionality of the modeled changes tracks with measured values, with peak and valley inflection points correlating well. This shows that in situations with airflow with the *fxa* boundary applied, FEHM produces accurate values if humidity, air flow, and initial conditions are well established.
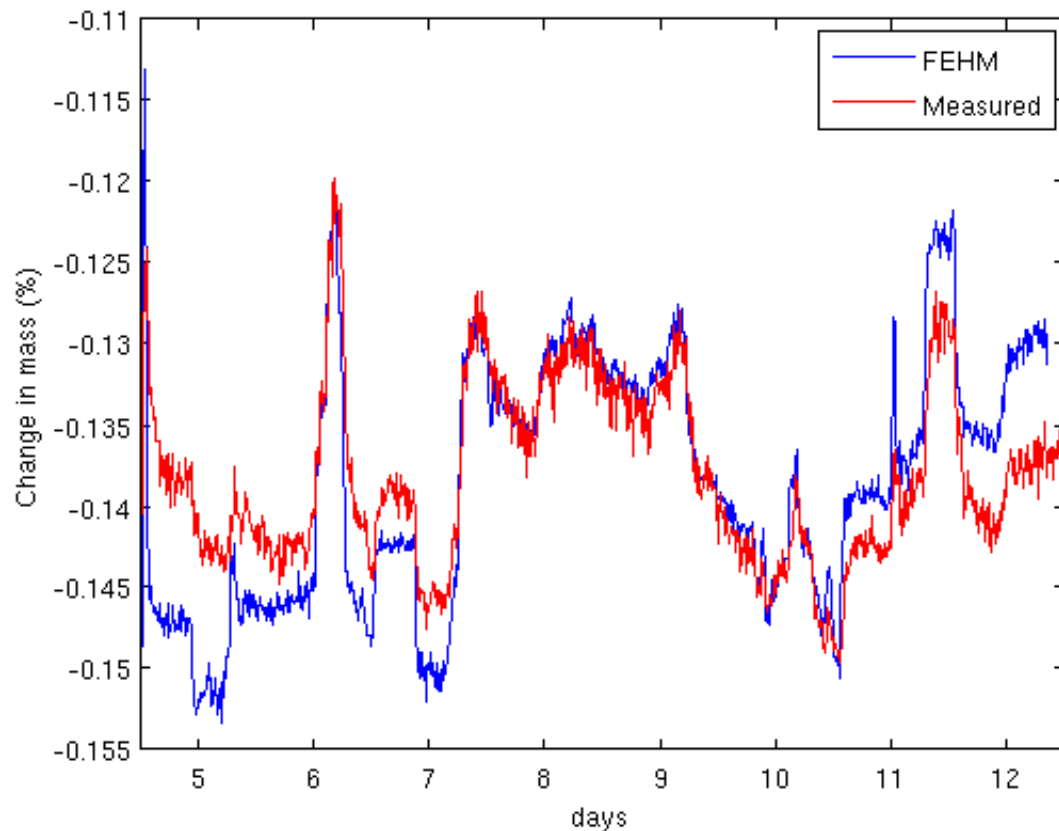
Figure 44: Mass change (%) of salt cone, showing comparison of FEHM model results (blue) to experimental measurements (red).

The results also indicate the vapor pressure lowering regime calculated for RoM salt in the FEHM simulations is appropriate at the WIPP site. Based on field observations, the dissolved WIPP salt and capillary pressure cause the pore water for RoM salt to require a relative humidity of about 25 % than that of pure water. The combination of P_{wv} lowering due to dissolved salt in pore water and with the additional retention resulting from capillary pressure in variably-saturated RoM salt, produces a reasonable match to the experimental data. The salt-dependent P_{wv}-lowering relationship was added to the salt module in FEHM, and tested in this validation study. The good fit between the measured and modeled data suggests the 25 % relative humidity estimate is appropriate for moving forward with more complicated modeling in the future.

CONCLUSIONS

Modeling the complicated and coupled THMC processes around placement of a heat-generating source in variably-saturated, crushed salt includes in many uncertainties. The validation of new FEHM capabilities for simulation of salt and relative humidity by comparison of model results with data from simple experiments, as discussed above, builds confidence in model accuracy. Rates of evaporation and

precipitation of water vapor from granular salt depend not only on the relative humidity of air in the subsurface, but also the lowering of the water-vapor pressure for pore water with dissolved salt and capillary retention. The experiment represented a dynamic system with simple constrained parameters which rendered a dataset with which to compare to modeled results. We see a general agreement between the modeled and experimental results, suggesting FEHM is will perform well for simulations including a higher degree of complexity. Thus the newly added salt module is a valuable tool for modeling future experiments and HGNW disposal in bedded salt.

ACKNOWLEDGEMENTS

REFERENCES

1. McMahon, K. 2012. Update of the Used-Fuel Disposition Campaign Implementation Plan, DOE Office of Nuclear Energy Report FCRD-UFD-2012-000334. Albuquerque, NM.

2. Hansen, F.D., and C.D. Leigh. 2012. Salt disposal of heat-generating nuclear waste. Sandia National Laboratories Report SAND2011-0161. Albuquerque, NM.

3. Kuhlman, K.L., and B. Malama. 2013. Brine Flow in Heated Geologic Salt. Sandia National Laboratories Report SAND2013-1944. Albuquerque, NM.

4. Caporuscio, F.A., H. Boukhalfa, M.C. Cheshire, A.B. Jordan, and M. Ding. 2013. Brine Migration Experimental Studies for Salt Repositories, FCRD Used Fuel Disposition Campaign Milestone FCRD-UFD-2013-000204. Los Alamos, NM.

5. Kelly, W.R. 1985. Brine migration in salt: Topical report. http://pbadupws.nrc.gov/docs/ML0404/ML040410467.pdf (accessed 10 July 2013).

6. Jordan, A.B., H. Boukhalfa, F.A. Caporuscio, B.A. Robinson, P.H. Stauffer. 2015. Hydrous Mineral Dehydration around Heat-Generating Nuclear Waste in Bedded Salt Formations, Environmental Science & Technology, accepted pending revisions.

7. Zyvoloski, G.A., B.A. Robinson, Z.V. Dash, and L.L. Trease. 1997. Summary of the models and methods for the FEHM application—A finite element mass-and heat-transfer code. Los Alamos National Laboratory Report LA-13307-MS, modified 1999. Los Alamos, NM.

8. Zyvoloski, G.A. 2007. FEHM: A control volume finite element code for simulating subsurface multi-phase multi-fluid heat and mass transfer. Los Alamos National Laboratory Report LA-UR-07-3359. Los Alamos, NM.

9. Kelkar, S., G. WoldeGabriel, and K. Rehfeldt. 2011. Hot Dry Rock Geothermal Energy Development at Los Alamos National Laboratory: 1970-1995, Final Report. Los Alamos National Laboratory Report LA-14433-HDR. Los Alamos, NM.

10. Bourret, S.M., P.J. Johnson, G.A. Zyvoloski, S.P. Chu, D.J. Weaver, S. Otto, H. Bouklhalfa, F.A. Caporuscio, A.B. Jordan, P.H. Stauffer. 2016. Experiments and Modeling in Support of Generic Salt Repository Science. Los Alamos National Laboratory Document, LA-UR-16-27329. Los Alamos, NM.

11. Jordan, A.B., H. Boukhalfa, F.A. Caporuscio, and P.H. Stauffer. 2015. Brine Transport Experiments in Run-of-Mine Salt. Los Alamos National Laboratory Report LA-UR-15-26804. Los Alamos, NM.

12. Jordan, A.B., G.A. Zyvoloski, D.J. Weaver, S. Otto, and P.H. Stauffer. 2015. Coupled Thermal-Hydrologic-Chemical Model for In-Drift Disposal Test. Los Alamos National Laboratory Report LA-UR-15-27442. Los Alamos, NM.

13. Jordan, A.B., P.H. Stauffer, D.T. Reed, H. Boukhalfa, F.A. Caporuscio, and B.A. Robinson. 2014. Draft Test Plan for Brine Migration Experimental Studies in Run-of-Mine Salt Backfill. Los Alamos National Laboratory Report LA-UR-14-27338. Los Alamos, NM.

14. Stauffer, P.H., D.R. Harp, A.B. Jordan, Z. Lu, S. Kelkar, Q. Kang, J. Ten Cate, H. Boukhalfa, Y. Labayed, P.W. Reimus, F.A. Caporuscio, T.A. Miller, and B.A. Robinson. 2013. Coupled model for heat and water transport in a high level waste repository in salt. Los Alamos National Laboratory Document, LA-UR-13-27584. Los Alamos, NM.

    http://www.energy.gov/sites/prod/files/2013/12/f5/CouplModelHeatWaterTransprtGenericHLW RepSalt_1.pdf.

15. Stauffer, P.H., D.R. Harp, and B.A. Robinson (2012). Model Development and Analysis of the Fate and Transport of Water in a Salt-Based Repository, Used Fuel Disposition Campaign Milestone M2FT-12LA08180112, LANL Report LA-UR-12-25050. Los Alamos, NM.

16. Eppelbaum, L.V., I. Kutasov, and A. Pilchin. 2014. Applied Geothermics. Springer Science and Business Media LLC, New York, NY.

Experiments and Modeling to Support Field Test Design

Appendix C: In drift design, emplacement, and model domain

Schematic drawings of the canister within a drift are shown in Figures 45 and 46. Images from the canister emplacement and covering follow (Figures 47 to 51). The full model domain used in simulations is shown in Figure 52.
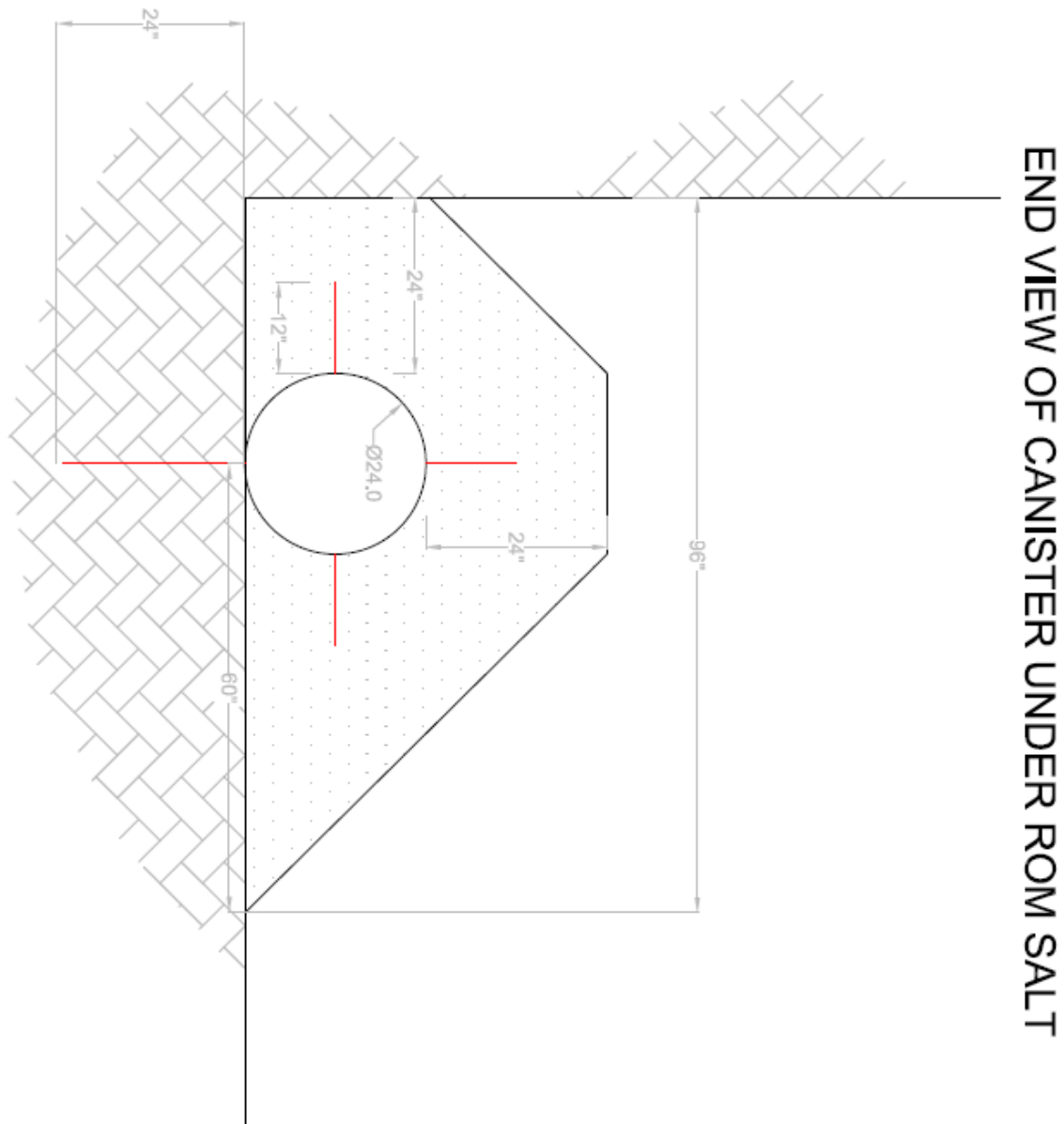

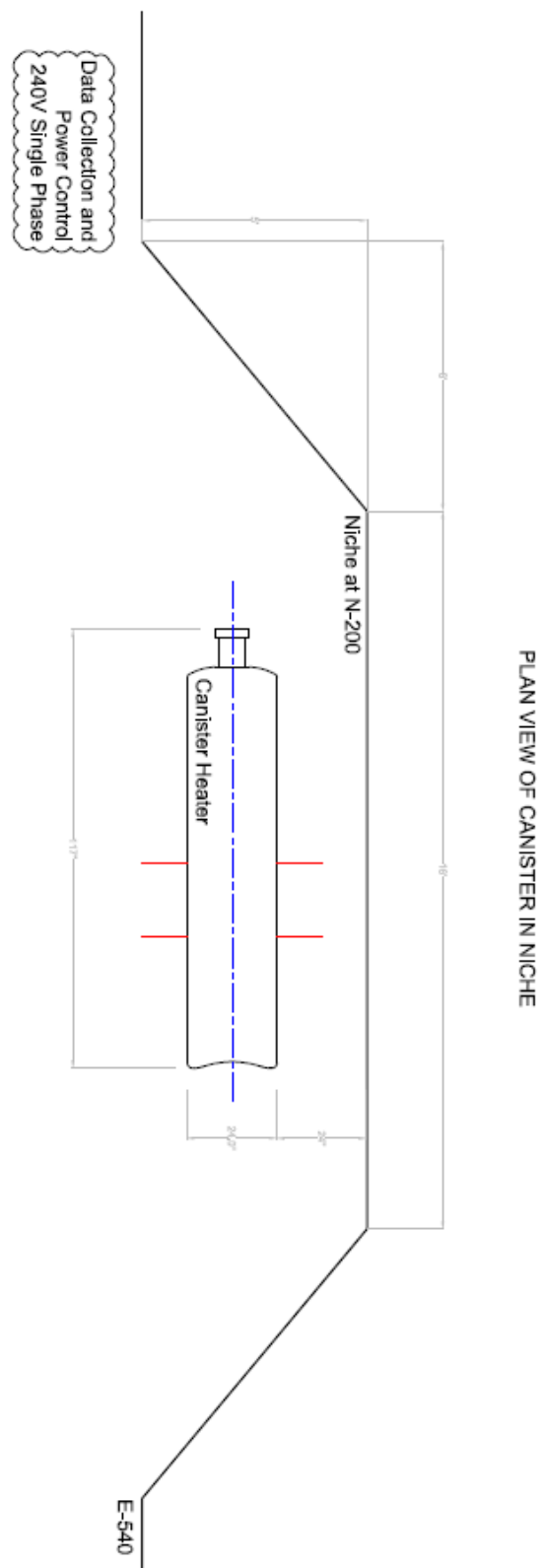*Figure 45: End view schematic of canister emplacement, showing dimensions of pile.*

Experiments and Modeling to Support Field Test Design

Figure 46: Side view schematic of canister emplaced in pile.

Experiments and Modeling to Support Field Test Design

The following set of images show the canister placed on the floor prior to being covered in salt, taken beginning on August 21, 2017. Completion of canister placement and burial is scheduled by August 30, 2017.

Figure 47: Oblique view of canister prior to application of salt cover. Blue coloring on floor indicates measurements for pile extent. Note carved wall and damage to wall rock in background behind canister.

Experiments and Modeling to Support Field Test Design

Figure 48: End view of canister. Salt pile will connect from canister to wall; pile-wall interface is an area of interest. Blue markings on floor indicate measurement lines for canister placement.
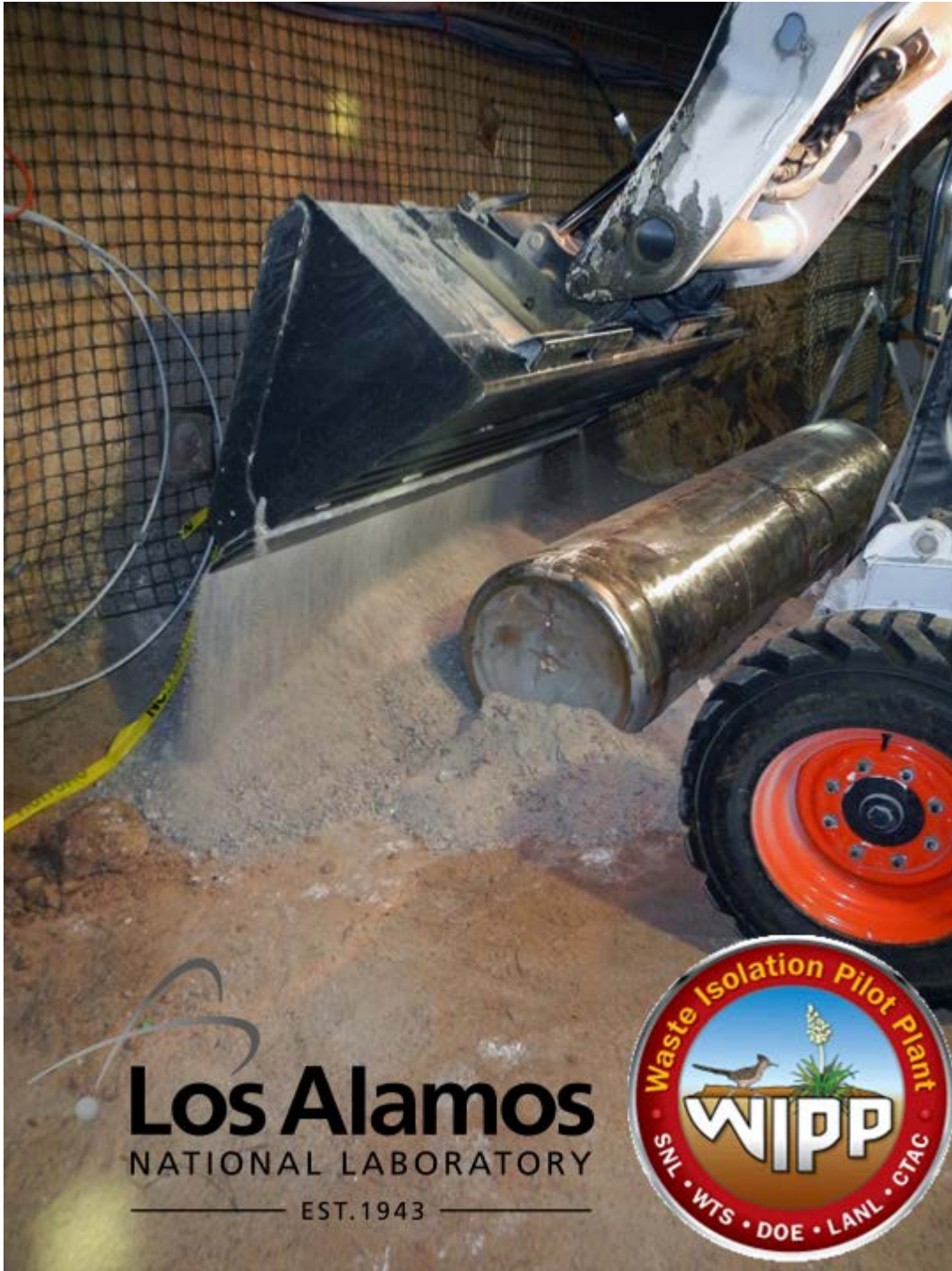
Figure 49: End-view of canister in early stages of salt cover.

Experiments and Modeling to Support Field Test Design

Figure 50: End view of intermediate stage of salt placement. For this experiment, cuttings from rockbolt holes (bright white salt) are applied to protect wiring and thermocouples (exposed wiring).

Experiments and Modeling to Support Field Test Design

Figure 51: Installation of vertical thermocouple arrays extending from top of can towards top of pile.

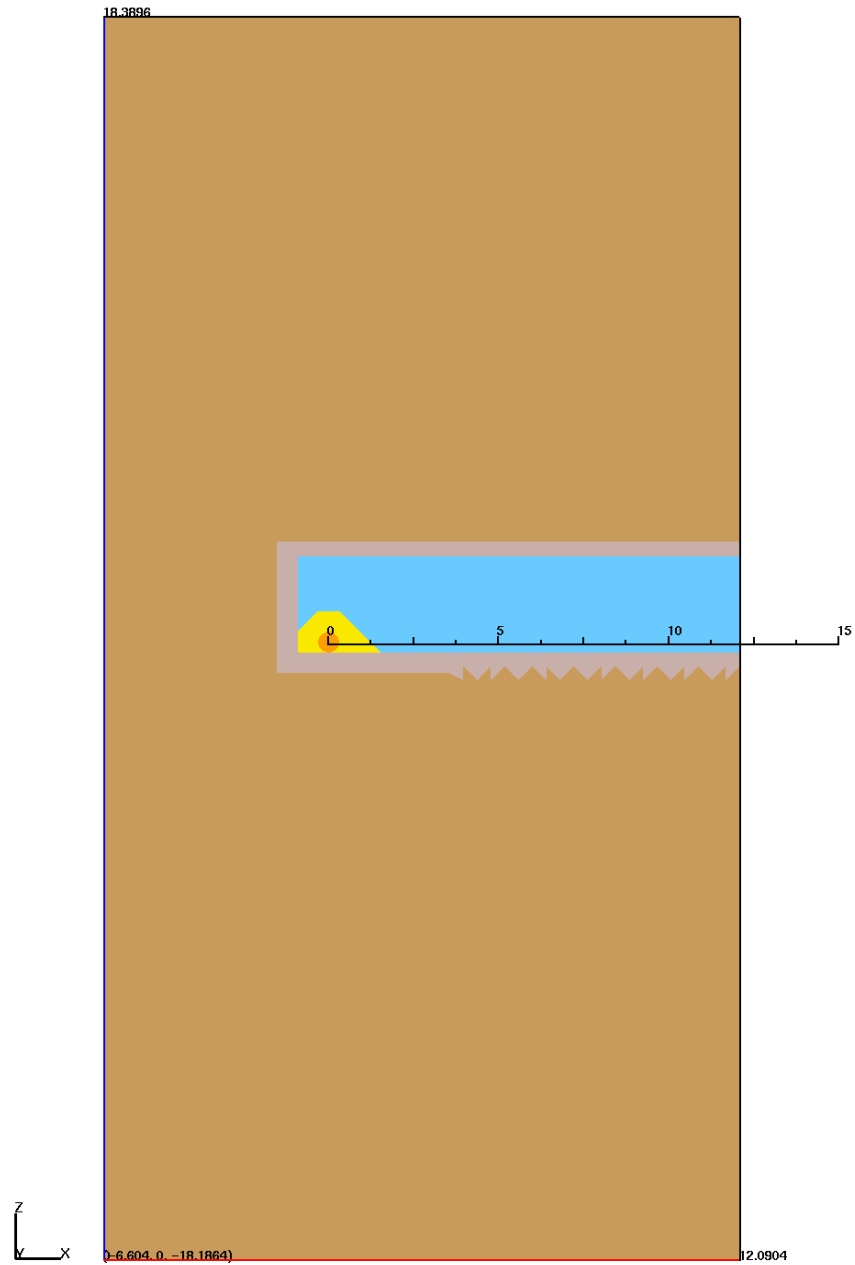Experiments and Modeling to Support Field Test Design

Figure 52: Complete mesh used for 2-D salt gallery modeling, with extensive region of intact rock salt beyond pile. Intact salt serves as a thermal sink.